DEVICE AND IMAGE ANALYSIS ADVANCEMENTS TOWARDS PHOTOACOUSTIC AND ULTRASOUND TOMOGRAPHY-GUIDED PROSTATE BIOPSY
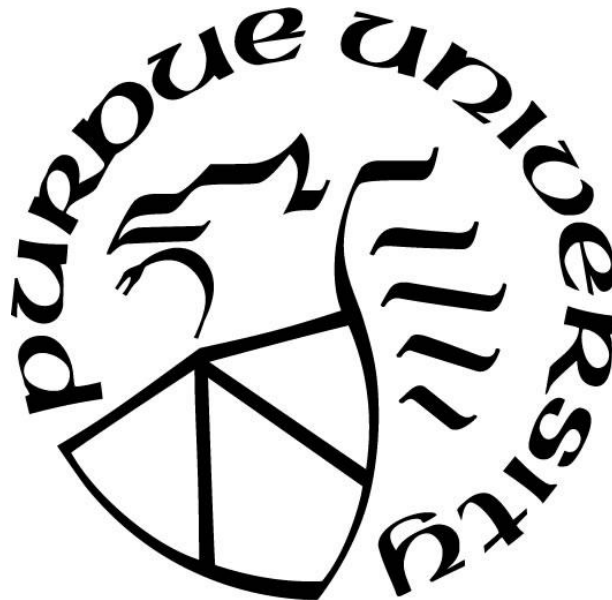
by

Brittani Lynn Bungart

A Dissertation

Submitted to the Faculty of Purdue University

In Partial Fulfillment of the Requirements for the degree of

Doctor of Philosophy

Weldon School of Biomedical Engineering

West Lafayette, Indiana

May 2019

THE PURDUE UNIVERSITY GRADUATE SCHOOL
STATEMENT OF COMMITTEE APPROVAL

Dr. Ji-Xin Cheng, Ph.D., Co-chair

> Weldon School of Biomedical Engineering, Purdue University, West Lafayette, Indiana, USA; Moustakas Chair Professor in Photonics and Optoelectronics, Department of Electrical and Computer Engineering, Department of Biomedical Engineering, Boston University, Boston, Massachusetts, USA

Dr. Young Kim, Ph.D., Co-chair

> Weldon School of Biomedical Engineering, Purdue University, West Lafayette, Indiana, USA

Dr. Craig Goergen, Ph.D.

> Weldon School of Biomedical Engineering, Purdue University, West Lafayette, Indiana, USA

Dr. Timothy Masterson, M.D.

> Department of Urology, Indiana University School of Medicine, Indianapolis, Indiana, USA

Approved by:

> Dr. George R. Wodicka
>
> Head of the Graduate Program

To my father and brother.

ACKNOWLEDGMENTS

The contents of this dissertation were made possible by contributions from many people. I am grateful for the support of these people and the opportunity to learn from them. First, I would like to thank Dr. Ji-Xin Cheng and Dr. Young Kim for co-mentoring me during my graduate studies. I especially appreciate Dr. Ji-Xin Cheng for his research support and guidance. The lessons learned while working in his lab were paramount to the work in this dissertation. I would also like to thank the rest of my committee members: Dr. Craig Goergen and Dr. Timothy Masterson. Dr. Craig Goergen provided his important ultrasound expertise to my committee along with technical knowledge of photoacoustic tomography.

For the clinical components of this dissertation, Dr. Timothy Masterson, Dr. Michael Koch and Dr. Liang Cheng provided their exceptional expertise and resources to make this work possible. I am very grateful Dr. Masterson for allowing me to observe many clinical procedures. Dr. Liang Cheng also provided significant clinical guidance for the histopathology background and provided much time for annotating the tissue slides for a ground truth reference. I am appreciative of Dr. Timothy Masterson and Dr. Michael Koch for allowing the recruitment of the prostate specimens for the imaging studies. Thank you to the patients who consented for participation in the imaging studies, and the nursing staff who helped coordinate the patient consent.

Other research collaborators were pivotal to this dissertation, such as the other members of the Ji-Xin Cheng lab. I especially want to thank Pu Wang, Rui Li, Lu Lan, Yingchun Cao, Jie Hui, Jiayingzi Wu, Delong Zhang, Hyeon Jeong Lee, Yi Zhang, Jason Liao, and Tiffany Yang-Tran. I appreciate the contributions of students from other labs including Sean Gorsky and Emil Atz. A special thank you should also be given to Dr. Timothy Ratliff for his collaboration on this work.

Acknowledgement is necessary to all the support provided by the Weldon School of Biomedical Engineering, the Indiana University School of Medicine's Medical Scientist Training Program, and Boston University's Electrical and Computer Engineering Department. I am beyond grateful for the resources and support that were given to me. Those at the Weldon School of Biomedical Engineering, such as Sandra May, Andrew Brightman, Linda Doyle, Kathryn Cooper, Susan Hardy, Bill Schoenlein and others, were always willing to answer questions and

TABLE OF CONTENTS

LIST OF TABLES

LIST OF FIGURES

LIST OF ABBREVIATIONS

18F-ACBC, 1-amino-3-fluorine-18-fluorocyclobutane-1-carboxylic acid

18F-FC, 18F-fluorocholine

18F-FDG, 18F-fluorodeoxyglucose

BPH, bengin prostatic hyperplasia

mpMRI, **multiparametric** magnetic resonance imaging

MRI, magnetic resonance imaging

MMF, multimode fiber

pSNR, peak signal-to-noise ratio

PA, photoacoustic

PAT, photoacoustic tomography

PCa, prostate cancer

PSA, prostate-specific antigen

PSMA, prostate-specific membrane antigen

ROI, region of interest

TRUS, transrectal ultrasound

US, ultrasound

ABSTRACT

Author: Bungart, Brittani, L. PhD
Institution: Purdue University
Degree Received: May 2019
Title: Device and Analysis Advancements Towards Photoacoustic Tomography-guided Prostate
  Biopsy
Committee Chairs: Dr. Ji-Xin Cheng, Ph.D., Dr. Young Kim, Ph.D.

To confirm the presence of prostate cancer which is the most incident visceral cancer in men, prostate biopsies are acquired using the magnetic resonance imaging fusion-guided prostate biopsy protocol. For this approach annotated magnetic resonance imaging is overlaid onto real-time ultrasound imaging to guide sampling of suspicious regions marked by uroradiologists. Additional biopsy samples are acquired via the previous clinical gold standard, i.e. the templated 12-core transrectal ultrasound-guided prostate biopsy protocol. While this approach improves the sensitivity of the prostate biopsy, a real-time, multiparametric imaging method of identifying biopsy targets could help overcome some of the inherent pitfalls of the magnetic resonance imaging fusion-guided prostate biopsy. Since ultrasound is used during the prostate biopsy, photoacoustic tomography, e.g. a hybrid imaging modality in which clinical ultrasound probes can be used to detect centimeters deep chemical alterations, has the potential to provide real-time targeting during biopsy. The translation of photoacoustic tomography to the clinic for prostate biopsy has been prevented by engineering challenges, which include identification of a biomarker for detecting suspicious regions of tissue and light delivery to the prostate for photoacoustic signal generation. Here, we present a vascular texture analysis method that identified 100% of primary and 67% of secondary tumors in the testing data set of *ex vivo* human prostate specimens. This method can be applied to future *in vivo* photoacoustic and ultrasound tomography of human prostates after further optimization of light delivery for photoacoustic tomography. To progress towards achieving this aim, we developed a transurethral light delivery device with angular light coupling method. By controlling the launch angle of the light into the fiber, the conversion of forward to side propagating energy can be improved from 27% to 98%, and the longitudinal emission profile can be controlled in order to illuminate the whole prostate simultaneously.

1. INTRODUCTION

1.1 Significance and Epidemiology: PCa

PCa is the most incident visceral cancer in men in the USA with an estimated 164,690 cases diagnosed in 2018, which is approximately 9.5% of all 2018 new cancer occurrences. The median age at PCa diagnosis is 66 years old compared to 80 years old as the median age of PCa-caused mortality. The current overall 5-year survival rate is 98.2% since 90% of PCa is discovered at a local or regional stage, but the 5-year survival rate drops to 30% if the PCa has metastasized prior to diagnosis [6]. Therefore, identifying PCa at a local or regional stage is paramount for long-term patient survival.

1.2 Current Diagnostic Paradigm for PCa

Based on the American Urological Association guidelines, serum PSA with or without digital rectal exam is recommended as a screening tool for PCa depending on risk factors such as age and the man's preference [7]. PSA is produced exclusively by prostate epithelial cells [8] and can be influenced by benign conditions such as bacterial prostatitis [9,10], ejaculation [11], and BPH [12]. Thus, false positive rates from serum PSA measurement can range from 12% to 76% based on frequency of use and PSA level cutoffs [13,14]. Since serum PSA measurement is a screening tool, it does not confirm a diagnosis of PCa, especially since the specificity of the test is low.

To confirm the presence of PCa, histopathology must currently be performed on samples acquired from the prostate tumor. Within the last year, the clinical standard for acquiring these samples during initial prostate biopsy has changed from a templated approach with TRUS guidance, which entails systematically acquiring 12 random cores of the prostate bilaterally [4,15], to using the MRI fusion-guided biopsy [1–3] if insurance covers the procedure. Otherwise, patients undergo the templated TRUS-guided prostate biopsy for the initial biopsy, and if concern of a false negative result exists after negative results, the MRI fusion-guided biopsy will be performed during the follow up biopsy procedure [16,17].

The change in the initial prostate biopsy procedure is due to the poor sensitivity of the templated TRUS-guided prostate biopsy, which is performed transrectally using an US probe to

locate anatomical landmarks to ensure uniform sampling with no tumor specifically targeted during the procedure. Even with optimization of the templated TRUS-guided prostate biopsy, the need for repeating a biopsy following negative results is approximately 12% within 1 year and 38% within 5 years [18]. This can be attributed to the limited sampling of the prostate as a whole. The average core is a cylinder with an approximate diameter of 0.1 cm and length of 1.0 to 1.5 cm [19]. For 12 cores the volume is 0.56 cm^3 at best if acceptable cores are acquired. The normal prostate size is approximately 45 cc [19]. Therefore based on prostate size, 1% to 2% is sampled during prostate biopsy using the recommended method.

The MRI fusion-guided biopsy's improved detection rate of clinically significant PCa compared to the templated TRUS-guided prostate biopsy [1,20–22] is due to the procedure having regions of concern based on a urogenital radiologist's assessment of a mpMRI of the prostate [23]. If a suspicious region is located on the mpMRI, the patient will come back to the clinic for the MRI fusion-guided biopsy. During this procedure the patient will lay still in the left lateral decubitus position. To fuse the previously acquired mpMRI with the real time US imaging, a calibration will be performed to align the images. Then, the regions of concern will be biopsied at least two times and 12 cores would be acquired by the templated TRUS-guided prostate biopsy procedure [1,24].

While the MRI fusion-guided biopsy provides improvement over the previous standard of care [1,25,26] and integrates well into the clinical workflow [27], some disadvantages exist. Careful calibration is needed to fuse the mpMRI with the real-time US imaging during the prostate biopsy procedure. If the movement occurs during the procedure, the fusion will have to be re-calibrated. Additionally since the mpMRI is a static image, the tissue may become distorted by the US probe, which may affect the imaging overlay [28]. The mpMRI is also a costly procedure [29] that utilizes contrast agents, which may be contraindicated in some patients [30].

For both the templated TRUS-guided and MRI fusion prostate biopsy, pitfalls related to the invasiveness of the procedure exist. Significant complications can occur following the procedure with an overall rate of complications at 2% and infection being the major complication [31]. The risk of experiencing a complication is affected by the number of core biopsies; increased core biopsy number is associated with an increased risk of experiencing a complication [32]. MRI fusion-guided biopsy has been shown to need less biopsy cores for the

same PCa detection rate [26]. For men who require repeat biopsies, additional risk of complications are unnecessarily added if the biopsy was successful initially.

1.3   Clinical Need Overview

In summary, the current paradigm of PCa diagnosis has improved in recent years, but still has many negative attributes considering the incidence of PCa and the chronic nature of the disease. The screening tool used for PCa, i.e. serum PSA measurement, is imperfect in its specificity, while those continuing through the necessary process of diagnosis can experience an additional appointment for the mpMRI before the biopsy procedure. Additional improvements may still be made on the prostate biopsy workflow. In the remaining chapter, current advances in prostate biopsy acquisition and other pertinent information is reviewed in order to propose a method for real-time targeting of the prostate biopsy.

1.4   PCa and Its Anatomical Position

1.4.1   Classification of PCa

PCa can be classified into various subtypes. Overall, non-variant adenocarcinoma is the most common form of PCa with 99.6% of cases falling under this category [33]. To determine the presence and type of PCa, the prostate biopsy is assessed by a pathologist with traditional haemotoxylin and eosin staining. PCa is assessed based on morphology of the prostatic glands. For adenocarcinoma, decreasing gland size and loss of the glands' lumen equates to increasing Gleason grade ranging from 3-5 in current use. The pathologist will ultimately give a percentage of PCa involvement of the biopsied cores along with a final Gleason score, which is determined by summing the two most prevalent Gleason grades [34,35]. The Gleason score can be categorized into groups to aid in predicting treatment outcomes. This Gleason score, its grade group [35,36], and the stage [37] of the PCa is used as a prognostic indicator for the patient to help with therapeutic decision-making.

1.4.2   Anatomy Relating to PCa

Understanding the anatomy is pivotal for acquiring a biopsy specimen and for reading images for targeting the acquisition of the biopsy. Approaches to accessing the prostate are

shown in **Figure 1.1**, which includes transrectal, transperineal, and transurethral**.** Other external methods exist to image the prostate and would visualize all the anatomy shown in **Figure 1.1**. In order to choose the best approach to decreasing the need to have a repeat biopsy, the appropriate anatomy will be discussed.

1.4.3   Prostate Anatomy

The prostate sits just below the bladder as depicted in **Figure 1.1** with the prostatic urethra running through the prostate in a nearly vertical manner with a 35° bend at the vermontanum. The prostate is sectioned into regions as first described by McNeal [38]. As shown in **Figure 1.2**, the glandular prostate is subdivided into three zones: the peripheral zone, central zone, and transition zone. The respective percent volumes for these glandular areas is 70%, 25% and 5%. The anterior one-third of the prostate is comprised of fibromuscular stroma, which has very few glands [38,39].

The prostate size on average increases with age as approximately 90% of men develop BPH, which affects the transition zone, by 80 years old [40]. The average age of PCa diagnosis is 66 years old [37], and at this age, the average prostate size is approximately 45 cm^3 [19]. The normal prostate dimensions are 4.0 cm x 2.5 cm x 3.2 cm (lateral x anterior-posterior x height) [41] while in a small study of 41 patients with the average age of 70 years old, the dimensions were 5.3 cm x 4.9 cm x 3.5 cm [42]. As PCa is usually an adenocarcinoma and thus arises from epithelial cells [33], the frequency of PCa tumors is not uniform throughout the prostate. About 75 – 80% of PCa arises in the peripheral zone while the rest arise from the central zone and transitional zone [43]. The frequency of PCa tumor foci can be appreciated in **Figure 1.3**. While considering PCa imaging modalities, it is imperative to consider the ability for the modality to visualize the portion of the prostate that gives rise to PCa.

1.5   Distinguishing PCa from Benign Tissue

For imaging purposes to sample the prostate, a detectable difference needs to be present to distinguish benign from malignant tissue. From a pathological standpoint, nonmalignant tissue can be classified into unremarkable, BPH, inflammatory and inflammatory-like lesions, adenocarcinoma-mimicking lesions, non-prostatic tissue present in the prostate, and benign stromal lesions [39]. BPH is the most prevalent pathology of the prostate with approximately

70% of men between 61-70 years old exhibiting clinical BPH [40]. Similar to PCa [37], the likelihood of having BPH increases with increasing age as few men younger than 50 years old have clinical BPH [37,40]. This is especially important to consider as BPH causes enlargement of the prostate with the average prostate volume increasing by 50% from age 50 to 70 years old [44,45].

As already mentioned in the previous subsection, PCa is differentiated ultimately from other conditions via histopathology, and the structural differences in gland size and formation are used for the Gleason score and grouping for therapeutic decision-making [34,35]. As this is a microscopic assessment performed by a well-trained pathologist on tissue, we need to ensure that the samples acquired are representative of the disease. To achieve this many techniques have been explored including US, MRI, positron emission tomography, and optical-based methods. These methods will be discussed further including the science behind how each modality specifically identifies PCa.

1.6   Assessment of Current Techniques for PCa Image-Guided Biopsy Acquisition

1.6.1   US-based Imaging Modalities for Targeting Prostate Biopsy

The most commonly used imaging technique for guiding prostate biopsy is B-mode US, which was introduced in 1989. With this imaging modality, the peripheral zone can be clearly distinguished from the central and transition zone by echogenicity [46]. Due to this ability, US is currently used to observe the anatomy of the prostate and the surrounding tissue to acquire 12 core biopsies in a systematic manner bilaterally. With the transrectal access to the prostate, the entire anterior-posterior axis can be observed [4,15]. This approach to obtaining prostate core biopsies is known to have low sensitivity though, as the need to have a repeat prostate biopsy following negative histopathological results is approximately 12% within 1 year and 38% within 5 years [18]. Upon repeat biopsy, approximately 20% will have cores positive for PCa [47]. A major consideration is that this approach significantly under samples the prostate. Based on computational analysis, locations in the peripheral zone and anterior transition zone are likely to be under sampled considering the frequency of tumor foci [48,49]. Therefore, a method to direct the core acquisition is needed.

1.6.1.1   US Techniques Using Tissue Defects as Contrast

As there are differences in echogenicity that delineates the zonal anatomy, alterations in echogenicity [46] have been shown to represent PCa, especially hypoechogenicity, since the US signal's backscatter is altered. The contrast is thought to represent cellular and tissue alterations compared to normal glandular prostatic tissue [15]. Thus, echogenicity changes have been studied for its clinical utility in guiding the biopsy and shown to nearly double the efficiency of sampling a clinically significant PCa tumor [50]. Unfortunately like the PSA test, the use of echogenicity alone as a PCa marker is not specific to PCa, and BPH, inflammation, and infarction can similarly appear hypoechoic compared to normal surrounding tissue [51]. When using echogenicity as a biomarker for targeting the core biopsy, up to 60% of the hypoechoic lesions can be benign [52]. Therefore, the approach of random and echogenicity-targeted US cannot delineate between benign and malignant prostate tissue.

The approach to targeting based on echogenicity alterations within prostate zones is user-biased. To minimize the user-specific inconsistencies of US imaging, computer-based, real-time analysis of the US images has been applied. One commercially available tool is prostate Histoscanning^{TM} which was originally proposed as a "triage test…to avoid prostate biopsy" [53], but has since been studied to target biopsy and aid in reducing the number of biopsy cores [54]. Once the perimeter of the prostate is selected after scanning the prostate with US, sub-volumes are analyzed to determine PCa tumor location and size [55]. Individual signal volumes can have set cutoffs for inclusions of cancer or not cancer [54]. The specific algorithms of determining cancerous sub-volumes are not specified within literature, but the analysis is performed on radiofrequency information of the backscattered sound [56].

The results of using prostate Histoscanning^{TM} for identifying tumor volume, location, and extraprostatic extension of the PCa are conflicting [53,56–58]. prostate Histoscanning^{TM} for targeting the core biopsy has been shown to have sensitivity between 40 - 100% depending on the signal cutoff volume. While the sensitivity improves with decreasing signal cutoff volume, the specificity worsens as it can range from 28 – 73% [54]. Lastly, prostate Histoscanning^{TM} is a poor tool for use in the anterior prostate [56], which is a problem area for under sampling with the templated TRUS-guided prostate biopsy [48,49].

All of these previously discussed B-mode US approaches use a similar frequency US transducer that functions in the lower MHz range (5 – 9 MHz) [50,57,59]. If you consider the

speed of sound in human soft tissue to be 1540 m/s [60], then the axial resolution of these lower frequency US transducers is $170 - 300$ µm. If a higher frequency US transducer was utilized, the resolution could be improved. This approach has been recently explored using high frequency TRUS probes that have a 21 MHz center frequency with a maximum of 29 MHz [61,62]. With the higher frequency probe, an axial resolution of approximately 70 µm has been achieved, which is comparable to MRI resolution. Unfortunately to achieve this resolution, imaging depth has to be sacrificed. The maximum anterior-to-posterior imaging depth is 5 cm with this new frequency range [62], which should be sufficient for imaging the depth of the prostate [19,41].

In a preliminary study with 25 patients, the sensitivity of high versus low frequency US was 65% and 38% [61]. The low frequency US data matched well with the sensitivity of hypoechoic lesions as a targeting tool for biopsy [52]. A current multicenter trial is being performed to validate the use of high frequency US, and a scoring system has been published that correlates to likelihood of detection cancer in a core sample [62], which is similar to approaches with mpMRI [5].

1.6.1.2 US Techniques Using Tissue Mechanical Properties as Contrast

Another US technique that capitalizes upon changes in PCa compared to normal tissue is real-time elastography US in which the increased stiffness is utilized as a contrast [63,64]. This stiffness, which is also the basis for the digital rectal exam, is due to the increased cell density, decreased gland size, and increased collagen content in the surrounding stroma [65,66]. There are three subtypes of real-time elastography: strain elastography, acoustic radiation force impulse, and shear wave elastography.

Strain elastography is performed by the user compressing and decompressing the prostate with an US probe. A pseudo-colored map is overlaid with the B-mode US imaging to show the deformation within the prostate. A recent meta-analysis of strain elastography performance directly before radical prostatecomy revealed that the specificity and sensitivity for strain elastography are 76% and 72% respectively [67]. One issue with this approach is the bias due to the patients enrolled in the study had known significant disease that warranted curative therapy by removing the prostate. In a study with 171 patients, strain elastography was shown to have similar performance [68]. A pitfall of strain elastography is that the compression cycles are manually performed, and thus the results are operator-dependent.

Acoustic radiation force impulse is a similar technique to strain elastography except the operator-dependency is not a factor as the displacing forces are created by the US probe itself by using focused, high intensity US. While acoustic radiation force impulse could initially image prostate anatomy and cancer lesions, it was unable to image the full depth of the prostate as the compression force attenuated [69]. This complication was still observed when imaging *in vivo* [70,71]. In a sample size of 29 patients with biopsy-confirmed PCa, acoustic radiation force impulse detected 79.3% of posterior tumors and 33% of anterior lesions [71]. This method is still yet to be tested in a population of patients who are not biopsy-proven to have PCa. One advantage of acoustic radiation force impulse is that the imaging is real-time and co-localized with B-mode US imaging. This is beneficial for biopsy as the clinician may apply pressure during the biopsy which could deform the prostate.

Shear wave elastography similarly does not utilize manual compression cycles as shear waves are generated from acoustic radiation forces of the US transducer. The velocity of the shear wave is measured and provides a quantitative image of stiffness since the shear wave velocity is proportional to Young's modulus. Initial studies have delivered encouraging results of sensitivity and specificity of 96% with a cutoff of 37 kPa [72] and 96% and 85% with 35 kPa cutoff [73]. Alternatively, other results of sensitivity and specificity of 81% and 69% have not been as promising when a 50 kPa cutoff was used [74]. Shear wave elastography has not been shown to improve the detection rate of PCa per core sample, but increased risk for the presence of PCa was found for individuals with concerning lesions in shear wave elastography imaging [75]. As for shear wave elastography currently, the kPa cutoff for PCa is not standardized, which can explain the variation in results.

1.6.1.3 US Techniques Using Angiogenesis as Contrast

Another change observed in PCa tissue is an increase in vasculature density, especially due to neo-microvessels which are characterized as having diameters of $10 - 50$ µm [76,77]. Compared to benign adjacent tissue, PCa tissue on average has twice the vasculature per field of view, but variability of the relative vasculature amount within the tumor and from person-to-person exists [77]. This increase in vasculature has been the foundation for Doppler US in which the flowing red blood cells cause a frequency shift in the acoustic wave proportional to the velocity. Color Doppler US is the pseudo-colored, live view of this frequency shift, which

depicts positive and negative velocity, overlaid on the grayscale B-mode US to show areas of increased vasculature. Another way to display color Doppler US is with the absolute value of the frequency shift, which is called power Doppler US [78–80].

The performance of color and power Doppler US have been variable at detecting PCa. Power Doppler US is more sensitive to perfusion compared to color Doppler US, but the tradeoff is the loss of information on the vasculature flow direction. While some studies have shown that power Doppler US is a promising improvement to aid in guiding [79] and preventing unnecessary prostate biopsy [81], other studies have shown that power and color Doppler US underperformed compared to the templated 12 core TRUS-guided prostate biopsy [78,80]. These results could be partially explained by the diameter of the microvessels, which are approximately $10 - 50\,\mu$m diameter [76,77]. The resolution of color and power Doppler US are not robust enough to achieve imaging of these vessels as lower frequency US transducers are used. The only benefit of power Doppler US has been observed in patients with higher PSA levels [80]. This improvement could be due to larger vessels present in the detected PCa tumors in patients with high serum PSA levels.

To overcome the limitation on vessel size, the method contrast-enhanced US was developed, in which an exogenous contrast agent has been utilized to improve the backscattering of US in the sub-resolution vasculature. The contrast agent used are gas-filled microbubbles, similar in size to red blood cells [82], which are injected intravenously during the biopsy to aid in visualizing the increased neo-vascularization within the tumor [83]. Contrast-enhanced US while using power Doppler US, i.e. contrast-enhance power Doppler US, was initially used to detect PCa prior to radical prostatectomy with approximately 86% of PCa tumors detected compared to histopathology. Unfortunately, contrast-enhanced power Doppler US could not differentiate PCa stages, especially extraprostatic extension. The translational value of this work is not as easily garnered since no direct comparison with systematic biopsy was performed [84].

When compared to systematic biopsy in 1,776 patients, contrast-enhanced color Doppler US doubled the positive biopsy rate to 12%, but the total core number was about half of the control group. While an improved detection rate of 12% was present with contrast-enhanced color Doppler US, 1.5% of the positive cases were detected only by templated TRUS-guided prostate biopsy [85]. More recent work has shown conflicting results in PCa detection between color Doppler US with and without contrast enhancement versus the templated TRUS-guided

prostate biopsy [86,87]. The conflicting results could be due to stability of the microbubbles when detected by US. If the mechanical force is too high, the microbubbles may be destroyed [88] and thus lower the signal intensity. Utilizing a lower US mechanical force has improved the imaging results for contrast-enhanced color Doppler US [89]. Other important pitfalls exist for using contrast-enhanced US for identification of biopsy targets. For instance benign lesions, such as prostatitis and BPH [90,91], can give a false positive biopsy targets even when accounting for prostate zones that are less likely to have BPH present [91]. Also, these contrast-enhanced changes in Doppler US images occur within seconds and are difficult to capture in the whole prostate as current probes are two dimensional. Therefore, multiple boluses of contrast agent are needed to capture multiple imaging slices [90].

In addition to the increased signal, the PCa tumor has altered kinetics of early signal enhancement and rapid washout of the microbubbles compared to benign prostate tissue which is the marker used for dynamic contrast-enhanced US imaging. Out of the parameters of arrival time, time to peak, and peak intensity, time to peak has been shown to correlate best with PCa Gleason grade [92,93]. This approach to biopsy targeting has similar negative attributes as discussed for intensity contrast-enhanced US, including false positives in transition zone due to BPH [93] and capturing sufficient imaging during the bolus of contrast agent.

Overall, US-based modalities have been well explored clinically for guiding prostate biopsy, and is currently utilized for finding anatomical landmarks during the procedure. Also, US imaging is a clinical tool that can be utilized in the exam room directly by the urologist in real-time. Many of the techniques mentioned do have a learning curve to achieving the best results and require additional intravenous injection of transient exogenous contrast agents to overcome the limited resolution of US compared to the biomarker.

1.6.2   MRI-based Imaging Modalities for Targeting Prostate Biopsy

In contrast to US, MRI has been largely applied in a multiparametric approach for targeting prostate biopsy. Currently if insurance covers the procedure, mpMRI is used to guide targeted biopsies via fusion with US for patients during initial prostate biopsy [1–3]. Otherwise, patients receive the MRI fusion-guided biopsy on repeat prostate biopsy [94]. The parameters considered for locating suspicious regions in mpMRI are: anatomical reference acquired by T2-weighted imaging and functional sequences diffusion-weighted imaging and dynamic contrast-

enhanced imaging to visualize different tumor characteristics. Another less common functional sequence is magnetic resonance spectroscopic imaging that may be included [24,95].

1.6.2.1 MRI Sequences Using Tissue Defects as Contrast

The mpMRI sequences that utilize alterations in tissue structure are T2-weighted imaging and diffusion-weighted imaging. T2-weighted imaging is the anatomical reference for the prostate zones, similar to greyscale US imaging. Differentiation of the zones is feasible due to different water and stromal tissue content. Thus, peripheral zone appears more intense and homogenous compared to transition and central zone [95].

The utility of T2-weighted imaging beyond anatomical reference is locating alterations in the intensity, especially in the transition zone where the majority of PCa arises. Also, T2-weighted imaging may be used to identify extraprostatic extension and invasion of the seminal vesicles, which indicate a more aggressive disease [95,96]. Unfortunately, T2-weighted imaging is not specific for PCa and other conditions can mimic PCa such as BPH, prostatitis, atrophy [95], and hemorrhage including from prior biopsy [95,97]. Therefore, additional MRI sequences and PCa characteristics must be included for the identification of suspicious regions for prostate biopsy targeting.

A robust MRI sequence is diffusion-weighted imaging in which cellular density, which is increased in PCa, is probed via the surrogate of Brownian water motion. As gland size decreases and becomes more packed with increasing Gleason grade, the intracellular to extracellular volume ratio increases. In doing so the water molecules become more restricted in their random movement in the extracellular compartment when varying magnetic fields are applied. Apparent diffusion coefficient is the quantification of this molecular motion and appears decreased in PCa tissue [98–101]. Diffusion-weighted imaging is thus not only beneficial in localizing PCa, but it also has been shown to correlate with PCa aggressiveness [99,100]. To ensure a high specificity for PCa with diffusion-weighted imaging, a higher cutoff needs to be used [102]. One of the positive attributes to diffusion-weighted imaging is that user bias is minimized due to the quantification and cutoffs for identifying suspicious regions [103]. Unfortunately, not all PCa can be located with diffusion-weighted imaging alone and is similarly affected by prior hemorrhaging [102].

1.6.2.2   MRI Sequence Using Angiogenesis as Contrast

Dynamic contrast-enhanced imaging is the functional sequence utilized in mpMRI to identify regions of increased neovasculature and their higher permeability [104,105], which is highly correlated to Gleason score [106]. To observe the dynamics of the prostate's blood flow, an MRI contrast agent, typically a gadolinium chelate, is injected to identify regions of early enhancement and fast washout, which is most characteristic of PCa. Similar to contrast-enhanced US, the bolus of contrast agent must be rapidly injected and a fast series of images acquired to properly observe the dynamics. The temporal resolution of dynamic contrast-enhanced imaging is approximately 3-5 seconds, but an entire view of the prostate can be captured compared to contrast-enhanced US [107,108]. Just like contrast-enhanced US, dynamic contrast-enhanced imaging also suffers lack of specificity for only PCa as angiogenesis can be observed in prostatitis and BPH and prior biopsy can cause false negative and positive results [108]. Another inherent problem with dynamic contrast-enhanced imaging is that an acquisition time of 5 minutes or longer is necessary to obtain enough temporal data for analysis of the contrast perfusion and diffusion dynamics [107,108]. As a coregistration of the pixels is needed to assess the changes over time, any motion, particularly rectal peristalsis, bladder filling and patient movement, can interfere with the imaging [108].

1.6.2.3   MRI Sequence Using Metabolic Alterations as Contrast

Magnetic resonance spectroscopic imaging is the functional sequence that can deliver a metabolic ratio map of the entire prostate. The critical metabolites imaged are citrate, choline, polyamines, and creatinine [109,110]. The ratio of choline, polyamines, and creatine to citrate is then used to locate suspicious regions that could be PCa. While normal peripheral zone has high levels of citrate and low choline, PCa has altered metabolism of citrate which lowers the concentration and an increase in choline-containing molecules is observed. Polyamines and creatine is also imaged as they cannot be distinguished from choline [111,112].

While magnetic resonance spectroscopic imaging provides a unique functional approach to identify PCa in mpMRI, the resolution is quite poor and requires considerable technical expertise to ensure acquisition of a quality sequence. Magnetic resonance spectroscopic imaging also has to be overlapped with the anatomical reference T2-weighted imaging due to the poor resolution [110]. For the localization of PCa, magnetic resonance spectroscopic imaging was

shown to provide added benefit compared to T2-weighted imaging alone [113]. Currently, the American College of Radiology and European Society of Uroradiology do not recommend the utilization of magnetic resonance spectroscopic imaging in standardized mpMRI for the MRI fusion-guided biopsy [5].

1.6.2.4   mpMRI and Current Clinical Implementation

As mentioned, the combination of T2-weighted imaging, diffusion-weighted imaging, and dynamic contrast-enhanced imaging are the most common combination of sequences used for mpMRI as recommended by medical experts to identify lesions suspicious for PCa [5]. For targeting PCa biopsy, the mpMRI is commonly fused with standard US imaging to guide the core biopsy after targets are identified by well-trained urogenital radiologists [24]. The radiologist assigns a rating to the suspicious region from 1-5 based on the findings in each mpMRI components. Also, different sequences are weighted differently with diffusion-weighted imaging given the most importance and T2-weighted imaging and dynamic contrast-enhanced imaging weighted about equally [5]. Currently, MRI fusion-guided biopsy is utilized during the initial biopsy procedure for patients whose insurance covers the procedure [1–3]. Otherwise, patients undergo the templated TRUS-guided prostate biopsy on the initial biopsy procedure, and if a repeat biopsy is needed, the MRI fusion-guided biopsy is then performed [94]. The MRI fusion-guided biopsy, which typically includes the 12 core templated TRUS-guided prostate biopsy procedure as a part of the platform [1,24], has recently been shown to have a greatly improved sensitivity of PCa detection compared to the 12 core TRUS-guided prostate biopsy alone [1]. Additionally, MRI fusion-guided biopsy has a higher detection rate of clinically significant high grade PCa and lower detection of clinically insignificant low grade PCa [22]. This means that a multiparametric approach can reduce the overdiagnosis and overtreatment previous mentioned.

Unfortunately, mpMRI and MRI fusion-guided biopsy has some negative attributes. To perform MRI fusion-guided biopsy, an additional appointment for the patient is required in order to acquire the approximately 40 minute mpMRI, which then has to be read by a well-trained urogenital radiologist. This adds additional time for the patient and costs. Prior hemorrhaging especially from previous prostate biopsy can affect the quality of the mpMRI [95,114], which is an important consideration as the indication is for patients with prior negative biopsy [94].

Another consideration in implementing the MRI fusion-guided biopsy is that during the biopsy distortion of the prostate may occur from the urologist compressing the prostate. This may cause false negative biopsies as the alignment of the US and mpMRI may be altered [28]. Also, if the patient moves during the biopsy once the fusion of the mpMRI and US has occurred, the fusion process has to be redone as the mpMRI is not real-time and inherently aligned with US. Lastly, once the targeted biopsies are acquired, the standard 12-core templated TRUS-guided prostate biopsy still need to be performed [5,28], and thus the core number is not reduced.

An added benefit of the current MRI fusion-guided biopsy is that many of the commercially available systems offer tracking of where the cores are acquired [28]. This can be useful for surveillance of PCa as many patients are choosing this over curative therapy [115–117]. Also, if the biopsy is negative, a better sampling may be performed in areas not previously sampled as the system tracks the location of the cores.

1.6.3 Positron Emission Tomography for PCa Imaging

Positron emission tomography is a method utilizing exogenous radiolabeled tracers that are imaged using gamma cameras. Positron emission tomography-based approaches are not used significantly for initial PCa diagnosis. The main function of positron emission tomography is for PCa staging, including identification of lymph node and metastatic involvement [118–121]. Positron emission tomography applications in PCa exploit cellular alterations, such as receptor upregulation, proliferation and metabolic changes [122,123], in conjunction with an anatomical reference such as MRI or computed tomography. As this is not a tool utilized for initial diagnosis of PCa, a table summarizing the targets of the positron emission tomography radiolabeled tracers is presented in **Table 1.**

The major limitation with these targets is the overlap between benign and PCa tissue, especially with the metabolic [123] and proliferation tracers [124]. Also, accumulation in the bladder can introduce confounding signal that impedes PCa localization in the prostate [122]. Elimination route should be a design consideration, especially if one is to use exogenous contrast agents.

1.6.4   Optical-based Imaging Modalities for Targeting Prostate Biopsy

A final imaging genre to discuss is optical-based imaging modalities. As tissue is a highly scattering medium, a limited number of optical techniques can be considered for PCa detection as the entire prostate needs to be imaged for PCa detection. The optical imaging modalities that have a minimum imaging depth in the centimeter range is PAT, i.e. optoacoustic or thermoacoustic tomography, [125,126] and diffuse optical tomography [127,128]. These methods overcome the limitation of scattering, which limits optical techniques such as confocal microscopy [125], by relying on photons in the diffuse regime, i.e. at least one scattering event occurred [129].

Optical coherence tomography has also been applied to PCa detection, but optical coherence tomography is limited to a few millimeters ($\approx$2 mm) of imaging depth as the technique is similar to US, but measures the backscatter of photons versus acoustic waves [130]. The difference in attenuation coefficient between acoustic waves and photons in tissue limits optical coherence tomography to an interstitial approach in which the prostate must be penetrated—a needle must be introduced for the optical coherence tomography probe to access the interstitial tissue. As multiple individual pathways must be performed to image a sufficient volume of the prostate, this introduces complications with precisely aligning imaging slices and the optical coherence tomography slices with the histopathology. Without exceeding the number of needles placed in the current literature, optical coherence tomography may still suffer from under-sampling [131,132]. Also as this is an invasive approach, additional risk for post-biopsy/imaging complications, especially infection, is present.

1.6.4.1   Optical Imaging Utilizing Endogenous Contrast

PAT is a relatively new hybrid imaging modality that is a combination of optical excitation and acoustic detection based on the phenomenon of the PA effect [129,133,134]. As shown in **Figure 1.4**, a PA signal is generated by absorption of light followed by a local rise in temperature which results in thermal expansion to create an acoustic wave. This acoustic wave can then be reconstructed after detection by traditional US transducer arrays [126,134,135]. Due to this PAT has been applied to many clinical topics including: fibrosis [136,137], the neurological system [138–141], the female reproductive tract [142–144], breast cancer [145–

149], the gastrointestinal system [150,151], melanoma [152–156], atherosclerosis [157–161], PCa [162–171], and the urological system [172–178].

An inherent benefit of PAT as described here is the use of an US transducer array to collect the PA signal [126,134,135]. US, as discussed above, is the primary tool for guiding prostate biopsy [1–4,15], and is thus well integrated and understood in the urology clinic. With the incorporation of a short-pulsed laser, a necessary data acquisition system, and computer for synchronization and image display, a simple PAT system is made. Additionally, a cyclic acquisition of PAT and then US-only images can be acquired [134]. Therefore, an US anatomical reference can be displayed simultaneously with the PAT images.

The resulting PA signal is dependent on a few parameters as $p_0 = \varepsilon\mu_a\Gamma F$, where ε is the imaging system constant, μ_a is the absorber's absorption coefficient, Γ is the Gruneisen parameter, and F is the local photon fluence [126,129]. For the user, the primary parameters to control are the light fluence and absorption coefficient (**Fig. 1.5**), which is done by carefully selecting the wavelength, light delivery including density of irradiation, and target absorber. Currently, a limited number of endogenous biological contrasts are available targets, which includes: hemoglobin (oxy- and deoxyhemo-globin), melanin, lipid, collagen, and water [126,179]. To optimize light fluence in a biological system, wavelengths are typically chosen where a "window" in which water absorption is minimized [126,146,168,180–182]. This can be seen highlighted in **Figure 1.5** below.

The imaging resolution of PAT is typically limited by the US resolution, which can range from 50 – 300 μm depending on the frequency of the US transducers. As mentioned above in the discussion of US-based imaging methods, the typical US probe for prostate imaging ranges in frequencies of 5 – 9 MHz [50,57,59], but recent efforts have resulted in higher frequency US probes of up to 29 MHz [61,62]. The excitation volume is not limited to the US frequency, and thus sub-US resolution molecules can be imaged.

In regards to the application of PAT to PCa detection, PAT has been recently applied *in vivo* in humans for the purpose of evaluating angiogenesis in PCa compared to benign tissue [171]. Preclinical studies in canines [168,183] and mice [164,184] have demonstrated the ability to discern PCa or PCa pseudo-lesions from benign tissue which analysis including PA frequency and PA single and multispectral signal intensity analysis. Other applications of PAT or PA's application to human prostate samples have been on haemotoxylin and eosin stained, 100

μm thick tissue slices [185] and to prostates before [169] and after they were axially sectioned following radical prostatectomy [163,182,186].

While these are steps toward the translation of PAT to the urology clinic, these studies leave some unanswered questions to the feasibility. For example, the barrier of light delivery to the whole prostate has yet to be overcome [171]. As light scattering is high from the rectal wall while the anisotropy is high [187], a novel route to deliver the laser pulses may be needed [188]. An alternative to transrectal light delivery is interstitial [169,189] or transurethral light delivery [165,190]. These routes have been tested without [169] and with PA absorbers that achieve a high signal-to-noise ratio, such as brachytherapy seeds [190], titanium wire [189], and pencil leads [165].

Another consideration for PAT for PCa detection besides light fluence is the other variable of the PA signal amplitude which can be controlled—the absorption coefficient or the absorber. As shown in Figure 1.5, the absorption coefficient changes with wavelength. An optimized wavelength can be chosen to ensure the balance of light penetration and absorption. The primary absorber thus far for PCa detection has been hemoglobin [168,171,183] as angiogenesis is a known major component of clinically significant PCa tumors [76,77]. Other endogenous absorbers include lipid and water [182]. Lipid storage is known to be increased in PCa specifically, but only by approximately 5% [191]. As only a few endogenous absorbers are available, development of targeted exogenous absorbers is another potential for PCa detection with PAT [179,192–195], but these are currently limited in the clinical setting.

Lastly, the current studies imaging endogenous contrast *in vivo* or *ex vivo* human prostates have yet to provide suspicious regions as targets for the prostate biopsy. Dogra and colleagues have applied multiple image analysis techniques to a dataset of multispectral PAT and US images of axially-sliced human prostates following radical prostatectomy [163,186,196]. While differences in endogenous absorbers are shown, biopsy targets are not provided. Also, the images are taken in such a way that axial plane of the prostate specimens have a uniform light fluence and the PA signal is acquired with a C-scanning US transducer array [196]. The current US transducers used for the prostate biopsy are B-scanning [4,15], and the methods of light delivery do not allow for completely uniform light delivery across the axial plane of the human prostate [165,171,197]. *In vivo* PAT imaging of the human prostate has shown the ability to

correlate PAT signal with angiogenesis and tissue vascularity. No prostate biopsy targets were given from these measurements [171].

1.6.4.2   Optical Imaging Utilizing Exogenous Contrast

To date the techniques utilizing an exogenous contrast for PCa detection is fluorescence diffuse optical tomography [128,198] and PAT [192–195], which are typically performed in a multimodal manner as an anatomical reference is necessary [128,192–195,198]. Diffuse optical tomography and PAT differ in the mechanism of signal generation. Diffuse optical tomography is a pure optical technique in which a fluorescent label is optically excited, and the resulting emitted light is detected [128,198]. Alternatively as mentioned above, PAT is a hybrid imaging modality in which the exogenous contrast agent's absorbed optical energy is converted to heat. The resulting thermodynamic expansion then creates an acoustic wave that is detectable by traditional clinical US transducers (Figure 1.4) [133,134]. As these approaches utilize exogenous contrast, the procedures would take more clinical time for the prostate biopsy, since the exogenous label needs to bind to its target [128,192–195,198], compared to the MRI fusion-guided or templated TRUS-guided prostate biopsies.

Fluorescence diffuse optical tomography has been demonstrated to image over 2 cm in prostate phantom with optical tissue-mimicking properties using an integrated TRUS probe. A single capillary tube of indocyanine green fluorescent label encapsulated in lipid droplets was used as the control imaging target. The TRUS probe had four integrated sensors for fluorescent detection [128]. Reconstruction may be an issue for this method if more than one imaging target was in the phantom prostate [198], which would be a concern for translation as multifocal PCa is common and non-specific binding would be expected for an exogenous contrast agent. While the reconstructed images provide agreement with the phantom [128], no work has been completed *in vivo* or with human radical prostatectomy specimens for fluorescence diffuse optical tomography.

PAT has an advantage over diffuse optical tomography as the signal detector for the PA signal is an US transducer [134], which is already utilized for the current gold standard prostate biopsy procedure [1–4,15], while diffuse optical tomography needs an optical sensor to collect the signal [128,198]. In addition, PAT can image deeper than diffuser optical tomography as acoustic attenuation is lower than optical attenuation in biological tissue [135]. Compared to

endogenous PA contrast in the prostate, exogenous contrast agent targets, such as PSMA [192,193], could provide more specificity than endogenous hemoglobin imaging. Also, exogenous contrast agents have the potential to be optimize to further increase the imaging depth beyond the estimated optical extinction [199].

For the application of PAT of exogenous contrast for the prostate biopsy, the topics of light delivery, as discussed in the previous subsection, is still needed to be improved for this approach. Also, an imaging analysis method is similarly needed for identifying suspicious regions that can be used as targets for the prostate biopsy. This image analysis method would need to be potentially capable of real-time analysis to enable real-time display of the images to be easily integrated into the current workflow of the templated TRUS-guided prostate biopsy [4,15].

1.7   Summary

To date, no improvements in prostate biopsy have been incorporated to improve the under-sampling issues present in the current method of 12-core templated TRUS-guided prostate biopsy without the use of additional imaging that requires a separate appointment and added personnel. While there is added costs and appointments needed for the MRI fusion-guided biopsy, the sensitivity of the prostate biopsy is improved along with more clinically significant PCa detected [1−3]. This success is due the combination of PCa characteristics, such as blood flow dynamics and density, water motion restriction or increased cellularity, and anatomical alterations, which are assessed with this imaging modality along with a more quantitative nature of the diffusion weighted and dynamic contrast-enhanced imaging [2,5,28]. While much of these characteristics have also been attempted with US imaging modalities [15,67,74,81,85], the imaging resolution of the lower frequency US transducer arrays has had limited the success [57,59,62]. To overcome this, exogenous contrast agents have been employed [84,87], but limitations still exist due to the difficulty to image the entire prostate while trying to observe the blood flow dynamics [90].

A need exists to develop a real-time, multiparametric imaging tool that can be utilized in the urological clinic to guide prostate biopsy without adding significant burden to the clinical workflow so that it may be incorporated as first line for biopsy acquisition. By fulfilling this need an improvement of the biopsy sensitivity may be achieved along with better acquisition of

the most clinically significant prostate tissue without added appointments nor significant cost increase. This would then lead to improved pre-surgical diagnosis and improved decision making for active surveillance versus curative therapy as the large majority of men die with PCa and not from it [37]. The imaging tool will hopefully reduce the need for repeat biopsy and therefore lower the patient's risk of developing a post-biopsy complication within their lifetime.

1.7.1 Proposed Engineering Solutions for the Current Investigation

The proposed engineering solutions will include 1) a multiparametric approach to improve the sensitivity and specificity of identifying PCa ROI for the purpose of a targeted prostate biopsy, 2) an optimized, real-time imaging approach to ensure visualization of the most frequent prostate regions that give rise to PCa, 3) a non-invasive approach to minimize post-biopsy complications, and 4) a realistic experimental model to ensure accurate conclusions from the study.

We hypothesize that the development of a multimodal, multiparametric, real-time imaging system which includes US and PAT will improve prostate biopsy sensitivity and deliver better representative core sampling of the diseased tissue. As discussed PAT is inherently a multimodal technique as the US transducer array is necessary to collect the PA signal [126,134].. Based on previous simulation results [188] and *in vivo* prostate imaging [171], a transurethral light delivery approach will be explored to deliver light to the whole prostate simultaneously so that anterior regions of the prostate can be imaged with PAT. Utilizing a multi-wavelength approach, the major endogenous absorbers for PCa will be assessed. The minimum necessary wavelengths will be utilized to limit computational burden of the analysis method, which will ultimately provide potential targets for the prostate biopsy without user selection. By completing these tasks, a prostate PAT will be developed for testing *in vivo* for endogenous contrast imaging, and the imaging system will provide a mechanism for testing exogenous contrasts agents that are being developed [192–195].
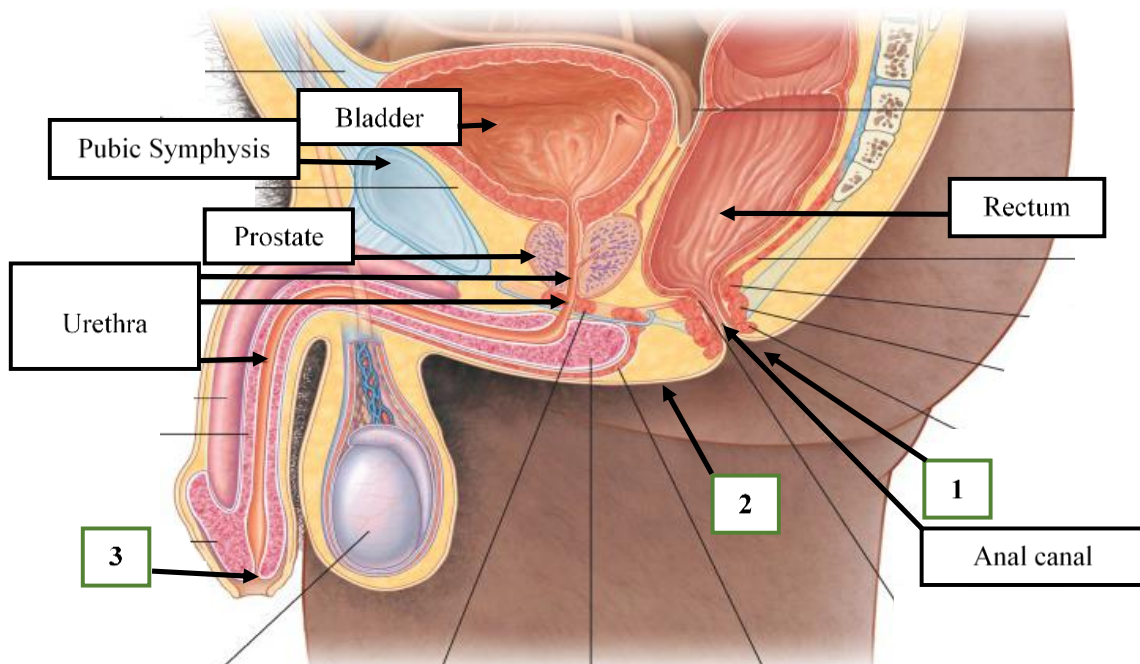
Figure 1.1. Gross male pelvic anatomy with median sagittal view. Major structures labeled are for general anatomical reference. Relative size of structures may vary by person. (1-3) Transrectal, transperineal, and transurethral locations for accessing the prostate. Image was adapted from Gray's Atlas of Anatomy, Second Edition [200].
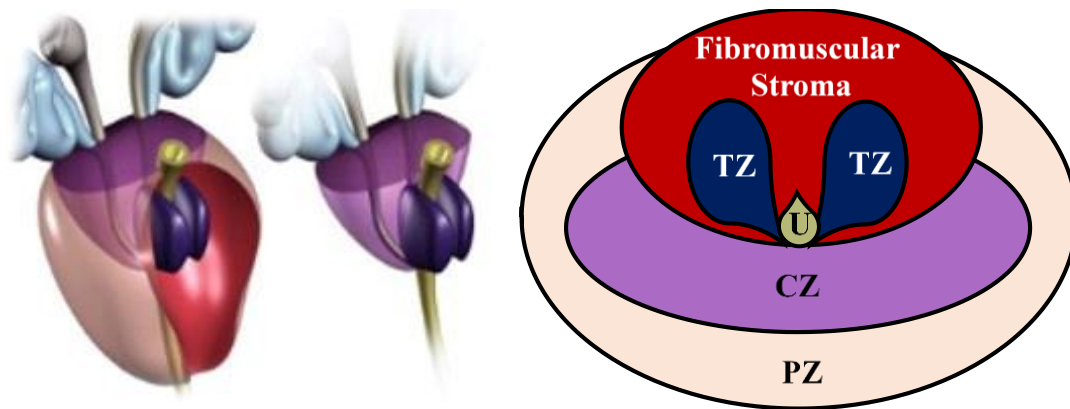
Figure 1.2. Prostate zonal anatomy. This figure was adapted from the original located in Genitourinary Pathology: Foundations in Diagnostic Pathology [39]. Above left is a three-dimensional representation of the prostate zonal anatomy. A corresponding axial slice is depicted on the above right. The peripheral zone (beige/light pink), central zone (purple), transition zone (navy blue), fibromuscular stroma (red), urethra (green), and seminal vesicles (light blue) can be seen relative to one another.
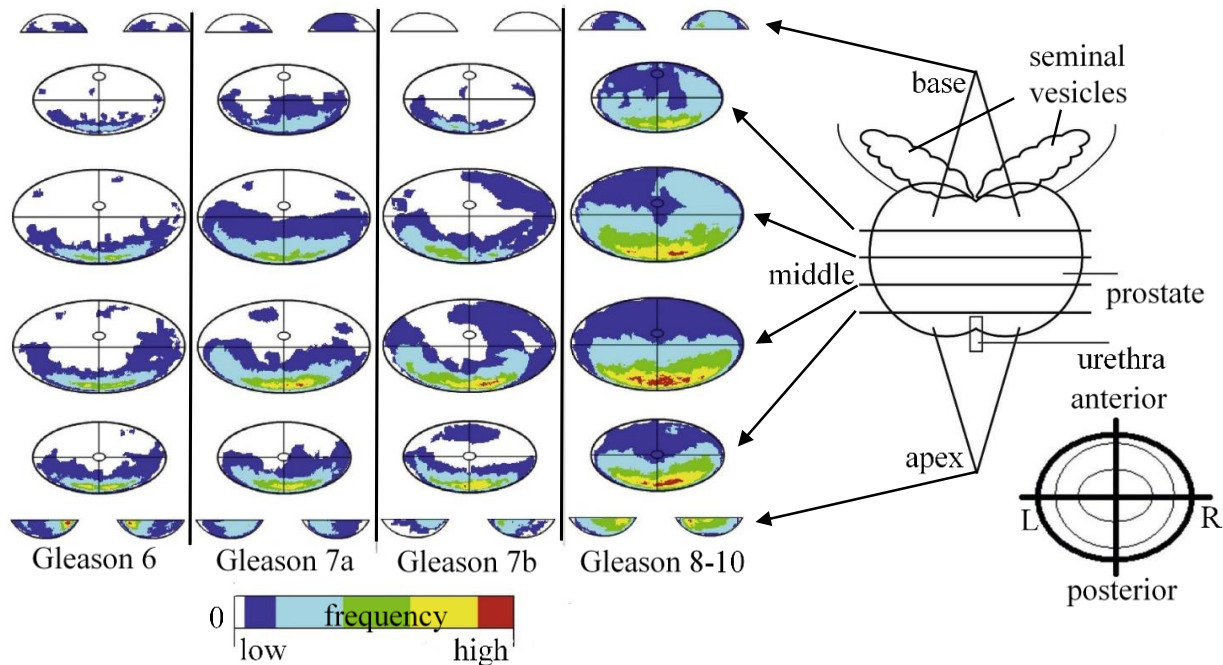
Figure 1.3. Distribution of PCa based on Gleason score. This figure was adapted from original article by Eminaga et al. [201]. No data was altered, but layout and text were altered for clarity here. To the right of the figure, a schematic drawing is shown of the relative location the heat maps represent for anatomical orientation. On the left half of the figure, the heat maps show the frequency distribution of the various Gleason scores. These were determined from 168 prostates following radical prostatectomy. Each prostate could exhibit more than one Gleason score. As these specimens were from radical prostatectomy cases, the frequencies are biased towards cases that needed curative therapy and were surgical candidates, but the distribution represents literature well. Gleason 7a = 3+4. Gleason 7b = 4+3.

Table 1.1. Summary of positron emission tomography radiolabeled tracers for locating PCa.

Category	Tracer	Rationale
Metabolism	18F-FDG [122,123]	Warburg effect [76].
Proliferation	18F-ACBC [124,202,203]	Increased amino acid transport.
	11C-Choline/ 18F-FC [119,204,205][120]	Increased cell membrane synthesis.
	11C-Acetate [122][121,206]	Increased cell membrane synthesis.
Receptor Upregulation	Radiolabeled PSMA antibody [207,208]	Epithelial glycoprotein upregulated in all PCa stages; associated with metastasis and recurrence [209].
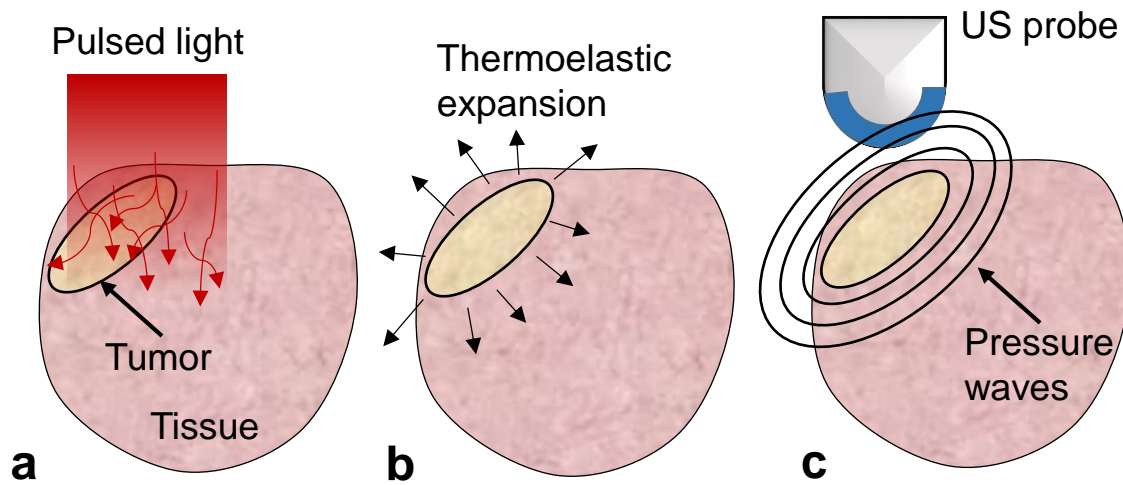
Figure 1.4. Principle of PAT. (a) Light propagates through tissue until absorption occurs. (b) The absorbed energy causes a local temperature rise which causes thermoelastic expansion for the absorber. (c) The expansion causes an acoustic wave to propagate which can be detected with US transducer arrays. Figure adapted from L. V. Wang and J. Yao [134].
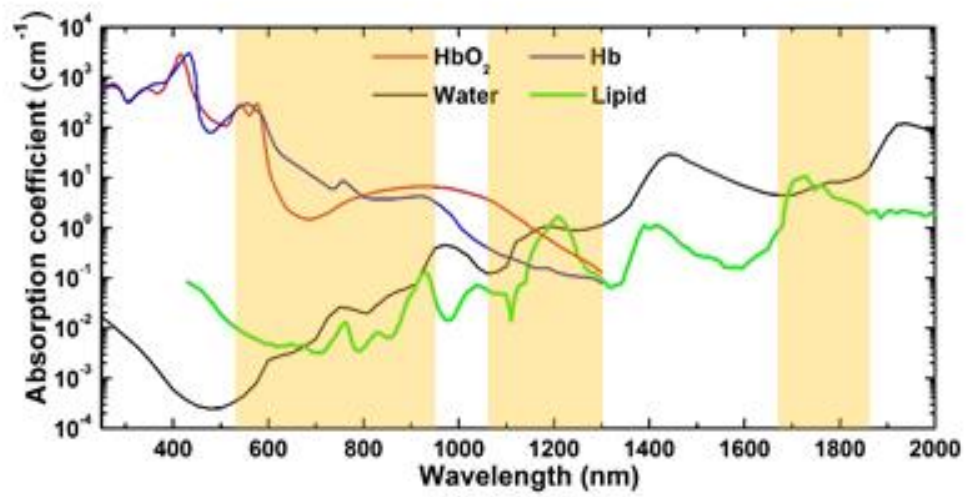
Figure 1.5. Endogenous PA absorbers' absorption coefficients at different wavelengths. Original figure from Hui et al. altered to highlight wavelengths with valleys in the absorption of light by water [126].

2. COMPARISON OF PHOTOACOUSTIC TOMOGRAPHY DEVICES FOR IMAGING EX VIVO HUMAN PROSTATES

*A portion of the contents of this chapter and all of the next chapter (Ch. 3) has been previously published in *Photoacoustics* [162]. This work was reformatted for dissertation, and additional data has been added to this chapter that were outside of the scope of Bungart *et al.* [162].

2.1 Introduction

PCa is the most incident, visceral cancer in USA men. An estimated 164,690 new PCa cases are predicted to occur in 2018, which is 9.5% of all estimated 2018 cancer occurrences [210]. The current overall 5-year survival rate is 97.7%, especially when PCa is discovered at a local stage, but this drops to 30% if the PCa has metastasized prior to diagnosis [6]. In order to ensure that diagnosis occurs at the local stage while limiting harm to the patient, serum PSA measurement is recommended as a screening tool for PCa depending on factors, such as age, family history and the patient's preference [211,212]. PSA is produced exclusively by prostate epithelial cells and can be influenced by benign conditions including: bacterial prostatitis [9], ejaculation [11], and BPH [12]. Thus, false positive results from PCa serum PSA screening commonly occur, which makes a follow-up, confirmatory test necessary.

Currently to confirm the presence of PCa, histopathology analysis with Gleason grading must be performed on biopsy samples acquired from the prostate in order to guide clinical decision making [213]. Gleason grading is based on the microscopic tissue architecture, and the two major Gleason grades are added to give the Gleason score [35]. The current clinical standard for acquiring biopsy samples is to perform a 12-core TRUS-guided biopsy, which entails following a template to systematically acquire 12 tissue samples from the prostate [4]. To follow the template protocol, a TRUS probe guides the biopsy procedure by allowing visualization of the anatomical locations within the prostate [4,15]. Even with optimization of the TRUS-guided biopsy, false negative results occur in approximately 15-34% of initial biopsy procedures due to the limited, untargeted sampling of the prostate [49,214].

The combination of the PSA and the TRUS-guided biopsy is considered to be the major contributor to the overtreatment problem for PCa [211]. Since the biopsied tissue, and not the PSA, currently provides the diagnostic information to aid in therapeutic decision making [35], the biopsy procedure needs improvement due to its low sensitivity [18]. As previously mentioned, the current gold standard for performing the biopsy is a systematic approach based on a template [4]. Therefore, providing a target for the prostate biopsy may help to improve the sensitivity of the procedure.

The most notable clinical advancement for targeting the prostate biopsy is the MRI fusion-guided biopsy, which is currently recommended for patients undergoing repeat biopsy following an initial negative biopsy [16,17]. For biopsy-naïve patients, recent conflicting evidence exists regarding the PCa detection rate when using the MRI fusion-guided biopsy compared to TRUS-guided biopsy [21,25,26,215–217]. Overall, these clinical studies show that the MRI fusion-guided biopsy alone can reduce the number of cores needed to achieve the same PCa detection rates as the TRUS-guided biopsy [25,26,215]. Additionally, the MRI fusion-guided biopsy has been shown to miss fewer clinically significant PCa tumors [25]. This reduction in cores needed and detection of clinically significant PCa tumors can reduce the risk of side effects and the need for repeat biopsy. However, many pitfalls exist with this method. Careful calibration is needed to fuse the real-time US and previously acquired, annotated mpMRI. If the patient moves after alignment, the calibration must be completed again. In addition, the mpMRI images are static, and manual pressure on the prostate during biopsy can distort the tissue compared to the mpMRI [28]. Other pitfalls include added costs for the mpMRI [29] and the injected contrast agents, which may be contraindicated in some patients [30], used in the procedure. Thus, an ideal solution for targeting the PCa biopsy includes endogenous contrast and real-time, coincident imaging and analysis.

Since the prostate biopsy is TRUS-guided, PAT, which uses traditional US transducer arrays for signal collection [134], is a potential tool to apply clinically in order to improve the prostate biopsy. In contrast to MRI fusion-guided biopsy, PAT has inherent co-registration with the US imaging channel as the PAT and US images are sequentially acquired using the same US transducer array. MRI fusion-guided biopsy does have an advantage in imaging resolution and difference in biomarker type compared to PAT for prostate biopsy targeting. For PAT, the imaging resolution is dependent on the US transducer's imaging resolution [134]. Since the

TRUS probe used for prostate biopsy is typically a low frequency US transducer with central frequency at approximately 7 MHz [218], the axial resolution is approximately two to three times lower than the resolution of the mpMRI sequences used for the MRI fusion-guided biopsy [5]. Another potential major difference is that the recommended mpMRI utilizes two functional imaging sequences out of the three total sequences as biomarkers [5], while PAT approaches can be based on biomarker content [126,219] and/or functional alterations [220]. Overall, PAT should be investigated as an alternative to MRI fusion-guided biopsy for the purpose of targeting the prostate biopsy.

The PA signal detected during PAT results when an absorber interacts with pulsed light in such a way that the energy is converted to heat, and the resultant local thermodynamic expansion releases an acoustic wave, which is detectable via an US transducer [134]. Compared to traditional optical-only imaging techniques, this allows for deeper imaging of major endogenous absorbers, such as de-oxygenated and oxygenated hemoglobin, lipid, and water [126,134]. A few examples of the applications in which these endogenous PA contrast agents have been used are intravascular imaging of atherosclerotic plaques [221], breast cancer tumor margin assessment [146], and PCa [171] and breast cancer [222] vascularity. Since PCa is known to involve angiogenic processes [76], PAT, with hemoglobin as the endogenous contrast agent [126,134], may be able to identify targets for the prostate biopsy. Thus, we will utilize the 1064 nm output from our previously published barium nitrite Raman laser [223] to image hemoglobin in human prostates. Unfortunately, angiogenesis in the prostate is not specific to PCa [76], while increasing cholesteryl ester, i.e. lipid, storage has been shown to be a specific biomarker to increasingly aggressive PCa [191]. Therefore, PAT was also performed at 1197 nm, which is an absorption peak for lipid [126,223].

To determine the ability for 1064 nm and 1197 nm PAT to differentiate benign from malignant tissue for the purposes of guiding the prostate biopsy, a prostate PAT device needs to be optimized. Up until 2016 PAT imaging of human and animal prostates included PAT devices in which the US detector and light source were external to the prostate [167,168,182,224], or an interstitial [189,225] light source with external US detector were used. For simplicity purposes, we aim to develop a PAT device with combined illumination and US detection so that scanning of the *ex vivo* human prostates results in relatively consistent illumination between each PAT image. Two common optical and acoustic device setups are the co-linear orientation and the use

of a bifurcated fiber bundle mounted to the sides of the US probe [134]. Here we test these device setups to determine the optimal design for *ex vivo* imaging of human prostates in order to test the ability for 1064 nm and 1197 nm PAT and US imaging to identify prostate biopsy targets.

2.2   Methods

2.2.1   Fabrication of PAT illumination and US detection devices

Parts to mount to the low frequency US probes were designed in Solidworks (Dassault Systèmes, Boston, MA, USA) and fabricated using a three-dimensional printer. Two US probes were used. For the device designs involving a bifurcated fiber bundle, the C9-5ICT TRUS probe (Philips, Andover, MA, USA), while a L7-4 US probe (Philips, Andover, MA, USA) was used for the co-linear device design.

2.2.2   Performance testing of PAT illumination and US detection devices

Devices were incorporated into the 1064 nm and 1197 nm PAT and US system (**Fig. 2.1**) [226]. The laser source included the previously published barium nitrite Raman laser [223], which is pumped with a 10 Hz Nd:YAG laser (Continuum, San Jose, CA). An US system (Verasonics, Kirkland, WA) was used with the US probes to collect the PA signal and perform US imaging.

The PAT and US imaging devices were compared using targets that generate a strong PA signal, such as heat shrink tube and tungsten wire, and that represented endogenous contrast, such as human blood and polyethylene tubing. The targets were embedded in an agarose gel (CN: 16500500, Invitrogen, Carlsbad, CA, USA). Imaging depth, pSNR, and the imaging resolution were measured. A minimum of 3 independent measurements were used for statistical analysis.

2.3   Results

2.3.1   PAT/US imaging probe with reflected emission from a bifurcated fiber bundle

A C9-5 US probe was outfitted with a three-dimensional printed cover that had internal grooves to hold the bifurcated fiber bundle. The US probe was placed into the cover with

attached bifurcated fiber bundle so that the fiber bundle was parallel to the US transducer array's imaging plane (**Fig. 2.2a,b**). To help direct the light output towards the acceptance plane of the US transducer array, two mirrors were glued to the US probe cover. The 1197 nm PAT imaging depth of the PAT/US probe was then tested using 100 μm tungsten wire embedded in 2.5% agarose gel (**Fig. 2.2c**). The maximum energy output of 1197 nm from the laser, which was 80 mJ/pulse, was used. The output energy from the bifurcated fiber bundle was 25 mJ/pulse. Thus, the coupling energy was 31.25%. US imaging (**Fig. 2.2d**) was able to observe all of the tungsten wires in the agarose gel. The corresponding 1197 nm PAT imaging (**Fig. 2.2e**) only acquired signal from the top 3 wires, which were up to approximately 1 cm deep. The wires deeper than 1 cm did not have detectable 1197 nm PA signal.

2.3.2   Co-linear PAT/US imaging probe

To ensure the light emission illuminates the acceptance plane of the US transducer array, a co-linear setup was designed (**Fig. 2.3a**). Glass slides were used to reflect the acoustic waves to and from the L7-4 US transducer array, while the light propagated through a glass slide to the sample. By including the glass slides, the distance from the fiber bundle to the tissue surface is increased. To minimize light absorption, deuterated water was used as it has a very low absorption coefficient compared to normal water [227]. To correct the light expansion from the fiber bundle (**Fig. 2.3b**), cylindrical lens with a 13.7 mm focal length (LJ1909L1-C, Thorlabs, Newton, NJ, USA) were placed directly after the fiber bundle. The fiber bundle and cylindrical lens were held in place with a custom three-dimensional printed holder. The cylindrical lens created a focusing point approximately 1 inch from the holder (**Fig. 2.3c**), which was just under the tissue surface. The fiber bundle and cylindrical lens output energy efficiency for 1197 nm was 28.6%. Since the glass slides were not coated with an anti-reflection coating, a fraction of the energy is expected to be reflected from the glass. The reflected amount was measured to be 20%. After included this energy loss, the total effective output energy efficiency for 1197 nm was 22.9%.

After assembling the co-linear PAT/US device (**Fig. 2.3d**), the 1197 nm PA and US pSNR was determined for 3 mm heat shrink tube, 1.22 mm polyethylene tube, and 1.5 cm diameter sphere of butter (**Fig. 2.3e**). The samples were placed close to the bottom of the co-linear PAT/US device. Three frames were averaged per image and analyzed. The US pSNR was

insignificantly different for the heat shrink tube and butter samples. A statistical difference was detected between the heat shrink tube and polyethylene tube US pSNR and the polyethylene tube and butter US pSNR. Overall, The US pSNR was around the same level of 85 dB. The 1197 nm PA pSNR for the heat shrink tube was approximately twice as high as the US pSNR for polyethylene tube and butter, which were insignificantly different.

2.3.3   PAT/US imaging probe without reflected emission from a bifurcated fiber bundle

The final PAT/US probe design tested was similar to the setup in section 2.3.1 (**Fig. 2.2a**), except that mirrors were not used. Instead, a bifurcated fiber bundle was fixed to the US probe at the end, parallel to the transducer array, with a 30° angle relative to the probe, thereby creating a focus of approximately 1 cm by 2 cm at 1 cm from the US transducer (**Fig. 2.4a**). The surface area per bifurcated fiber bundle end is 13 mm by 3 mm. With an energy output per bifurcated fiber bundle of 27.5 mJ/pulse, the total energy output was 55 mJ/pulse. Based on the fiber bundle end surface area and energy output, the energy density maximum was 70.5 mJ/cm^2. Thus, the fiber bundle setup and energy output is acceptable as the maximum permissible exposure for this laser is 100 mJ/cm^2 [228].

For PAT, the TRUS probe determines the imaging resolution. We assessed the C9-5ICT TRUS probe's US and PAT beam full width at half maximum (FWHM) with a custom sample holder (**Fig. 2.4b**) which contained 25 micron tungsten wire at 11, 19, and 26 mm from the transducer (**Fig. 2.4c**). As expected, the US axial FWHM remained relatively constant over depth while the lateral FWHM increased (**Fig. 2.4d,e**). The PAT axial FWHM was larger compared to US while the PAT lateral FWHM was similar to US, except at 19 mm. These results are consistent with expected resolution for a TRUS transducer array with a center frequency of 7.8 MHz.

Lastly, the pSNR of the PA absorbers' US and 1064 nm and 1197 nm PAT were assessed using phantoms (**Fig. 2.4f**). Heat shrink tube is a broad-spectrum, strong absorber used here as a control, while polyethylene tube and coagulated human blood that was 1-2 hrs old in 1% agar gel was used for the prostate biomarkers of lipid and hemoglobin. Coagulated blood that was 1-2 hrs old was used as a sample since the blood in the resected human prostate specimens is expected to be coagulated. Additionally, the human prostate specimens will be imaged approximately 1-2 hrs after resection. The pSNR for blood, heat shrink tube, and polyethylene tube was shown to be

statistically different between all imaging channels. The US pSNR was within 10 dB for all the samples, while the PAT pSNR varied more between samples. The heat shrink tubing has the highest PAT pSNR. For blood the 1064 nm PAT pSNR was 6 dB higher than the 1197 nm PAT pSNR. The opposite was found for polyethylene tube with the 1197 nm PAT pSNR being 6 dB higher than the 1064 nm PAT pSNR.

2.4   Discussion and conclusions

For the proposed *ex vivo* human prostate study to determine if 1064 nm and 1197 nm PAT and US imaging can target the prostate biopsy, a PAT/US imaging probe needs to be optimized. The human prostate can be up to 5 cm in the anterior-posterior dimension [42]. Due to this the mirrored bifurcated fiber bundle probe design cannot be used since the PAT imaging depth was limited to approximately one cm. In comparison, the non-mirrored bifurcated fiber bundle design of the PAT/US imaging probe detected blood, a more weakly absorbing imaging target than tungsten wire, at a depth of at least 18 mm. The co-linear PAT/US imaging probe design was not tested beyond 10 mm of imaging depth.

In addition to imaging depth, the pSNR for 1064 nm and 1197 nm needs to be as high as possible to ensure the ability to distinguish contrast, especially since the changes in lipid from benign to malignant prostate tissue is a few percent change [191]. For the co-linear PAT/US imaging probe, the 1197 nm PAT pSNR was at least 10 dB lower for polyethylene tube than the bifurcated fiber bundle design without mirrors. The difference in pSNR is likely due to the difference in energy fluence at the sample. As the light fluence will decrease over depth and that the PA signal is directly correlated to the light fluence [126,129], the bifurcated fiber bundle PAT/US imaging probe without mirrors is the best option for the proposed *ex vivo* human prostate study for the purpose of determining if 1064 nm and 1197 nm PAT and US imaging can provide targets for the prostate biopsy.
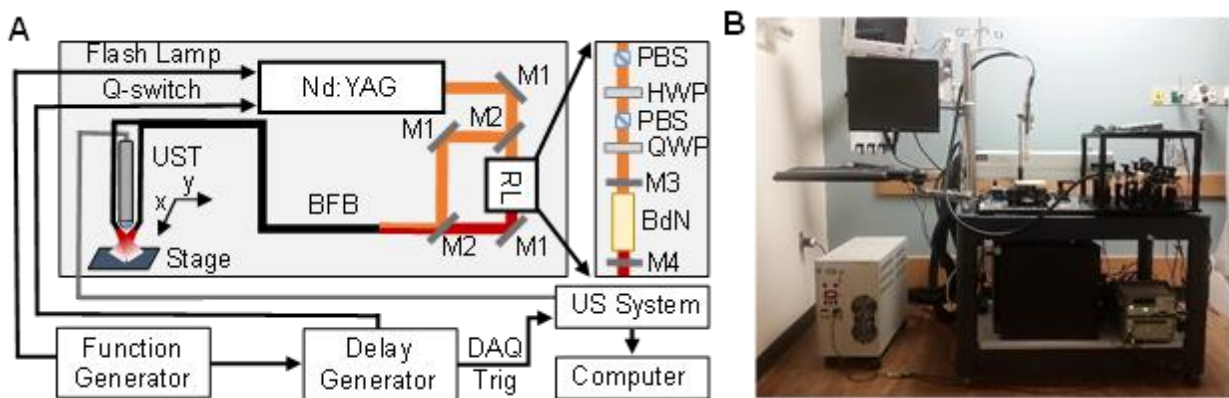
Figure 2.1. PA and US Tomography Imaging Setup. (a) Schematic of PAT and US imaging system. M1: 45 degree reflective mirror; M2: flip-mounted 45 degree reflective mirror; M3: resonator end mirror; M4: output coupler; PBS: polarizing beam splitter; HWP: half wave plate; QWP: quarter wave plate; BdN: barium dinitrite crystal; BFB: bifurcated fiber bundle; UST: ultrasound transducer; DAQ: data acquisition system. (b) Image of PAT and US imaging system at location in Indiana University Hospital near surgical suite for optimized tissue handling.
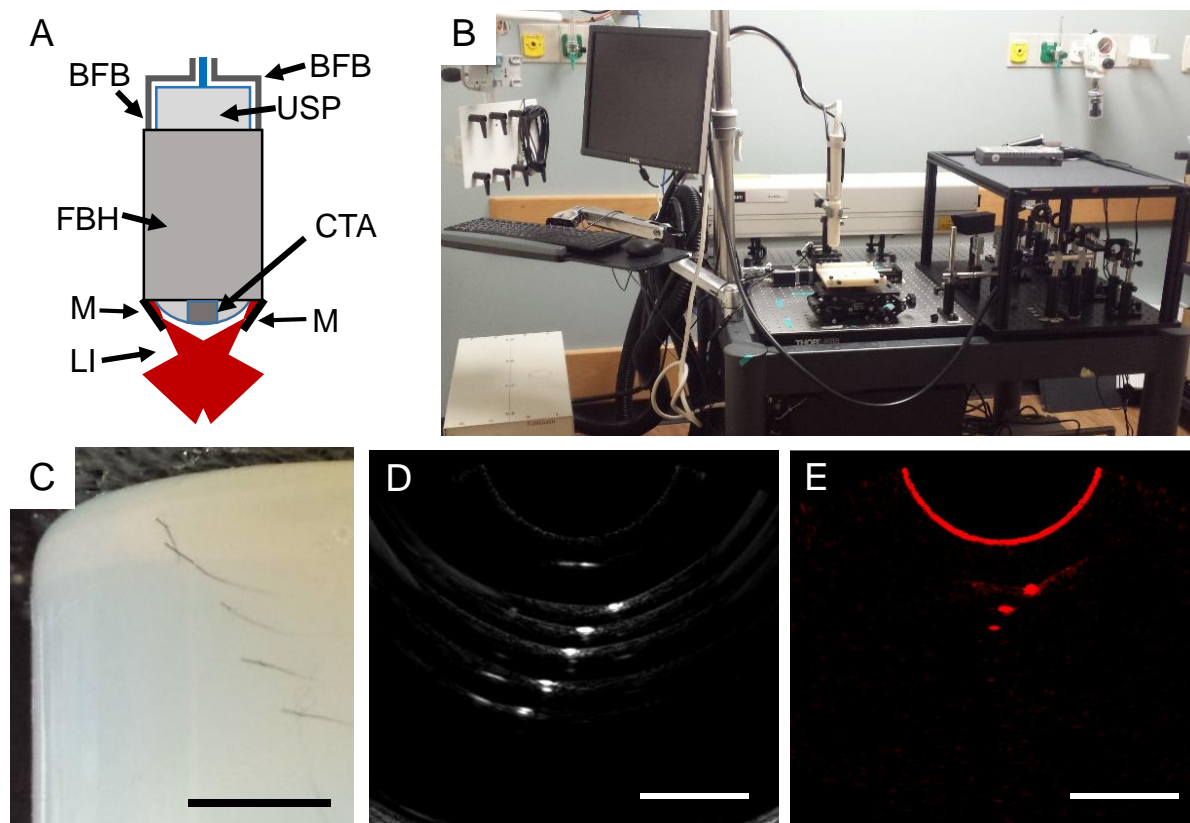
Figure 2.2. PAT/US imaging probe with reflected emission from a bifurcated fiber bundle. (a) Schematic of PAT/US imaging probe with reflected emission from a bifurcated fiber bundle. BFB: bifurcated fiber bundle; USP: ultrasound probe; FBH: fiber bundle holder; CTA: curved transducer array; M: mirror; LI: light illumination. (b) Picture of imaging probe installed on system at IU Hospital for testing. (c) Picture of the tungsten wire embedded in agarose gel shown in the (d) US image and corresponding (e) 1197 nm PAT image. Scale bars: 1 cm.
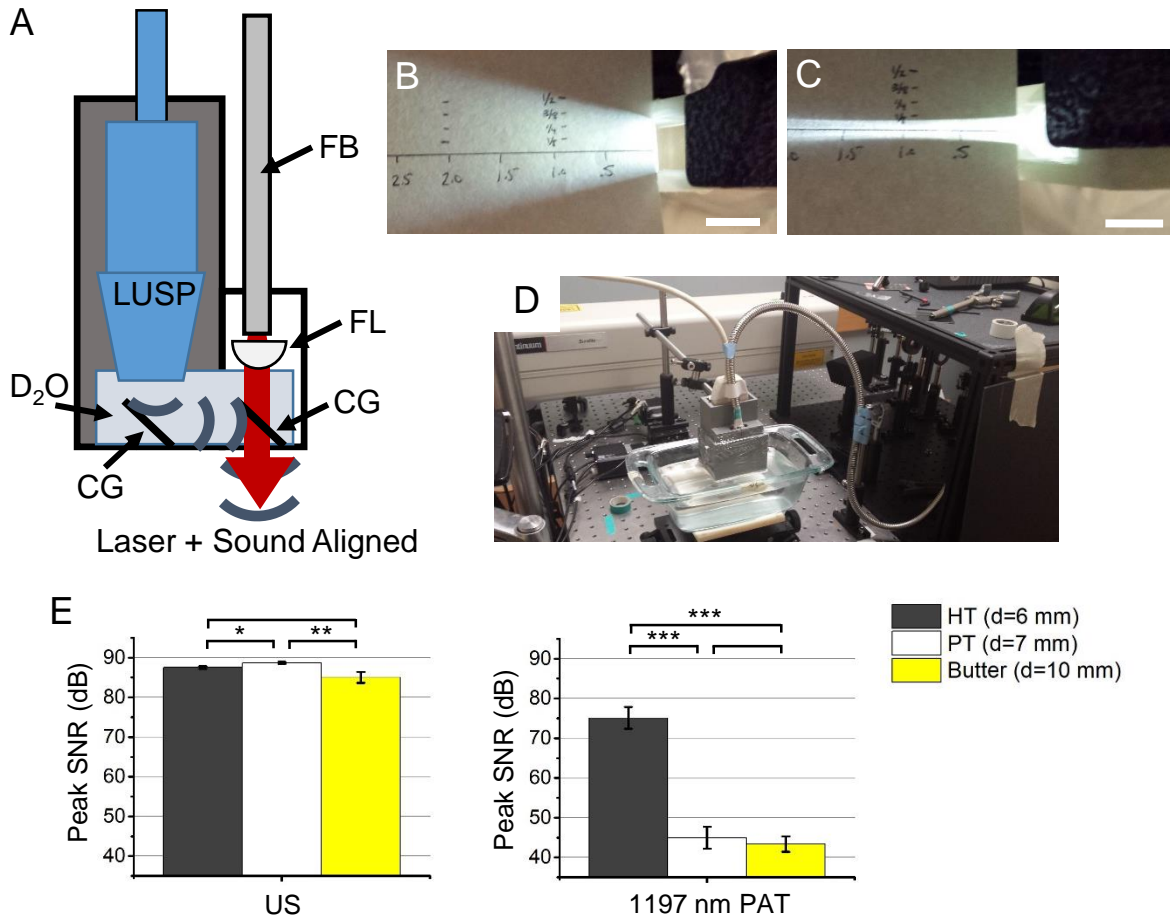
Figure 2.3. Co-linear PAT/US imaging probe. (a) Schematic of the co-linear PAT/US imaging probe. FB: fiber bundle; LUSP: linear ultrasound probe; FL: focusing lens; D2O: deuterated water; CG: cover glass. (b) Light emission from fiber bundle without and (c) with cylindrical focusing lens. Scale bars: 1 in. (d) Picture of the co-linear PAT/US imaging probe installed on the system at IU Hospital for testing. (e) US and 1197 nm PAT pSNR for heat shrink tube (HT), polyethylene tube (PT), and butter samples. D = depth of sample from the bottom of the co-linear PAT/US imaging probe. Each group has n greater than or equal to three; * = p < 0.05; ** = p < 0.001; *** = p < 0.0001.
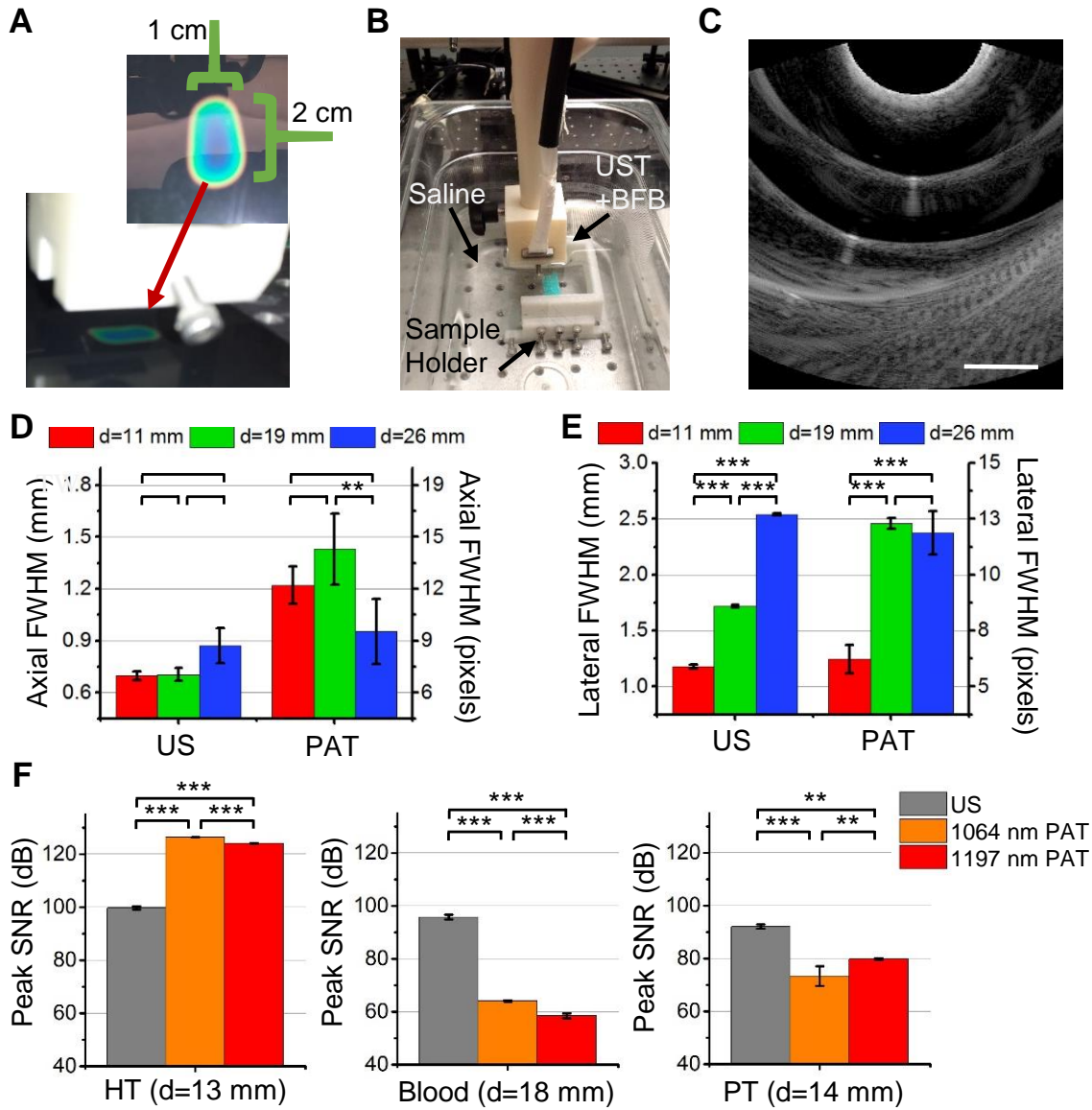
Figure 2.4. PA and US Tomography Imaging System Performance. (A) Illumination area of 1064 and 1197 nm pulsed laser light at 1 cm from the fiber bundle ends. (B) Experimental setup to determine imaging resolution. UST + BFB: ultrasound transducer with bifurcated fiber bundle. (C) Representative US image of 25 micron tungsten wire. Wires were centered relative to the transducer array for analysis. Each group has n = 5. Scale bar: 1 cm. (D,E) Axial and lateral resolution of the US and PAT system when imaging 25 micron tungsten wire at depths (d) of 11, 19, and 26 mm below the US transducer array. (F) pSNR of 1064 and 1197 nm imaging of heat shrink tube (HT), polyethylene tube (PT), and coagulated human blood. Applies to all panels: each group has n =5; ** = p < 0.001; *** = p < 0.0001.

3. PHOTOACOUSTIC TOMOGRAPHY OF INTACT HUMAN PROSTATES AND VASCULAR TEXTURE ANALYSIS IDENTIFY PROSTATE CANCER BIOPSY TARGETS

*All of this chapter and a portion of the previous chapter (Ch. 2) has been previously published in *Photoacoustics* [162]. This work was reformatted for dissertation, and additional data has been added to chapter two that were outside of the scope of Bungart *et al.* [162].

3.1   Introduction

Recent studies have begun applying PAT to the identification of PCa in human prostates [163,171,182,186]. Unfortunately, a method of identifying targets for the prostate biopsy has yet to be achieved without manual selection of ROI that rely on intensity-based thresholding [171,182] or the use of multispectral PAT analysis [163,182,186] that would decrease the frame rate. Out of these studies, Rajanna *et al.* used deep neural networks to learn features and then identify pixels representing PCa. This work was completed using a previously published PAT dataset of *ex vivo* human prostates that were sliced into axial sections prior to five wavelength PAT imaging [182]. The imaging method ensures uniform light fluence over the anterior-posterior axis of the tissue, which is currently not possible for prostate PAT in the clinical setting [171]. Additionally, the feature learning method used is based on feature learning of gene expression profiles, which can have hundreds of features [229]. Here, we minimize the PAT channels to 1064 and 1197 nm and acquire the standard US channel. The rationale for this was discussed previously in section 2.1. Since feature learning typically involves 10s to 100s of features [186,229], we utilize the "off-the-shelf" K-means clustering feature learning of texture patches, which has been shown to be effective in single-layer networks [230], for the purpose of identifying targets for PCa biopsy.

3.2   Materials and methods

3.2.1   Prostate specimen inclusion and handling

All work performed followed the approved Institution Review Board protocol (IUSCC-0581). A total of 9 prostate specimens were imaged in a room near the Indiana University

Hospital surgical suite directly following radical prostatectomy (**Fig. 3.1**). After 10 sterile saline washes of the external surface, prostates were immobilized using an agar bed and imaged with PAT and US as described below. Formalin fixation and whole mount histopathological analysis was then performed by urogenital pathologist (L.C.) as previously described [231]. De-identified pathology reports were also provided in addition to the annotated whole mount histopathology slides.

3.2.2   PAT and US imaging

1064 nm and 1197 nm PAT imaging was performed using a setup (**Fig. 2.1**) with the previously published barium nitrite Raman laser [223] pumped with a 10 Hz Nd:YAG laser (Continuum, San Jose, CA). (**Fig. 2.4**) A bifurcated fiber bundle (Fiber Optic Systems, Inc., Simi Valley, CA) delivered the pulsed light at a 30° angle relative to the probe. A C9-5ICT TRUS probe (Philips, Andover, MA) was used to collect PAT signal and to perform US imaging with an US system (Verasonics, Kirkland, WA). The C9-5ICT TRUS probe was designed to include US imaging of the prostate from the rectal cavity, and thus allowed for imaging of the prostate's entire posterior-anterior depth. Experiments were performed at 55 mJ/pulse with a 0.5 mm step size while raster scanning. Scanning was performed in 10 minutes with no averaging applied per frame. Images were taken in the prostate's axial plane to match the histopathology slices' plane.

3.2.3   Image and histopathology slice matching

PAT and US images were matched to histopathology slides (n=40) by using the US channel alone. Since the PAT and US imaging were performed in the same plane as the histopathology slices, the prostate characteristics from the histopathology slides, which included anterior-posterior length, left-right length, urethral position and perimeter shape, along with a minimum spacing of 4 mm between each prostate's histopathology slides, were used to determine the best match between the histopathology slides and the US channel. The measurements were taken manually from the histopathology slides [145]. Measurements of US channel frames were taken using ImageJ [232]. As scanning was performed in 0.5 mm increments, the distance between US channels was known to ensure at least 4 mm spacing between frames matched to consecutive histopathology slices.

3.2.4 Intensity-based analysis of PAT images

ImageJ was used to assess the minimum, average, and maximum signal intensities for PCa and laterally-matched benign ROIs [232]. The averaged maximum benign ROI signal intensity was used as the minimum threshold for PCa-specific signal to determine if intensity thresholding can be applied to determine targets for the prostate biopsy.

3.2.5 Training and testing datasets

The training dataset consisted of six prostate specimens comprising of 28 total whole mount histopathology slices, while the testing dataset had three prostate specimens of 12 histopathology slices. **Table 3.1** shows the specimens' clinical and pathological distribution. The two datasets were randomly divided, except for the Gleason 6 case that was specifically added to the training dataset as there was only one case with this Gleason score.

3.2.6 Statistical Analysis

A minimum of three repetitions were used for all experiments. Values are represented as averages with standard deviation of sample for the error. One-way ANOVA was used for hypothesis testing with Tukey's HSD post hoc test. The significance level (p) is < 0.05.

3.3 Results

3.3.1 Thresholding-based analysis is ineffective for identifying PCa biopsy targets

Intensity thresholding for identifying PCa targets was initially applied due to recent *in vivo* PAT imaging study of prostate angiogenesis which utilized an intensity-based analysis [171]. For assessing intensity thresholding for identifying PCa-associated signal, we determined the minimum, average, and maximum signal intensities for PCa and depth-matched benign PAT ROIs (**Fig. 3.2a**). To include only PCa-specific signal after thresholding, the average maximum signal intensities for the 1064 nm and 1197 nm benign ROIs were used as the minimum cutoff for PCa-specific pixel identification. For 1064 nm PAT images, the threshold was set at 9.9 (log scale), while 8.8 was the threshold for 1197 nm PAT images. This approach results in no signal for identifying prostate biopsy targets in the PCa tissue (**Fig. 3.2b,c**). This is expected as the PCa and depth-matched benign ROIs' minimum, average, and maximum values

are not statistically different (**Fig. 3.2a**). Based on these results, an alternative approach is needed for identifying targets for the prostate biopsy.

3.3.2 K-means clustering feature learning of PAT texture patches demonstrates that 1197 nm PAT does not uniquely contribute to clustering results

Besides intensity-based analysis, prior work involving PAT of human prostates for the purpose of distinguishing malignant versus benign tissue includes applying multispectral deconvolution, frequency analysis, and deep neural nets with Greedy feature selection to a dataset of axially-sectioned, ex vivo human prostates [163,182,186]. Unfortunately, multispectral deconvolution cannot be applied here as two PAT channels are not sufficient as there are at least three endogenous PA absorbers present, i.e. hemoglobin, lipid, and water [126]. Additionally, with two PAT and one US imaging channel, we are limited in machine learning approaches without reformatting the data [229,230]. To reformat the data for k-means clustering feature learning, the histopathology slice-matched PAT and US images (**Fig. 3.3a-c**) were initially converted from an image format to a format appropriate for k-means clustering (**Fig. 3.3d,e**). Texture patches were converted to row-wise data with neighborhood features in each column. The patches were five-by-five and considered column-wise from left to right. The step size between each patch was one. The patch size and step was chosen from prior published work [230]. Following reformatting the training dataset was dimensionally reduced using principal component analysis for the PAT channels alone. The top 50% of the major principal components were included for feature learning.

After reformatting and dimensionally reducing the data, the feature learning was performed using k-means clustering with the open source library VLFeat (0.9.20) [233] with k = 100. Since strong correlation between 1064 nm and 1197 nm PAT of hemoglobin and lipid was present (**Fig. 2.4f**), feature learning was performed on 1064 nm PAT with US and 1197 nm PAT with US (**Fig. 3.4**) to determine the clustering contribution from each PAT channel. The PCa-related features were manually chosen in the training dataset based on overlap with the PCa ROI in the ground truth histopathology slices. Next, the learned feature cluster centers were used to cluster the reformatted and dimensionally-reduced data in the testing dataset. The testing dataset was matched to the closest learned cluster center. The testing data that was clustered into the PCa-related feature clusters was then assessed for the clustering contribution.

As shown in **Figure 3.4**, the original 1064 nm and 1197 nm PAT images are strongly correlated. For the testing cluster outputs, the PCa-related clusters are also similar except that there is more non-specific PCa cluster signal in the 1197 nm with US channel results, which could be due to the signal intensity being approximately an order of magnitude lower for the 1197 nm PAT versus the 1064 nm PAT (**Fig. 3.4, Col. 2-3**). Therefore, the 1197 nm PAT channel does not provide a unique contribution to identifying PCa biopsy targets, and only the 1064 nm PAT with US channel should be used for training and testing of prostate biopsy targets.

3.3.3   1064 nm PAT and US texture analysis identifies biopsies targets

Since the learned features are not dependent upon the 1197 nm PAT channel, analysis was completed using the 1064 nm PAT and US channels. The cluster centers from the training dataset (n = 28) were used with the testing dataset (n = 12). As angiogenesis is not a specific biomarker [76], the PCa-associated clusters were not specific to PCa nor only prostatic tissue (**Fig. 3.4**). To overcome non-specific results, we apply a ten-by-ten density filter to the PCa cluster results. The ten-by-ten density filter is assignment of 0 to 100 to each pixel based on the number of pixels assigned to a PCa-related cluster in the nearby 10-by-10 pixels. Then, non-specific results were removed by thresholding the density level (**Fig. 3.3g**). Finally, the center of mass for groupings of prostatic signal was calculated to determine where the biopsy core would be targeted (**Fig. 3.5**).

Using center of mass on the density filter of the PCa cluster outputs, targets were successfully identified for 100% (3/3 prostates) of the primary PCa tumors in the testing dataset. In addition, 67% (2/3 prostates) of the secondary PCa tumors were targeted by this approach. A PCa-free histopathology slice was present in the testing dataset (**Fig. 3.5**). A small amount of PCa-associated cluster output was present in this PCa-free image. The signal was located in the bilateral peripheral posterior of the prostate. Since signal was present, biopsy targets were still included. Ultimately, the number of targets from our approach is ten, eight, and ten targets respectively for patient 1, 2, and 3 in the testing dataset. For these targets, the percentage of false positive cores was 40% (4/10), 50% (4/8), and 30% (3/10) cores for the three cases. Thus, we are able to target multiple locations of each PCa tumor in the cases with at least two fewer cores than the current clinical gold standard approach of the systematic 12-core TRUS-guided biopsy [15,234].

3.4   Discussion

Our work presented here shows that k-means clustering feature learning of 1064 nm PAT and US texture patches can be used to identify targets for PCa biopsy. For the first time, PAT is utilized along with supervised machine learning to independently identify targets for prostate biopsy in intact human specimens. Previously, significant work was performed on an axially-sliced human prostate specimen PAT dataset looking at multispectral deconvolution, frequency analysis, and deep neural nets with Greedy feature selection [163,182,186]. While this work shows the differences between PCa and benign prostate tissue, the studies' approaches are still based on user-selected ROIs or do not show the locations where targets would be suggested compared to ground truth histopathology slides. Additionally, the experimental design with sectioned prostate and subsequent transverse plane of imaging does not adequately challenge PAT and analysis methods on imaging depth that would be required for clinical translation. Most recently, an *in vivo* pilot study of three patients showed correlation of PAT of blood to vascular changes in prostate tissue with known PCa [171]. This work relied on intensity-only measurements which are limited over the depth of the prostate (**Fig. 3.2**). Thus, our work presented here provides an important contribution to the field of PAT of prostates for the purpose of guiding PCa biopsy.

The analysis approach presented here has some inherent advantages as only a single PAT and the US channels were utilized. For PAT, pulsed lasers are necessary to stimulate the resulting acoustic signal [134]. These lasers are typically 10-20 Hz, with our system containing a 10 Hz laser. If multiple wavelengths or averaging was needed, the frame rate would then decrease and add more time to the procedure. The advantage of using multispectral PAT imaging is that deconvolution of the signal into its endogenous contrast components could be performed. Whereas, the benefit of averaging multiple frames at one imaging location is that the pSNR could be improved, which would improve the image quality for analysis. As the prostate biopsy is performed on awake patients and the urologist is manually controlling the US transducer while the patient can simultaneously move [235], issues with individual channels overlapping at an imaging location are possible. This alignment of individual channels is important for analysis purposes. Our image analysis approach avoids the potential issue of channel overlap in each frame as only a single PAT wavelength was ultimately used to determine the prostate biopsy targets. The use of one PAT wavelength maximizes imaging speed and will

limit added time for the procedure if clinically translated. Additionally, for the first time, we identify prostate biopsy targets with an imaging and light delivery scheme that is clinically relevant compared to previously published work [163,182,186].

For this preliminary study, inherent limitations are present. E*x vivo* intact fresh prostate specimens were imaged directly after radical prostatectomy and before formalin fixation. The 1064 nm PAT images' signal is primarily from the endogenous absorber hemoglobin. The absorption coefficient of hemoglobin is different for oxy- versus deoxyhemoglobin [126]. As the prostate no longer has normal perfusion, we expect the feature learning of *in vivo* prostate 1064 nm PAT to provide different cluster centers than in the presented work. Additionally, an anatomical barrier that is not included in this study is the rectal wall, which is a highly scattering tissue [197]. Thus to ultimately prove the utility of this approach, *in vivo* imaging is necessary to see the analysis method's performance with normal anatomy and perfusion.

Another limitation in this study is the use of histopathology slices as ground truth for the biopsy targets. Differences in the thickness of the histopathology slides and the PAT/US image frames exist—histopathology slices are typically only a few microns thick, while the elevation resolution for TRUS transducers cannot achieve this thickness [236]. Also, our approach to matching was performed based on manual measurements [145]. Thus, exact matching for all of the histopathology slice to the appropriate PAT/US image frame is difficult to achieve.

A final consideration for this work is the light delivery and US transducer designs [134]. Here we utilize a bifurcated fiber bundle array at a 60 degree angle mounted to the US transducer. This design allows for the least amount of distance from the fiber bundle to the prostate tissue to limit light divergence and water absorption. However, a pitfall exists with this setup: an inherent focus of the light at approximately 1 cm from the fiber bundle and US transducer array (**Fig. 2.4a**). For this reason, we believe that the secondary lesion that was not targeted in these results was due to the tumor's close proximity to the fiber bundle and US transducer. This issue could be overcome if an additional imaging scan was performed with the fiber bundle and TRUS probe farther from the tissue so that the most posterior tissue would be in the beams' focus. If this imaging modality and analysis were used clinically, the urologist could adjust the probe position in real-time to visualize the location.

3.5   Conclusions

1064 nm PAT and US texture-based k-means clustering feature learning successfully provided tumor cluster centers that were validated in the testing group. The resulting targets delivered a 100% (3/3) and 67% (2/3) sensitivity respectively to primary and secondary lesions while maintaining a total number of biopsy targets per prostate that is lower compared to the number of core biopsies acquired during current prostate biopsy protocols. Therefore, this real-time multimodal imaging technique with target identification method should be explored further *in vivo* to determine its clinical value for improving the sensitivity of prostate biopsies for the purpose of PCa diagnosis.
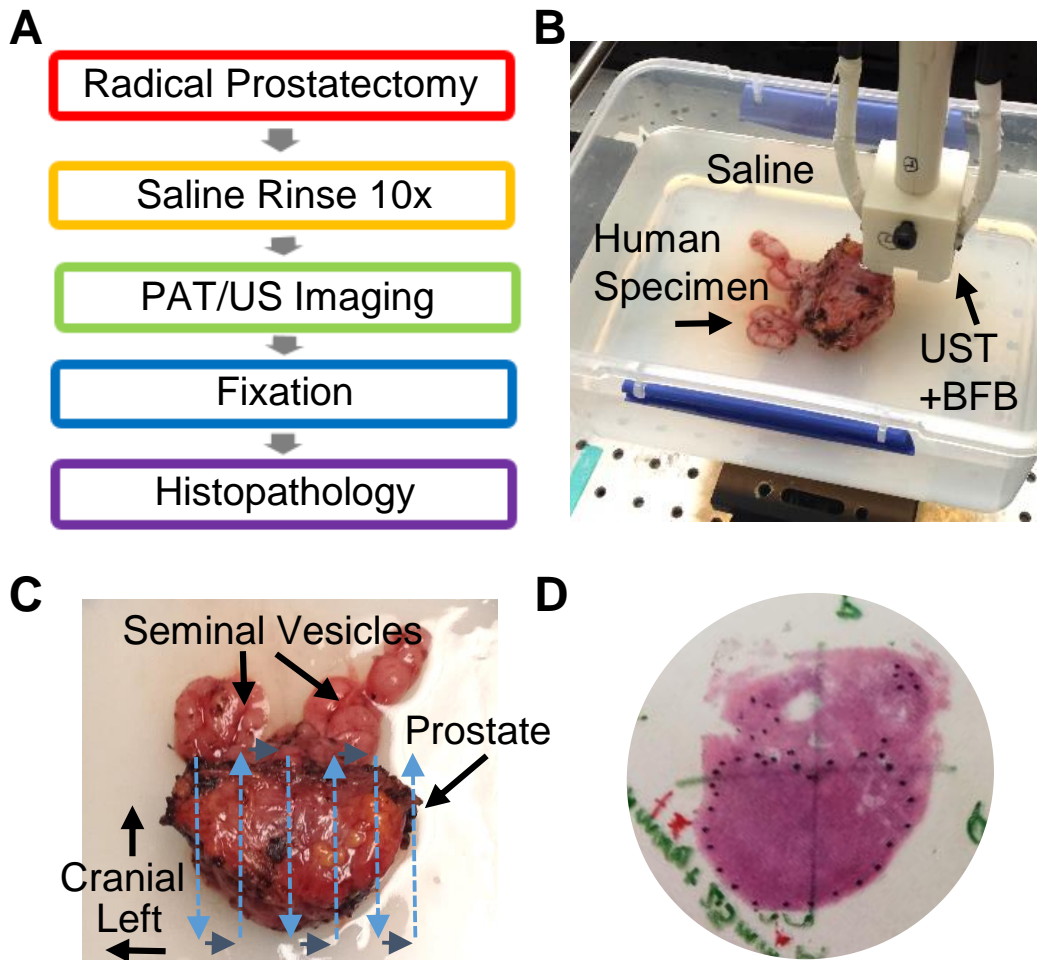
Figure 3.1. Prostate specimen handling during data collection. (a) Prostate specimen handling procedure from radical prostatectomy to whole mount histopathology. (b) Image of prostate specimen during PAT and US imaging. UST + BFB: ultrasound transducer with bifurcated fiber bundle. (c) Image of prostate specimen depicting position during imaging and the raster scanning pathway. (d) Representative whole mount histopathology slide. An experienced urogenital pathologist marked the tumor margins and completed the corresponding histopathology report. These slides are considered ground truth for image analysis.

Table 3.1. Patient characteristics of training and testing datasets

Training Dataset (prostates=6)	
Age	61 +/- 9
Prostate Volume (cm^2)	82.3 +/- 26.0
Primary Lesion Largest Dimension (cm)	2.79+/- 1.1
Secondary Lesion Largest Dimension (cm)	1.0 +/- 0.4
Gleason 6	1
Gleason 7a	3
Gleason 7b	2
Gleason 8-10	0
Testing Dataset (prostates=3)	
Age	72 +/- 7
Prostate Volume (cm^2)	96.4 +/- 23.3
Primary Lesion Largest Dimension (cm)	1.9 +/- 1.0
Secondary Lesion Largest Dimension (cm)	1.2 +/- 0.6
Gleason 6	0
Gleason 7a	2
Gleason 7b	1
Gleason 8-10	0
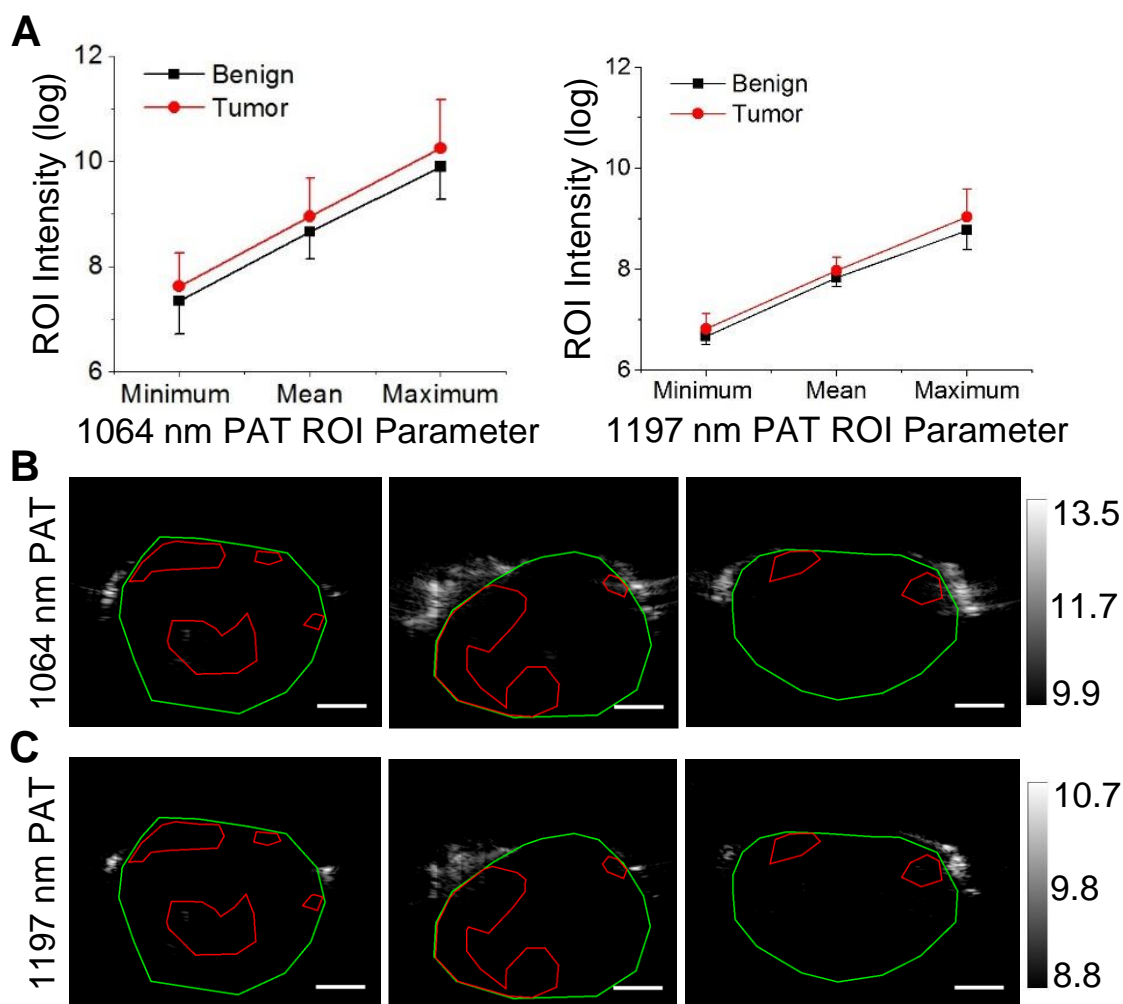
Figure 3.2. Thresholding-based analysis is ineffective for identifying PCa biopsy targets. (a) Signal intensity characteristics for tumor and matched benign ROI. Tumor and benign ROI were not statistically different. Each data point consists of at least n = 12. (b) 1064 nm and (c) 1197 nm representative PAT images that have been thresholded with the maximum average benign ROI measurement. Prostatic (green) and tumor tissue (red) are outlined. No biopsy targets were identified with this method of analysis. Applies to all panels: scale bar = 1 cm.
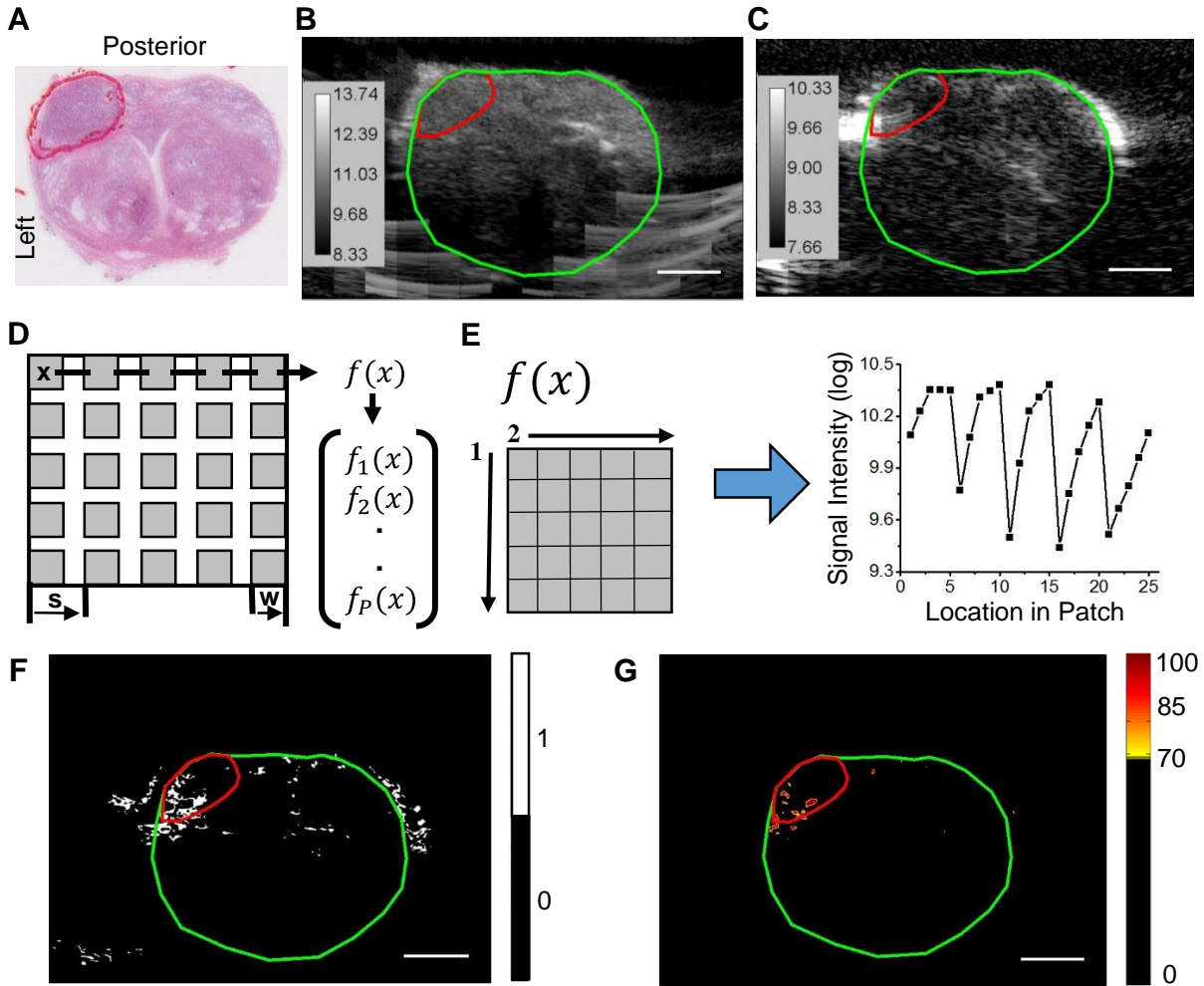
Figure 3.3. Texture-based K-means clustering feature learning. (a) Example whole mount histopathology slide with demarcated tumor margins (red line). (b) US and (c) 1064 nm PAT images that best match the whole mount histopathology slide in A are shown. (d) Texture patch (x) generation involves determining optimum patch size (w) and step size between patches (s). Patches are sequentially created from left to right and then top to bottom of the US and PAT images. (e) The patches are processed to a format that is appropriate for k-means clustering. (f) Raw PCa-related cluster output from k-means clustering feature learning of training set for US and PAT images in B and C. (g) Raw PCa-related cluster output converted to density heat map with thresholding. Signal corresponds to left posterior tumor foci in A. Applies to all panels: scale bar = 1 cm; Prostate margin: green line; Posterior tumor foci: red line.
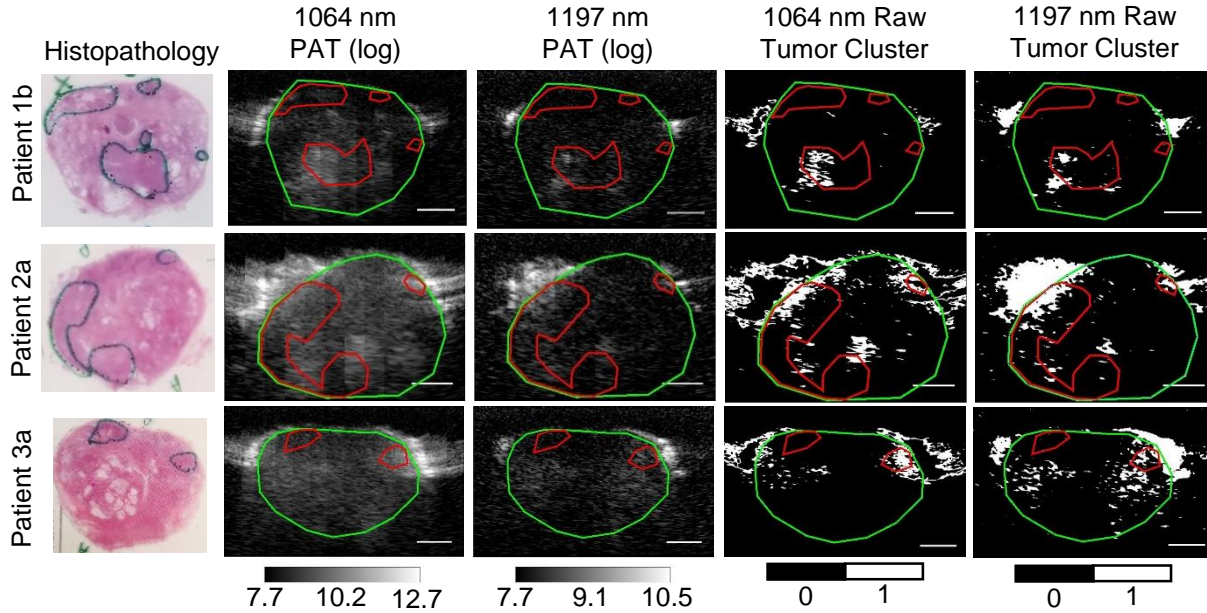
Figure 3.4. 1197 nm PAT does not uniquely contribute to clustering results. Each PAT channel was tested for its contribution to PCa feature learning by viewing the results of the testing dataset. Whole mount histopathology slides with the major tumor's largest dimension from each case in the testing dataset are shown in the left-most column. The PCa tumor margins are outlined (green) on the histopathology slides by a urogenital pathologist. 1064 nm and 1197 nm PAT images in log scale corresponding to the histopathology slides are displayed in the second and third column with the prostate (green) and tumor margin (red) outlines matching the histopathology slides. The raw testing results are exhibited in the two right-most columns with the same prostate tissue (red) and tumor (red) outlines for reference. Applies to all panels: scale bar = 1 cm.
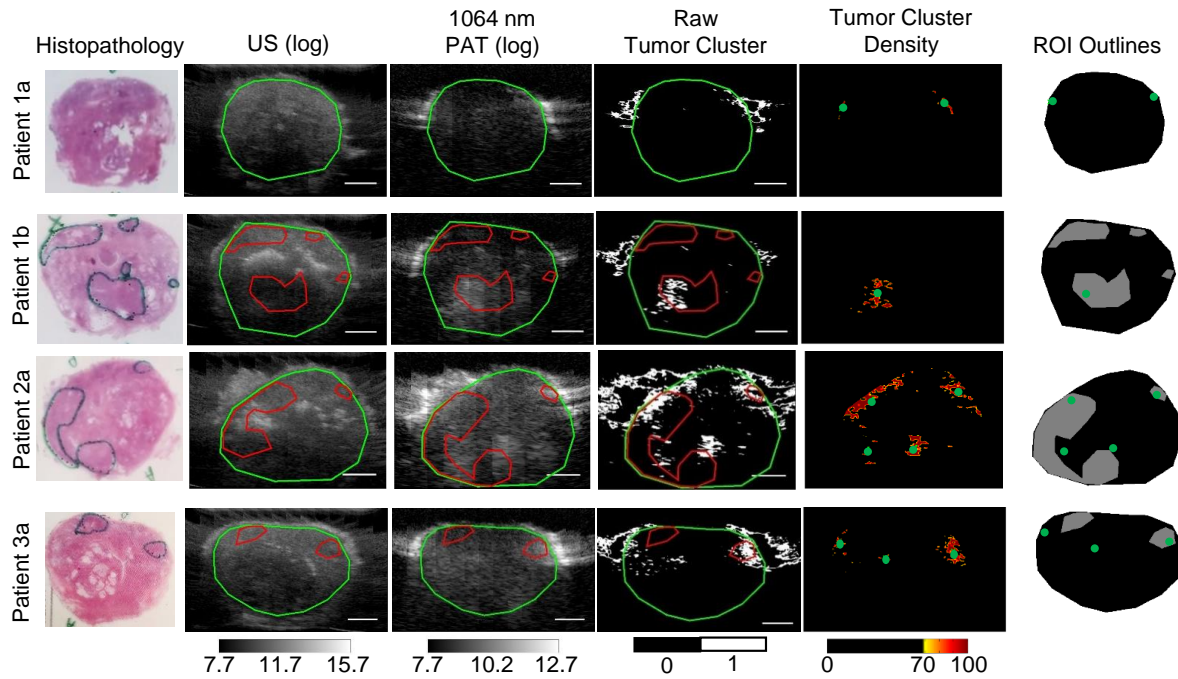
Figure 3.5. Prostate biopsy targets identified in testing dataset. The PCa tumor margins are outlined (green) on the whole mount histopathology slides in the left-most column. A cancer-free slide was present in patient 1 of the testing dataset. US and 1064 nm PAT images in log scale corresponding to the histopathology slides are displayed in the second and third column with the prostate (green) and tumor margin (red) outlines matching the histopathology slides. The raw testing results are exhibited in the fourth column with the same prostate tissue (red) and tumor (red) outlines for reference. The raw data is then shown as a density heat map in the fifth column. Center of mass (green circle) of the density signal marks the targets for hypothetical prostate biopsy core acquisition. In the right-most column, the location of these targets is displayed on the histopathology slides' ROI: prostatic tissue (black), PCa (grey), and background (extraprostatic tissue and saline; white). Applies to all panels: scale bar = 1 cm.

4. PRELIMINARY TRANSURETHRAL LIGHT DELIVERY DEVICE DESIGNS AND TESTING

*A portion of the contents of this chapter and all of the next chapter (Ch. 5) were published in *Biomedical Optics Express* [237], and were reformatted for dissertation. Additional data has been added to this chapter that were outside of the scope of the submission to *Biomedical Optics Express*.

4.1   Introduction

PCa is the most incident cancer in men with an estimated 164,690 new cases to be diagnosed in 2018 [210]. To confirm the presence of PCa after prostate specific antigen screening, initial tissue biopsies are now acquired using the MRI fusion-guided prostate biopsy protocol. For this approach annotated MRI images are overlaid on real-time US imaging to guide sampling of suspicious regions marked by uroradiologists, and additional biopsy samples are acquired via the previous templated biopsy protocol [1–5]. While this approach improves the sensitivity of the prostate biopsy, a real-time imaging method of identifying suspicious regions to biopsy could help overcome some of the pitfalls of the MRI fusion- guided prostate biopsy [28–30].

PAT, a hybrid optical imaging technique, has great clinical translatability due to its increased imaging depth compared to pure optical imaging modalities. The PA signal is generated by photon absorption in biological tissue, which is subsequently released as heat. The resulting localized thermoelastic expansion generates an acoustic wave, which can then be detected by traditional clinical US transducer arrays [134,238–241]. In recent years, PAT has been applied to many clinical topics, such as neurological system [138–141], breast cancer [145–149], female reproductive tract [142–144], gastrointestinal system [150,151], atherosclerosis [157–161], PCa [162–171], urological system [172–178], melanoma [152–156], and fibrosis [136,137].

PAT can provide real-time imaging for the PCa biopsy since the same US transducers used for the current biopsy protocol can be used to collect the PAT signal. The combination of PAT and US imaging can then provide spectroscopic and anatomical information [162–

168,170,171]. Angiogenesis and lipid accumulation have been shown to be increased in PCa tumors [76,191]. *In vivo* [171] and *ex vivo* [162,163,169] imaging of human prostates have shown differences between malignant and benign prostate tissue using endogenous contrast. We have recently shown that successful PCa biopsy targeting in *ex vivo* human prostates is possible using hemoglobin PAT at 1064 nm and US imaging [162].

While PAT has the potential to provide biopsy targets to under-sampled regions of the prostate, current PAT setups have not yet demonstrated the ability to image the full posterior-anterior depth as observed from the rectum with the US transducer [162,163,169–171]. Two locations for the placement of the light delivery source for PAT have been investigated. The first location is placing the light delivery mechanism with the US transducer in the rectum. Simulation studies [188] along with *in vivo* [170,171] and *ex vivo* [162] PAT of human prostates have shown that the anterior regions of the prostate do not receive adequate light fluence to detect malignant and benign signal contrast when a rectally-located illumination source is used. The second location, which shows improved potential for PAT of the anterior prostate [188], is to deliver light via the prostatic urethra. A couple of transurethral light delivery designs have been employed for transrectal prostate PAT imaging, including a bevel-tipped fiber [190] and a fiber with a diffuser end [165]. While the recently published transurethral illumination device with diffuser end improved the illumination volume [165], neither of these transurethral light delivery designs has demonstrated the ability to deliver sufficient light for whole axial PAT of the prostate without rotating the illumination source, which can cause pain for the patient. To fill this gap, we investigate two transurethral illumination designs that provide 360° of radial illumination for the purpose of illuminating the whole axial plane of the prostate. The first is a fiber bundle of side firing, bevel-tipped fibers, and the second is a cone-tipped fiber design. Using 1064 nm we test the performance of these transurethral illumination sources to determine the ability of designs to fill the gap in transurethral illumination for prostate PAT.

4.2 Methods

4.2.1 Bevel- and cone-tipped fiber and fiber bundle fabrication

To fabricate the bevel-tipped fibers, 1.0 mm core MMF (FP1000ERT, Thorlabs, Newton, NJ, USA) were cleaved and polished using a NanoPol Polisher (Ultra Tec

Manufacturing, Inc., Santa Ana, CA, USA) with 30 µm to 0.02 µm grit diamond lapping sheets (Thorlabs, Newton, NJ, USA). The jacket and cladding were removed from the fiber's ends with a razor blade. For the coupling end, the fiber was polished flat with the NanoPol Polishers set to 0° polishing angle. The emission end of the fibers were polished with angles from 42° to 46° in 1°. The bevel-tipped fibers were capped with glass capillary tubes and were arranged in a 6 + 1 pattern for the fiber bundle. The fibers were aligned so that the light fired perpendicular to the fiber bundle and held in place with epoxy. The cone-tipped fiber was provided by a collaborator and was fabricated with 0.4 mm core MMF. It was similarly capped with a glass capillary tube to protect the fiber's cone tip.

4.2.2   Measurement of fiber emission

For the bevel-tipped fibers and fiber bundle, the light energy emission was measured using a power sensor and corresponding power meter (Coherent, Santa Clara, CA, USA). The energy firing forward and to the side was determined. After the fiber bundle was assembled, the output was tested for each fiber to determine the output uniformity around the fiber bundle.

4.2.3   1064 nm PAT and US imaging performance testing

The bevel-tipped fiber bundle transurethral illumination device was tested by imaging *ex vivo* human prostates directly after radical prostatectomy with 1064 nm PAT and US. The US system and 1064 nm laser (**Section 3.2.2**) along with tissue handling protocol (**Fig. 3.1**) was the same as previously published [226]. The illumination device used was the bevel-tipped fiber bundle. Light was coupled into the fiber bundle by using a 25 mm focal length plano-convex lens. The laser was set to output 100 mJ/pulse, and the output from the fiber bundle was tested directly before prostate imaging. The illumination device was inserted into the prostatic urethra and held in place while the C9-5ICT transrectal US (TRUS) probe (Philips, Andover, MA), which did not have any illumination device mounted, scanned the prostate specimen.

To test the imaging performance of the cone-tipped fiber, a phantom was used with pencil leads embedded in 1% agarose gel (CN: 16500500, Invitrogen, Carlsbad, CA, USA). The cone-tipped fiber was centered between the pencil leads. 1064 nm PAT and US imaging was performed in scanning mode to find the peak PA signal location along the phantoms length. Frame images of 1064 nm PAT and US was taken every one mm for seven mm with the images

centered at the location of peak PA signal. 10 frames were averaged per image. A minimum of three images were taken per location. The images were analyzed using ImageJ [232].

4.3 Results

4.3.1 Side-firing conversion efficiency of bevel-tipped MMFs

The forward- and side-propagating fractions of the total coupled energy were measured to determine the critical angle for the total internal reflection required to convert the forward-propagating light to side-firing. The theoretical critical angle for the fiber to achieve total internal reflection is 44.5°. This is near the approximate angle (44°) that was simulated (not presented here) by a colleague to achieve a 90° emission angle relative to the long axis of the fiber. Fibers with beveled tips from 42° to 46° were tested (**Fig. 4.1**). The angle that initially achieved a greater than 90% side-firing conversion efficiency was 44°. Fibers with 45° and 46° beveled tips similarly had 95% or better side-firing conversion efficiencies. For the 43° and 42° bevel-tipped fibers, the conversion efficiency dropped off steeply as the efficiencies were 78% and 55% respectively. Based on this data, 44° was chosen for the bevel tip angle for the individual fibers that will comprise the transurethral fiber bundle.

4.3.2 Transurethral side-firing fiber bundle characterization

The side-firing transurethral fiber bundle was created as a 6 + 1 design (**Fig. 4.2a**). The six side-firing fibers were epoxied to the central spacer fiber, which had no energy coupled into it. The diameter of the fiber bundle was approximately 6 mm (**Fig. 4.2b**). The illumination profile is shown using visible light in **Fig. 4.2c,d**. The light is emitted at 90° relative to the long axis of the fiber. The radial emission from the six fiber is evenly distributed, but inherent peaks are present.

The side-firing transurethral fiber bundle was installed on the optical table and aligned for maximum coupling possible coupling efficiency. The estimated surface area of the energy at the glass-tissue interface is 0.02 cm^2. Since the damage threshold for the laser used is 100mJ/cm^2/pulse [228], no more than 2 mJ/pulse should be output from each fiber to avoid tissue damage. The laser output was tuned until the energy output from each fiber was approximately 1 mJ/pulse. Each fiber's energy output was measured to determine the radial emission uniformity. The output ranged from 0.8 to 1.1 mJ/pulse/fiber (**Fig. 4.3a**). Since the fiber

bundle has a peak in the radial emission every 60°, the fiber bundle was rotated 30°. The energy emission from each fiber was measured again. The output ranged from 0.8 to 1.15 mJ/pulse/fiber (**Fig. 4.3b**).

4.3.3   1064 nm PAT and US imaging of phantom with cone-tipped fiber

To improve the radial illumination uniformity while decreasing the outer diameter of the side-firing transurethral illumination device, a cone-tipped fiber was fabricated. This reduces the outer diameter of the device by at least three times if the same one mm diameter core fiber was used. The cone-tipped fiber tested here was made using 0.4 mm diameter core fiber with a glass capillary tube used to protect the tip (**Fig. 4.5a**). A simple imaging phantom was made using pencil lead embedded in agarose gel (**Fig. 4.5b**). The pencil leads were placed evenly in a circle. The cone-tipped fiber was then inserted in the middle of the circle of pencil leads. 1064 nm PAT and US imaging was performed similarly as for the fiber bundle. The cone-tipped fiber was held in place while the TRUS probe was translated during imaging. The peak 1064 nm PA signal was measured for each pencil lead and the cone-tipped fiber location (**Fig. 4.5c)** in the PAT channel. Plotting the peak 1064 nm PA signal intensities along the fiber axis shows that the 1064 nm PA signal from the pencil lead is detectable 1 mm in front of and behind the peak PA signal location (**Fig. 4.5d**). In addition, the signal is not uniform radially in each frame.

4.3.4   1064 nm PAT and US imaging of human prostates with transurethral fiber bundle

Following testing of the side-firing transurethral fiber bundle emission, the device was tested by imaging an *ex vivo* human prostate directly following radical prostatectomy. 1064 nm and US imaging was performed by placing the side-firing transurethral fiber bundle in the prostatic urethra. The fiber bundle did not move during imaging while the TRUS probe raster scanned the tissue. The imaging frame with the highest PA signal is shown in **Fig. 4.4**. The whole prostate can be seen in the US channel. The urethra is shown with the yellow circle. The PA signal in the 1064 nm PAT channel is not detectable to the exterior regions of the axial prostate. Peaks can be observed that correspond to the radial emission peaks from the individual fibers.

4.4   Discussion and conclusions

Two side-firing transurethral illumination device designs were explored in this study to achieve whole axial prostate illumination. The fiber bundle design comprised of bevel-tipped fibers provided 360° radial illumination, which has yet to be reported [165,190]. Unfortunately, the radial profile of the side-firing fiber bundle presented here had a non-uniform illumination profile with peaks corresponding to the fiber locations. This is non-ideal as the fluence rate is directly related to the PA signal intensity [126,129]. Therefore, the ideal radial illumination profile is uniform to reduce the changes in PA signal intensity due to inherent properties of the transurethral illumination device.

Other pitfalls of the side-firing transurethral fiber bundle design is that the location of the bevel-tipped fibers is close to the glass-tissue interface. Due to this the effective illumination surface area was calculated to be 0.02 cm^2. The illumination area, along with the laser specifications, limits the maximum permissible energy that can be emitted from each fiber before tissue damage occurs [228]. Additionally, the overall diameter of the side-firing transurethral fiber bundle is approximately 6 mm and close to the maximum that can be used clinically [242].

The second side-firing transurethral illumination device explored here has an improved uniform radial emission profile while reducing the device from seven fibers to one fiber. This can reduce the diameter of the device by three times. While the radial illumination profile was improved with this more compact design, the device has a pitfall of a limited longitudinal emission profile. As shown in **Fig. 4.5**, 1064 nm PA signal has a peak at the cone tip of the fiber and abruptly reduces before and after the cone tip. This reduces the translatability in the case of prostate PAT as the TRUS probe is manually controlled by the surgeon and may or may not be in the axial plane at all times. Thus, transurethral illumination device with a significant longitudinal emission profile is needed in addition to having the uniform radial profile. The recent work by Ai *et al.* has shown that a fiber with a 3 cm long cylindrically-diffusing end can be made and used for deep PAT. This was achieved by using a mirror to direct the energy to one side [165]. This work demonstrates that whole prostate illumination may be possible with further engineering improvements, which is the focus of chapter 5.
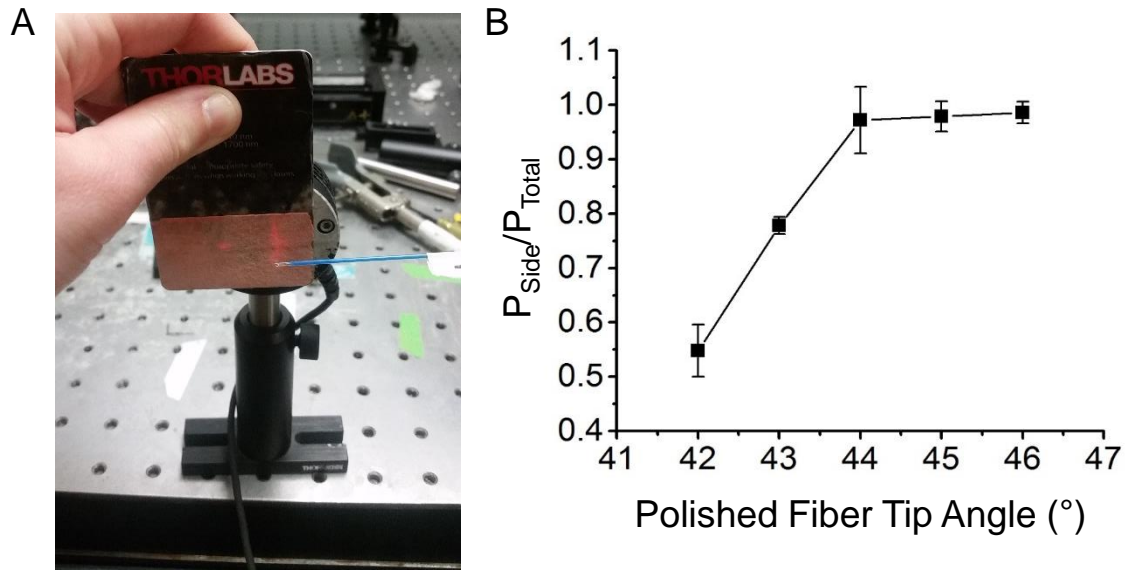
Figure 4.1. Side-firing conversion efficiency of bevel-tipped MMFs. (A) Picture of illumination profile from side- and forward-fired light. (B) Side conversion efficiency with increasing tip polishing angle.
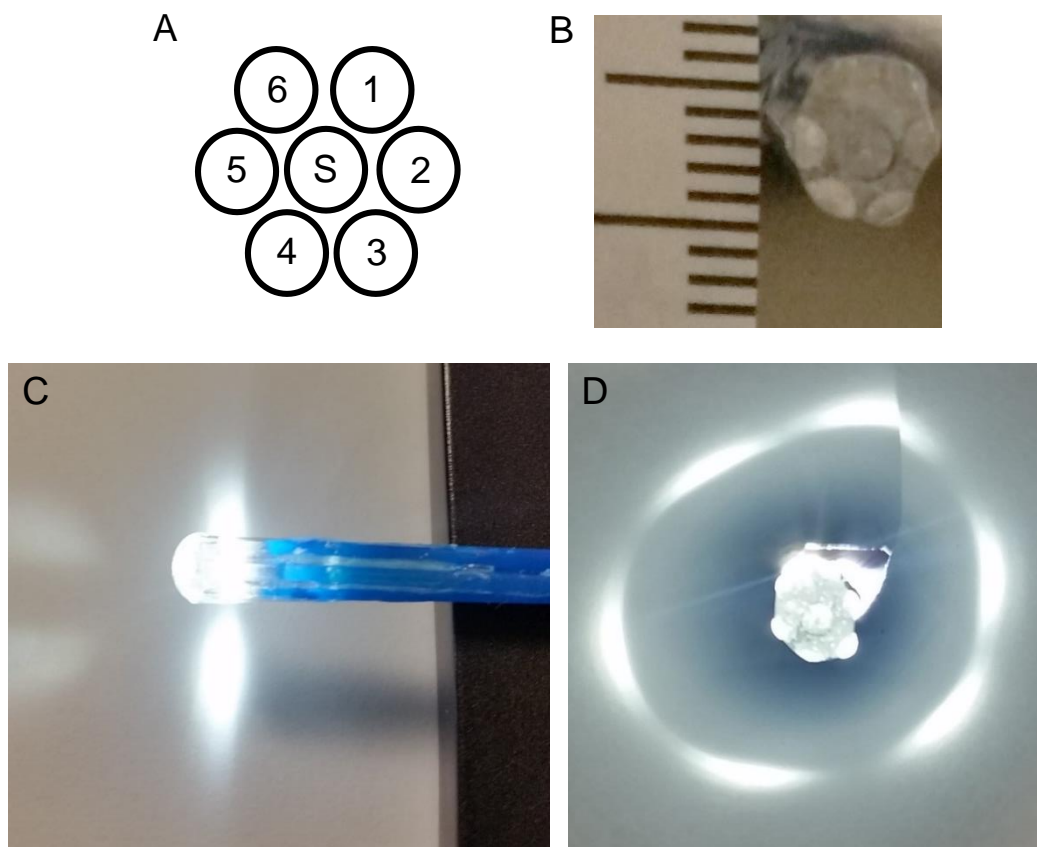
Figure 4.2. Fiber bundle design and illumination profile with bevel-tipped MMFs. (A) Schematic of the front view of the fiber bundle. Fibers 1-6 have bevel tips while the fiber labeled with "S" is a spacer. (B) Picture of fiber bundle from the front with ruler. The spacing is one mm between each line. (C) Side and (D) front view of the fiber bundle's illumination profile with white light.

74
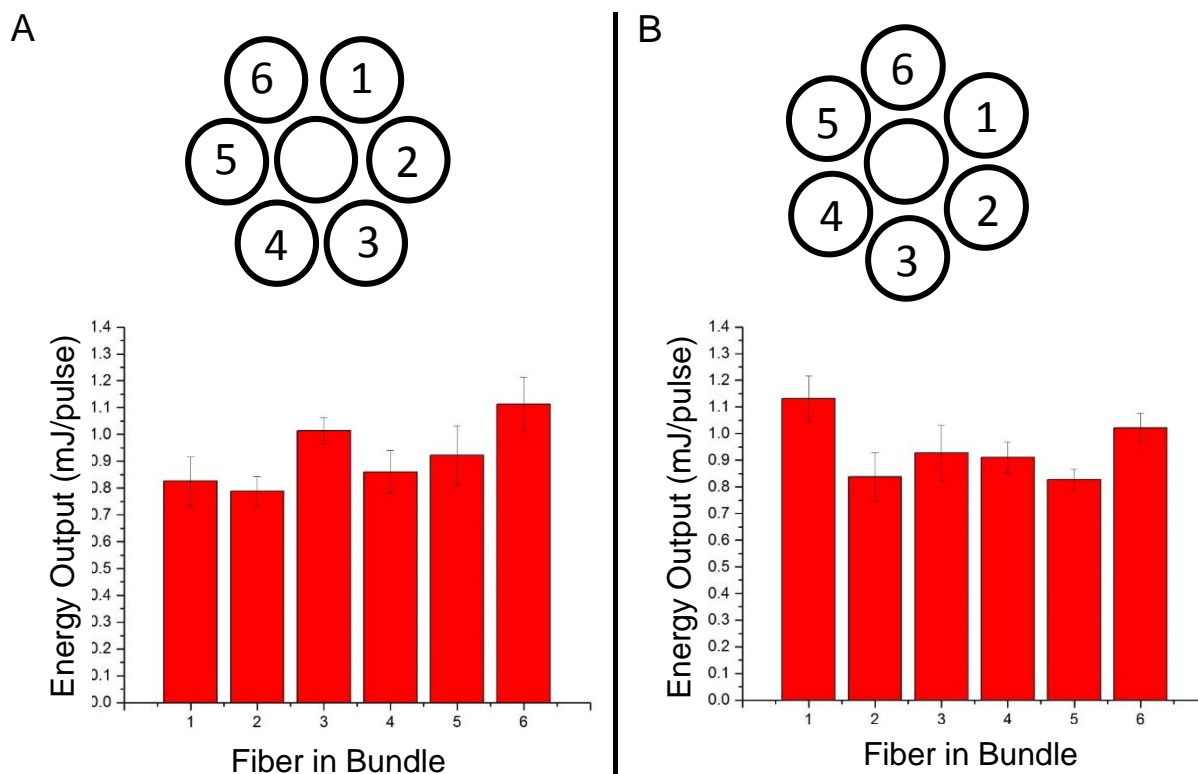
Figure 4.3. Relative fiber energy output before and after rotation. (A) Side-fired energy output per pulse from each fiber in the fiber bundle numbered 1-6, which matches the schematic. (B) Side-fired energy per pulse from each fiber after the fiber bundle rotated 30° clockwise. The fiber bundle schematic reference is similarly rotated 30° clockwise compared to the schematic in A.
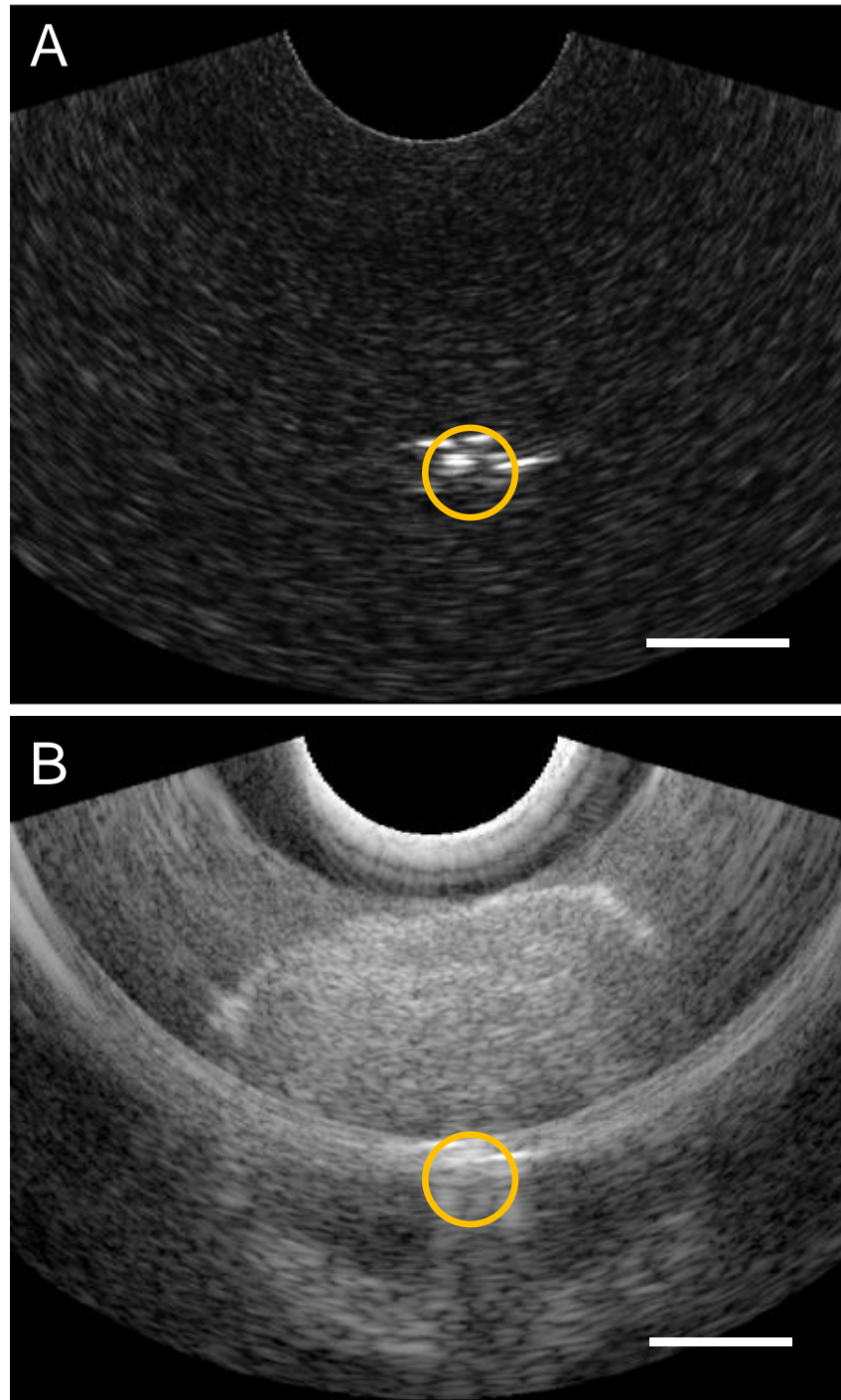
Figure 4.4. 1064 nm PAT and US imaging of human prostates with transurethral fiber bundle. (A) 1064 nm PAT and (B) matching US image of human prostate following radical prostatectomy. Side-firing fiber bundle is placed in the prostatic urethra (yellow circle). Scale bar: 1 cm.
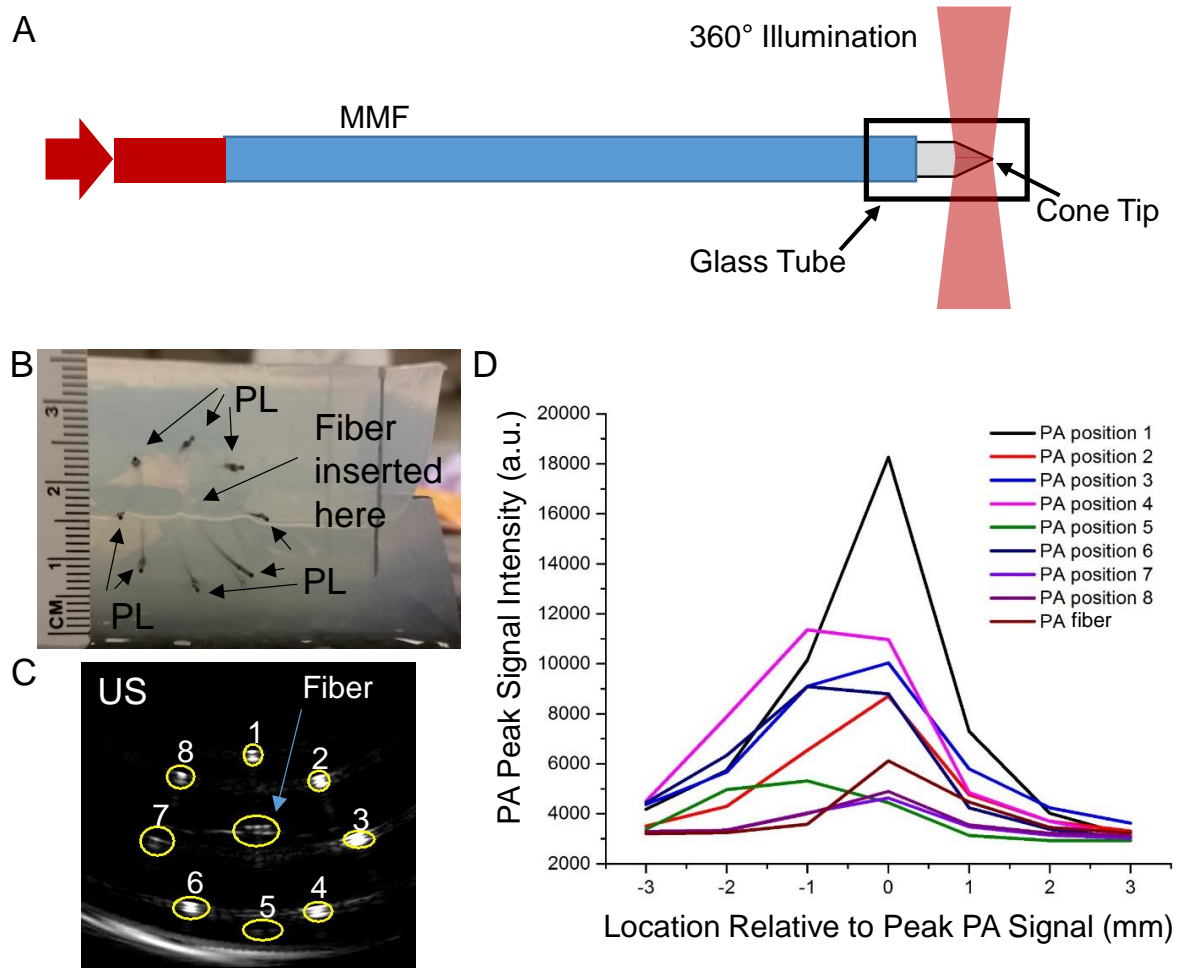
Figure 4.5. Cone-tipped MMF design and 1064 nm PA signal from phantom. (A) Schematic of cone-tipped MMF. (B) Picture of phantom with pencil leads (PL) located radially around fiber insertion location. (C) US image at fiber's cone tip. Labels from 1-8 correspond to the (D) graphed data of the peak PA signal intensity from pencil leads long the longitudinal axis of the fiber.

5. CYLINDRICAL ILLUMINATION WITH ANGULAR COUPLING FOR WHOLE PROSTATE PHOTOACOUSTIC TOMOGRAPHY

*The contents of this chapter and a portion of the previous chapter (Ch. 4) were published in *Biomedical Optics Express* [237], and were reformatted for dissertation.

5.1 Introduction

To illuminate the entire prostate via the prostatic urethra, cylindrical illumination is needed compared to light delivery methods that have limited axial thickness, for example bevel-tipped fibers [190], due to the uncoupled nature of the US transducer array's acceptance plane, which is manually controlled by the urologist during the biopsy procedure [4], and the region from which the PA signal is generated. In addition, since the patient is awake for the prostate biopsy procedure, any rotation and/or pullback of the fiber-optic device may cause patient discomfort. For these reasons a light delivery source with a cylindrical diffuser is needed.

While cylindrical diffusers have been used for photodynamic therapy for decades [243,244], their application in PAT is just emerging [165,169,245]. The process of fabricating a cylindrical diffuser typically entails methods that use acid etching [165,245] or laser micro-machining with a uniform pattern created on the fiber surface [246]. Using the acid etching method, Ai *et al.* created a 3.0 cm long diffuser on the end of a 1.0 mm core MMF. A maximum coupling energy of 40 mJ/pulse was demonstrated with two-thirds of the energy converted from forward firing to side firing. To increase the energy fluence to enable deep PAT, a parabolic mirror was incorporated to achieve an estimated 10 mJ/cm^2 energy fluence at the tissue surface. The final diameter of the transurethral light delivery device was 25 French or 8.33 mm, which includes the 1.0 mm core MMF diffuser, parabolic mirror, and rigid cystoscope sheath. This design illuminates roughly one-fourth of the axial plane along the whole caudal-to-cranial axis of the prostate, which is an improvement over the bevel-tipped MMF [190]. Similarly, the laser micro-machining method used to create a diffusing fiber for treatment of urethral stricture demonstrated forward energy leakage from the end of the diffuser end, while the majority of the energy was converted to side firing [246]. Most recently, Li *et al.* demonstrated the ability to detect PA signal generated 1 cm from diffusing MMF end made with

acid etching. While the forward propagation to side firing energy conversion was not evaluated, this study shows that deep PAT imaging is possible using a cylindrically diffusing fiber end. Based on this prior literature, the efficient conversion of forward to side firing energy in cylindrically diffusing MMFs needs to be improved to enable illumination of the whole prostate for PAT.

A commonly used approach to couple photons into a fiber is through a collinear geometry. Instead, we found that deviating the coupling from the collinear geometry significantly improves the conversion of forward propagation to side illumination, while not reducing the light-fiber coupling efficiency. Based on this counter-intuitive finding, we developed a simple and efficient method of cylindrical illumination by sandpaper machining of a MMF end and angular coupling of light into the MMF. After characterization of the angular coupling effect on the emission profiles, we demonstrate the potential of our device for whole prostate PAT by volumetric imaging of a prostate-mimicking tissue phantom with a single laser shot.

5.2   Methods

5.2.1   PAT setup with angularly coupled transurethral light delivery

For this study a 1064 nm PAT device with transrectal US (TRUS) and transurethral light delivery was employed (**Fig. 5.1**). This 1064 nm PAT imaging setup is similar to our previous published work [162] with a couple minor changes. A highly compact, 6 W Nd:YAG laser with 8 ns pulse width (CFR300, Quantel-USA, Bozeman, MT, USA) was incorporated with our US system (Verasonics, Kirkland, WA, USA). The laser's 10 Hz repetition rate was externally controlled, and the laser's beam diameter was 12 mm. A Galilean beam reducer was installed before MMF coupling achieve a 2 mm beam diameter. A C9-5ICT transrectal US transducer (Philips, Andover, MA, USA) was used for US imaging and collection of the PA signal.

5.2.2   Diffusing fiber fabrication

To test a sandpaper abrasion method for creating a MMF diffuser, the ends of 1.5 mm core MMF (FP1500ERT, Thorlabs, Newton, NJ, USA) were cleaved and polished using a NanoPol Polisher (Ultra Tec Manufacturing, Inc., Santa Ana, CA, USA) with 30 μm to 0.02 μm grit diamond lapping sheets (Thorlabs, Newton, NJ, USA). The jacket and cladding were

removed from the fiber's end with a razor blade (**Fig. 5.2a**), which was the last 3.0 cm of the 1.5 mm core MMF for the initial test. Following removal of the jacket and cladding, the proximal 1.0 cm of the MMF's bare core was abraded in a multidirectional manner using a 30 μm grit fiber polishing sheet (LF30D, Thorlabs, Newton, NJ) until the abrasion appeared uniform under 10X magnification and no smooth regions of glass were observed (**Fig. 5.2c**). 30 μm grit size was chosen since 30 μm is similar to the groove width for a previously published laser micro-machined fiber diffuser [246]. To qualitatively observe the light diffusion, 405 nm was coupled to the fiber (**Fig. 5.2c**).

For the final diffusing fiber design, a 2.0 mm core MMF (APC2000, Fiberguide Industries, Stirling, NJ) with a numerical aperture of 0.37 was used to create a fiber with a 5.0 cm diffuser end. Similarly, the ends of the fiber were cleaved and polished. The jacket and cladding were then removed with a razor blade (**Fig. 5.2a**). The diffuser was then fabricated using 320 grit sandpaper (Miady, Amazon) to abrade only the side of the bare fiber end (**Fig. 5.1b**). The fiber was sanded until it appeared uniform under 10X magnification. The end surface of the diffuser was kept polished to measure forward-leaking energy.

5.2.3   Measurement of fiber coupling and side firing efficiency

Energy measurements were acquired using a 1064 nm calibrated energy sensor (QE25SP-S-MT-D0, Gentec-EO, Lake Oswego, OR,USA) in combination with the Maestro console (Gentec-EO, Lake Oswego, OR,USA), which can connect to a computer for data acquisition. The MMF was mounted using a large core fiber holder (HFS001, Thorlabs, Newton, NJ, USA) that was clamped to a 3-D stage (MBT621D, Thorlabs, Stirling, NJ, USA). This setup was then mounted onto a manual rotational stage (RP03, Thorlabs, Stirling, NJ, USA) such that the coupling from 0° to the maximum coupling angle of the fiber, which was 21.7° based on the numerical aperture, could be tested.

Fiber coupling stability when removing and reinstalling a MMF was determined by measuring the pulse energy before and after a non-diffusing MMF with polished, cleaved ends. A non-diffusing MMF was used as it is difficult to ensure all energy is measured from the diffuser end. An iris was mounted on the energy sensor so that 1064 nm energy not propagating out the fiber end could be blocked from the sensor. Between each set of measurements from 5° to 20°, the fiber was removed from the fiber holder and placed back in the fiber holder without

realignment, i.e. repositioning of the multidirectional stage. Three sets of measurements were collected of 50 pulses per coupling angle. The average and standard deviation of the three measurements were plotted.

After determining that fiber coupling was stable when switching fibers, the percentage of energy converted to side firing emission was studied by initially measuring the coupling efficiency of a non-diffusing MMF as described in the previous paragraph. Coupling angles from 0° to beyond the MMF's maximum acceptance angle were used. A MMF with a diffusing end then replaced the non-diffusing MMF in the optical pathway. The forward firing energy from the diffuser end was measured with an iris used to block the side-fired energy from the diffuser end. A total of 50 pulses were measured and averaged for each data point and plotted with the error bars representing the standard deviation of the data points.

5.2.4 Fiber emission profile measurement

The same Gentec-EO energy sensor and console was used for all energy measurements to determine emission profiles. A one mm wide slit was created using razor blades This slit was then attached to the energy sensor, which resulted in 1 mm by 25 mm slit, with the slit parallel to the MMF's long axis. The sensor with slit was mounted to a motorized rotational stage (PRM1Z8, Thorlabs, Newton, NJ, USA), which as then attached to two overlapping 25 mm 1-dimensional stages (423 Series, Newport Corporation, Irvine, CA, USA). The MMF's diffuser end was positioned so that the energy sensor would be equidistant during for all measurements. The radial emission profile was measured every 15°. To measure the longitudinal emission profile, the slit was oriented perpendicular to the MMF's long axis. The longitudinal emission was measured every two mm along the diffuser end. The plotted data is the average of 50 pulses.

5.2.5 Determining energy fluence at the capillary tube-tissue interface

First, the stability of the diffuser end's longitudinal emission profile was determined. The pulse energy was modulated with neutral density (ND) filters (Thorlabs, Newton, NJ, USA), and then, the longitudinal emission profiles were measured as described above. The curves with ND filters applied were divided by the non-filtered emission curves. The profile of this curve was predicted to have no slope if the longitudinal emission profile does not change with pulse energy

coupled. The y-intercept can then be compared to the 1064 nm transmission data from the ND filters product information.

After confirming the longitudinal emission profile stability, the area under the diffuser end's longitudinal emission curves in addition to the side firing conversion efficiencies were used to determine the average energy per pulse that needs to be coupled at each launch angle into the MMF to meet the ANSI tissue damage threshold [228], which is 100 mJ/cm^2/pulse for 1064 nm and our laser's pulse characteristics.

5.2.6 Prostate-mimicking phantom design, validation, and fabrication

To create a PA tissue mimicking phantom, the optical and acoustic properties need to be considered. For human prostate tissue, the optical properties at 1064 nm are 0.78 cm^{-1} for the absorption coefficient and 6.3 cm^{-1} for the reduced scattering coefficient [247]. For the acoustic properties, the speed of sound in human prostates is 1529 m/s, while the attenuation coefficient and slope at 5.0 MHz is 2.35 dB/cm and 0.72 dB/cm [248]. Based on these properties, 8% type A, 300-Bloom porcine gelatin (G2500, Sigma-Aldrich, St. Louis, MO, USA) was chosen for its similar acoustic properties, while being optically transparent [249,250]. To modify the optical properties of the phantom, Intralipid fat emulsion solution and black India ink have been well studied for tuning the optical properties of tissue-mimicking phantoms [249,251].

To determine the concentration of black India ink and Intralipid-20% fat emulsion solution to achieve optical properties similar to human prostate tissue, a spectrophotometer (DU 530, Beckman Coulter, Brea, CA, USA) was used to measure 1064 nm transmittance through phantom components. Three independent measurements per phantom component concentration were collected. The sample volume loaded into the cuvette (14-955-129, Fisher Scientific, Hampton, NH, USA) was 300 μL and was kept constant over all measurements to minimize error. An air-filled cuvette was used as a blank reference to obtain a measurement value for ultrapure water to compare to literature. To correct for reflection differences between an air- and a water-filled cuvette, the Fresnel equations were employed with the light's angle of incidence perpendicular to the interfaces [252]. The refractive indexes used were 1.00, 1.51, and 1.33 for air, the cuvette [253], and water respectively. The ratio of the theoretical transmission through an air-filled cuvette to a water-filled cuvette was calculated to be 0.92, which was then multiplied to

the transmission data to correct for the reflection differences. The corrected transmission data was then used to calculate the reduced optical extinction coefficient (μ'_t) as

$$\mu'_t = \frac{1}{z}ln[I],$$

where z is the path length through the cuvette in cm and I is the corrected fraction of light intensity transmitted through sample over light intensity transmitted through air in a 1 cm cuvette [249]. This calculation is valid for a highly scattering media with little absorption if the inverse mean free path is equal to or less than the sample length [249,254].

For the concentrations of black India ink and Intralipid-20% fat emulsion solution that give optical properties similar to human tissue, the optical extinction coefficient, which is a summation of the reduced scattering (μ'_s) and the absorption coefficient (μ'_a), reduces to the absorption coefficient for black India ink's values and primarily to the reduced scattering coefficient for Intralipid-20% fat emulsion solution's values [251]. Therefore, the optical extinction coefficient values for black India ink were plotted as absorption coefficient over concentration. For Intralipid-20% fat emulsion solution, the optical extinction coefficient value of water was subtracted from the data since this value is primarily comprised of absorption. The resulting values that had a mean free path less or equal to 1 cm, were then plotted as the reduced scattering coefficient over concentration. The linear fitting of these two plots were used to calculate the phantom components' concentration to achieve optical properties that match human prostate tissue's optical properties.

The mold for the prostate phantom comprised of a 5 cm by 11 cm plastic container with 7 cm depth (Ziploc medium rectangle, S. C. Johnson & Son, Racine, WI, USA). Holes were drilled into the sides of the container for the 4 mm outer diameter glass capillary tube (246 040 080, Friedrich & Dimmock, Inc., Millville, NJ, USA) and 0.5 mm pencil leads, which were placed 1.5 cm from the surface of the capillary tube. After insertion of the capillary tube and pencil leads, epoxy was used to create a waterproof seal. The phantom mixture was prepared as previously described [249]. Then, the mixture was poured into the mold and allowed to incubate overnight in 4°C before imaging. The phantom was used within 3 days to ensure stability.

5.3 Results

5.3.1 Angular coupling enhances front propagation to side emission conversion efficiency

After aligning the coupling plane of the MMF to the axis of the rotational stage, the coupling stability when removing and reinstalling a MMF was confirmed to be stable between independent measurements without adjusting the stage position (**Fig. 5.3a**). The coupling efficiency between each installment of the MMF on the holder was consistent as the standard deviation was at most 1.1% for coupling angles from 5° to 20°. The coupling efficiency was then examined for coupling angles that covered all of the MMF's acceptance angles, which is from 0° to 21.7° (**Fig. 5.3b**). The coupling efficiency is between 73.6% and 81.7% for the angles up to the maximum acceptance angle. After a coupling angle of 22°, the coupling efficiency drops to 38.8%.

The efficiency of the coupled light to emit from the side of the diffuser end as opposed to leaking out the end is shown in **Fig. 5.3b**. When the coupling angle is 0°, most of the energy per pulse is observed to emit from the MMF end with only 25.7% of the energy emitting from the diffuser's side. The conversion to side firing steeply improves to 92.8% as the coupling angle is increased to 8°. Then, the side firing conversion efficiency gradually increases to 98.8% by the maximum accepting angle of the MMF.

5.3.2 Peak of side emission profile can be longitudinally tuned by varying the coupling angle

Since the side firing conversion efficiency for the MMF's diffuser end is affected by coupling angle, the emission profiles were also evaluated. To measure the radial emission profile from the MMF's diffuser end, the slit was oriented parallel to the MMF's long axis (**Fig. 5.4a**), while the slit was oriented perpendicular to the MMF's long axis to characterize the longitudinal emission profiles (**Fig. 5.4c**). The radial profile is shown to be uniform, but the relative energy is affected by the coupling angle (**Fig. 5.4b**). The relative energy for the 0° coupling angle's radial profile ranged from 0.10 to 0.13, while the 10° and 20° have relative energy ranges of 0.74 to 0.97 and 0.88 to 1.0 respectively. In contrast to the radial emission profile, the longitudinal emission profile does not have the same relative shape over the coupling angles tested (**Fig. 5.4c**). The longitudinal emission profiles contain a peak, which shifts from the distal to proximal

end of the MMF's diffuser end as the coupling angle is increased. The broadness of the peak also shortens when the coupling angle is increased.

5.3.3 Longitudinal emission profiles can be used to determine the maximum acceptable coupling energy

Longitudinal emission profiles collected with 10° and 20° coupling angles are constant when neutral density filters were applied to attenuate the coupled pulse energy (**Fig. 5.5a,b**). With the known longitudinal emission profiles and the relatively uniform radial emission profiles, the energy fluence at the capillary tube-tissue interface can be estimated if the longitudinal emission profiles are stable when the pulse energy is modified. The area under the curve (AUC) for the normalized longitudinal emission profiles is shown in **Fig. 5.5c**. The AUC decreases as the coupling angle increases, which equates to a sharpening of the peak found in the longitudinal emission profile. To determine the maximum coupled pulse energy based on the ANSI guidelines, a uniform longitudinal emission profile was initially assumed. For a maximum energy fluence of 100 mJ/pulse/cm^2, the coupled pulse energy was then calculated to be 628.3 mJ/pulse based on a glass-capped diffuser end with 2 mm radius and 50 mm length. Then, this value was divided by the ratio of side firing energy to total energy coupled for each coupling angle (**Fig. 5.3c**) to account for energy emitting from the tip of the diffuser end. These values were then multiplied by the AUC (**Fig. 5.5c**) for the longitudinal emission profiles (**Fig. 5.4d**) after normalization. The resulting coupled energy per pulse is the theoretical maximum at which the tissue damage threshold will be reached at each coupling angle (**Fig. 5.5d**). The maximum coupled pulse energy ranges from 320 mJ/pulse when using a coupling angle of 20° up to 476 mJ/pulse when an 8° coupling angle is used.

5.3.4 Prostate-mimicking phantom for testing the 1064 nm PAT device

To confirm the radial and longitudinal PA signal generated from the cylindrically-diffusing fiber, a prostate-mimicking phantom with optical properties tuned for 1064 nm PAT needed to be determined. Black India ink and Intralipid-20% emulsion solution are known to primarily tune the absorption and reduced scattering coefficient independently at 1064 nm [251]. Here, we confirm the change in optical coefficients over varying concentration of each component for tuning the phantom's optical properties (**Fig. 5.6a,b**). The linear fit of the black India ink's absorption coefficient (**Fig. 5.6c**) resulted in a slope of 32.9 cm^{-1}/% and y-intercept of

0.149 cm^{-1}. This linear fit can be used to determine the concentration of black India ink needed for the prostate-mimicking phantom to have an absorption coefficient that approximates human prostate tissue, which is 0.78 cm^{-1} [247]. After subtracting the value of water's absorption coefficient from Intralipid-20% fat emulsion solution's optical extinction coefficient at each concentration, the data was fit with a linear curve for the reduced scattering coefficient (**Fig. 5.6d**). The slope is 2.57 cm^{-1}/% while the y-intercept is 0.02 cm^{-1}, which can be used to control the phantom's reduced scattering coefficient to match human prostate (e.g. 6.3 cm^{-1}). Based on this data, the Intralipid-20% fat emulsion solution's final concentration in the phantom is 2.44%. At this concentration of Intralipid-20% fat emulsion solution some absorption is present. The contribution to the absorption coefficient is 0.054 cm^{-1}/% for Intralipid-10% fat emulsion solution [251]. After accounting for the 2.44% of the Intralipid-20% fat emulsion solution and water's contribution to the absorption coefficient, the final concentration for black India ink in the phantom is 0.011%. After the pencil lead targets and capillary tube were epoxied into the plastic mold (**Fig. 5.6e**), the prostate-mimicking phantom was prepared with 8% gelatin and poured into the mold to incubate overnight (**Fig. 5.6f**).

5.3.5 PA signal from pencil leads in a prostate-mimicking phantom generated over the length of the diffusing fiber

The prostate-mimicking phantom was allowed to warm to room temperature directly before imaging. The phantom was placed on a sample stage as shown in **Fig. 5.1b**. The diffusing end of the transurethral MMF was inserted in the capillary tube until all 5 cm of the diffuser end was centered in the 5 cm long phantom. Collimated light was coupled into the MMF at 10° and then 20°. Maximum coupled energy into the MMF was approximately 50 mJ/pulse. PAT and US imaging of the prostate-mimicking phantom was performed from the "posterior" side of the phantom in scanning mode with a 0.2 mm step size between imaging frames (**Fig. 5.7a**). Five imaging scans were completed per fiber coupling angle. No frame averaging was performed. Average pSNR of the pencil lead was measured and plotted with error bars representing standard deviation.

The prostate-mimicking phantom with pencil lead targets underwent 1064 nm PAT and US imaging as depicted in **Fig. 5.7a**. For US and PAT pSNR, the signal is radially-uniform as demonstrated by the error bars representing the standard deviation (**Fig. 5.7b**). The pencil leads' US pSNR is relatively constant over the length of the diffuser end, while the PAT pSNR is

affected by the coupling angle. The PAT pSNR of the pencil lead is strongest for the 20°
coupling angle, which correlates to the longitudinal emission profile (**Fig. 5.4d**). While the 10°
coupling angle yields a maximum PAT pSNR that is approximately 25% lower than the
maximum PAT pSNR for the 20° coupling angle, the peak is broader for the 10° coupling angle,
allowing PAT signal to be more uniform over the length of the pencil leads. The 3-D renderings
of the PAT and US scans demonstrate the radially-uniform PA signal coinciding with the US
signal from the pencil lead (**Fig. 5.7c-f**). The PAT signal around the capillary tube is generated
from the prostate-mimicking phantom.

5.4   Discussion

5.4.1   Design of the transurethral illumination source and light coupling method

The cylindrically-diffusing fiber end designed here was inspired by a laser micro-
machined design [246]. The benefits of sandpaper abrasion compared to laser micro-machining
are that the sensitive alignment of a laser is not needed, and the only equipment needed to make
the diffuser fiber here is sandpaper. This fabrication method is also safer and faster compared to
the use of etching agent for abrading the surface or creating a tapered fiber ends [165,245].

With regard to performance, the sandpaper-abraded fiber diffuser presented here has a
radially-uniform emission profile similar to the laser micro-machined fiber diffuser [246].
Additionally, the radial emission profiles of the acid-etched fiber diffusers qualitatively appear
uniform, while the longitudinal emission profiles also appear to have a peak [165,245]. Based on
these results, our cylindrically-diffusing MMF design has a similar performance regarding the
emission profile at a low coupling angle. After considering ray optics, the improved forward to
side propagation of light when the coupling angle is increased can be explained by a higher
percentage of light interacting with the core surface at the diffuser end [255]. Therefore, we
expect other cylindrically-diffusing MMF designs to have an improved forward propagating to
side firing energy conversion when the coupling angle is increased. For example, incorporating
angular coupling into Ai *et al.*'s transurethral illumination device could allow for reduction of
the device's diameter from 8.33 mm to 4 mm. This diameter reduction would reduce the acoustic
shadowing of the anterior prostate.

A pitfall to this current study is the rigidity of the MMF, which has minimum short-term bend radius of 200 mm and minimum long term bending radius of 400 mm. A more flexible fiber would be ideal, but does not limit clinical translation as rigid urological instrumentation with diameters up to 27 French or 9 mm is commonly used [242]. The 2 mm core diameter MMF was chosen to allow for more energy per pulse to be delivered to the prostate phantom as up to 476 mJ/pulse can be delivered by our transurethral illumination source before tissue damage occurs. Besides increasing MMF core diameter, other methods exist to increase the pulse energy before fiber damage occurs. One method is to optimize the fiber end polishing method and incorporate "front face conditioning" [256]. Another method to reduce damage to the MMF is to reduce the "hot spots" in the spatial profile of the laser beam, which can be done using a beam homogenizer, which must be carefully aligned and designed to minimize diffraction effects [257], or by adjusting the laser's internal alignment [258]. Lastly, the coupled energy can be increased by reducing the peak energy per pulse by using a laser with a longer pulse width, which can range from a few ns to 10s of ns for PA signal generation [259].

If a less rigid MMF is used with the angular coupling approach presented here, increased fiber bending may result in energy loss [255]. During the experiments in this study, fiber bending at or above the minimum long-term bending radius was present. No loss in coupled energy was observed, but the effect of fiber bending on the coupling energy and illumination profiles was not studied. Energy loss can be expected when higher coupling angles that approach the numerical aperture of the MMF and fiber bending is present [255]. If fiber bending results in energy loss, a couple approaches can be taken to minimize the energy loss. One method is to choose the minimum coupling angle that maximizes the forward propagating to side firing conversion of energy at the diffuser end. Here, we show that a 10° coupling angle, which is 11.7° lower than the MMF's maximum acceptance angle, fulfills the energy conversion requirement while providing longitudinal emission across the length of the fiber for prostate PAT. Another method to overcome the loss of energy due to fiber bending would be to choose a fiber with a higher numerical aperture, which equates to a larger angle to achieve total internal reflection for energy propagation within the MMF [255]. Large core MMFs with higher numerical apertures of are available, such as Thorlab's product number FP1500ERT.

Another pitfall to the cylindrically-diffusing fiber presented here is inherent to transurethral light delivery. As the light penetrates the tissue in the radial direction from the

diffuser end, the effective surface area increases. Therefore, the energy fluence attenuates over depth due to absorption and this increase in surface area. The maximum possible energy should be used to overcome this pitfall.

5.4.2 Broader applications of angle-coupled transurethral light diffuser

The coupling angle-modulated cylindrical light diffuser presented here is optimized for transurethral light delivery for whole prostate PAT. While the primary interest in for use during the prostate biopsy procedure, another prostate-specific use could be intra-operative PAT with da Vinci robotics [260]. Beyond illumination of the prostate for PAT, the light delivery device could be used or altered for other minimally-invasive applications. For instance, this MMF diffuser could be used for PAT of lower gastrointestinal diseases in animal models [137]. This MMF diffuser could also be applied for therapeutic purposes, such as re-sensitization of bacteria with phototherapy in urinal tract infections [261].

5.5 Conclusions

We developed a transurethral light delivery approach for whole prostate illumination with sandpaper micro-machining of a multi-mode fiber end. By controlling the coupling angle into the fiber, the energy is efficiently converted and distributed along the length of the diffuser end. The device is kept to 4 mm outer diameter, which minimizes anterior prostate acoustic shadowing. The whole prostate illumination could potentially allow a urologist to freely move the US transducer to identify the biomedical target while the illumination device is statically kept in place.
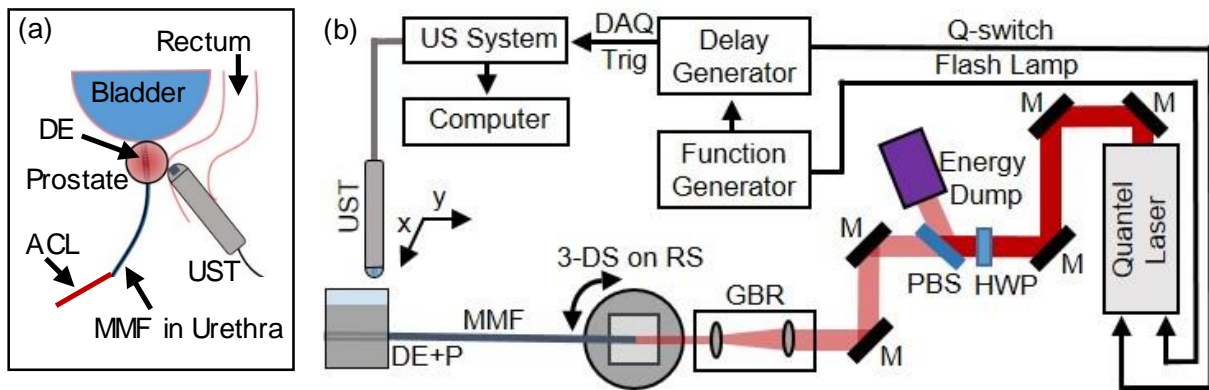
Figure 5.1. PA and US tomography with angle-coupled transurethral light delivery setup. (a) Transurethral light delivery with transrectal US imaging and PA signal collection is depicted. (b) A schematic is shown of the PA and US tomography setup used for this study. DE: diffuser end; ACL: angularly-coupled light; MMF: multimode fiber; UST: ultrasound transducer; DAQ Trig: data acquisition system trigger; M: Nd:YAG laser line 45° mirror; HWP: half wave plate; PBS: polarized beam splitter; GBR: Galilean beam reducer; 3-DS on RS: 3-dimensional stage on rotational stage; DE+P: diffuser end + phantom.
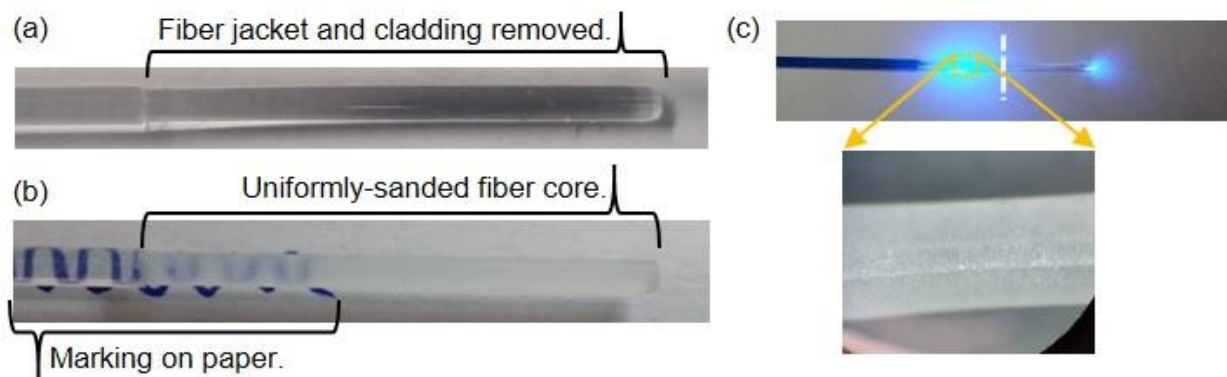
Figure 5.2. Fabrication of fiber with sandpaper-abraded diffuser end. (a) The jacket and cladding are removed from the end of a 2 mm core MMF. (b) The fiber core's surface underwent abrasion with sandpaper. A blue sine wave is drawn on the paper behind part of the abraded and unabraded fiber. (c) Light diffusion is shown at the end of a 1.5 mm core MMF with abrasion from sandpaper located left of the white dashed line. The surface of the sandpaper-abraded fiber core (orange box) is shown under 10 times magnification.
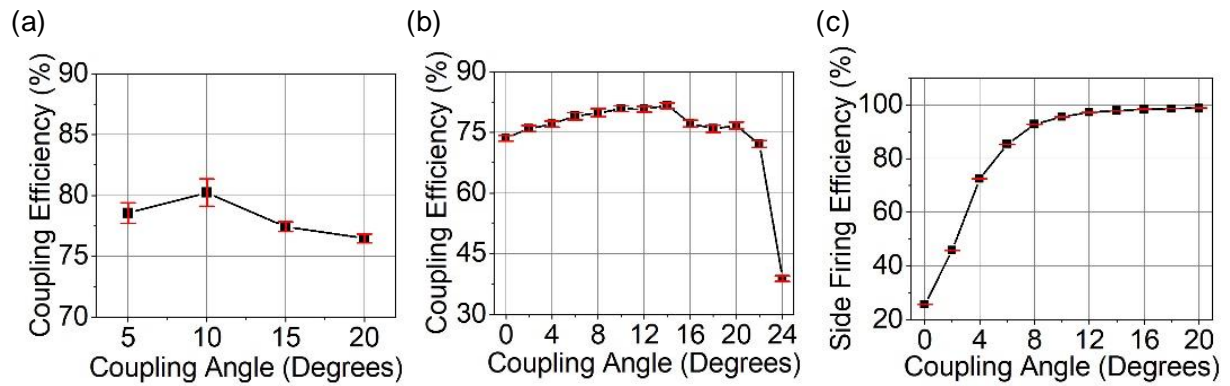
Figure 5.3. Coupling angle affects side emission conversion efficiency of the diffuser-ended fiber. (a) Fiber coupling efficiency shown from 0° coupling angle to past the numerical aperture of the fiber. (b) The percent of energy fired cylindrically from the fiber's diffuser end while increasing the coupling angle of the light. Error bars are plotted on a and b.
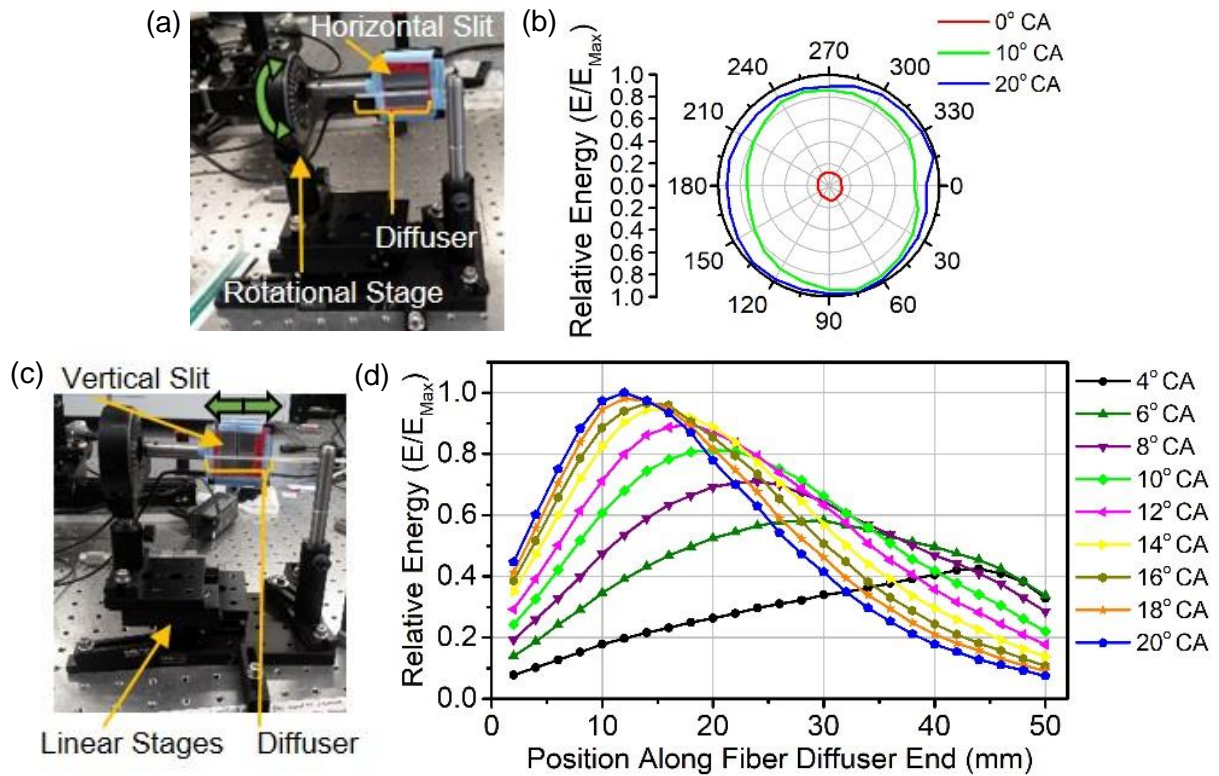
Figure 5.4. Diffuser's longitudinal emission profile is controlled by coupling angle. (a) Photograph of sensor with horizontal slit mounted on a rotational stage for radial emission profile data collection. (b) Relative radial emission profile with increasing angular coupling is graphed. (c) Photograph of sensor with vertical slit mounted on a linear stages for longitudinal emission profile data collection. (d) Relative longitudinal emission profiles are shown with angular coupling from 0° to 20°. CA: coupling angle.
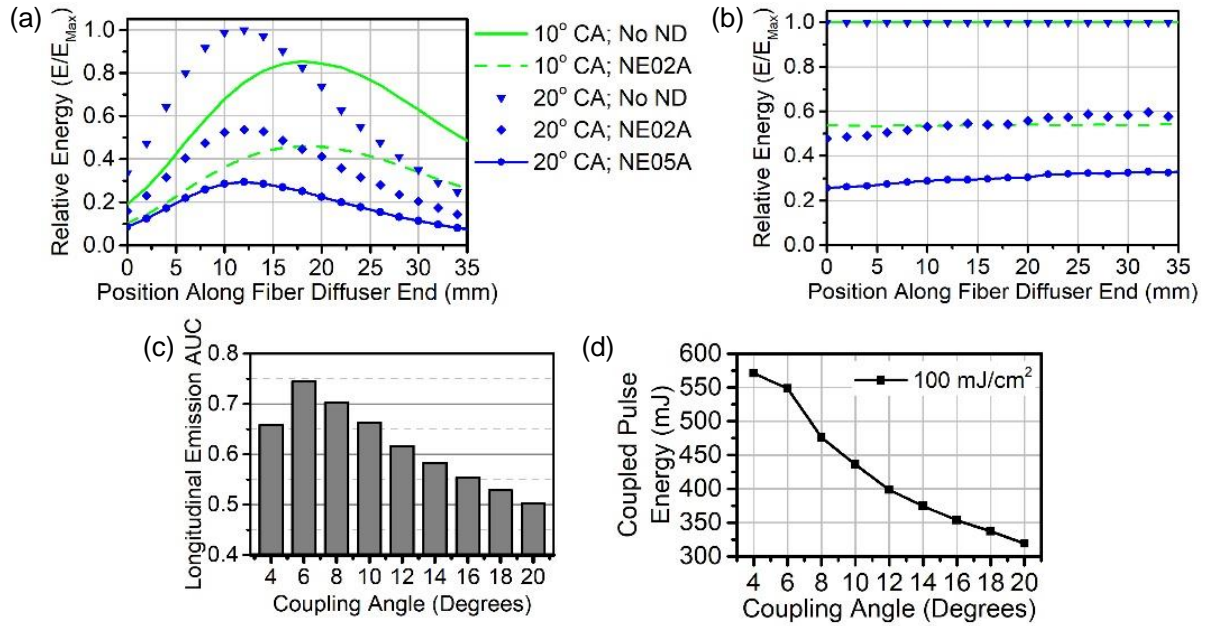
Figure 5.5. Longitudinal emission profiles can be used to determine maximum coupling energy based on the tissue damage threshold. (a) Relative longitudinal emission profiles are plotted with varying coupling angles and coupled energy into the fiber. Figure legend also applies to b. (b) These longitudinal emission profiles are shown after normalization. (c) AUC ratio for longitudinal emission profiles are illustrated over increasing coupling angle. (d) Based on the AUC ratio and the side conversion efficiency at increasing coupling angles, the maximum coupling energy is shown based on 100 mJ/cm2 light fluence at 1064 nm. CA: coupling angle; ND: neutral density filter; NE02A: 0.2 ND filter; NE05A: 0.5 ND filter. AUC: area under the curve.
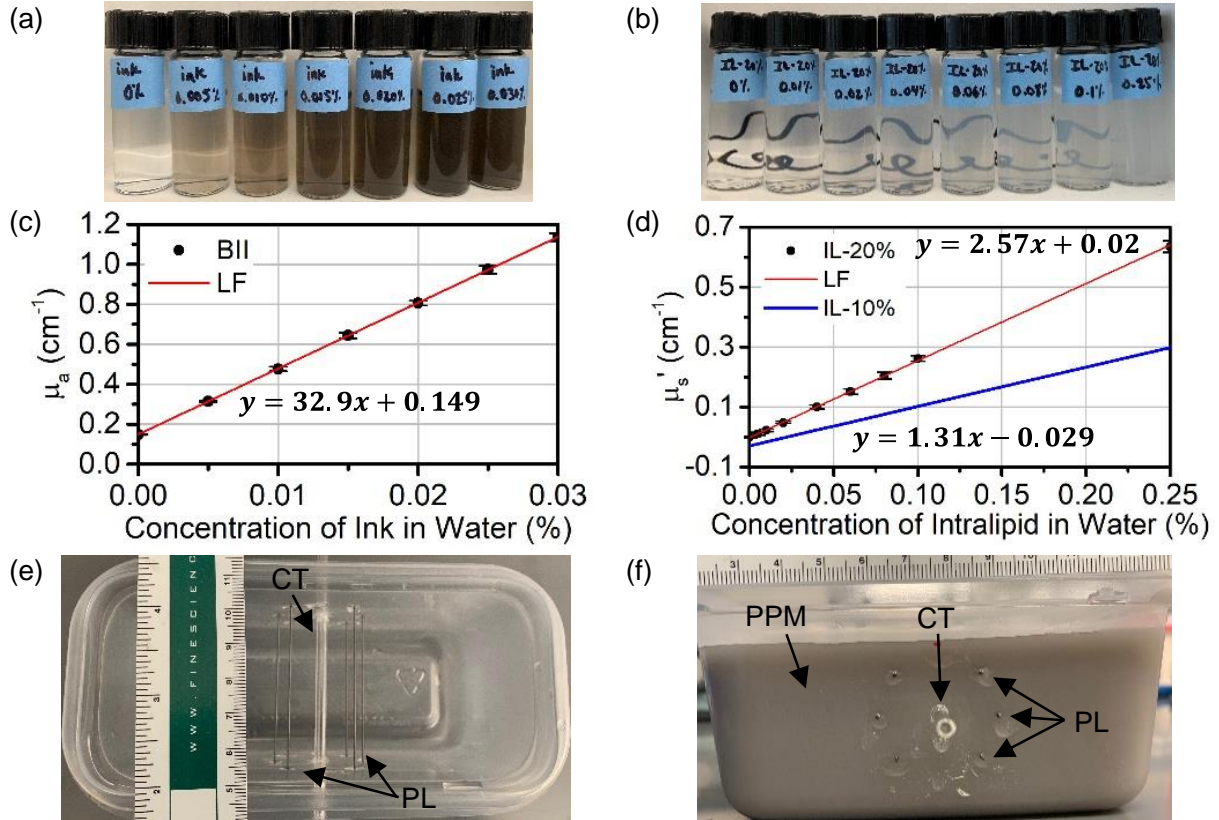
Figure 5.6. Controlling the concentration of tissue-mimicking phantom components enables direct, independent tuning of absorption and scattering for single wavelength PAT device testing. (a) Black India ink and (b) Intralipid-20% fat emulsion dilutions are shown that were used to determine μa and μs' respectively. The background for the ink dilutions is white, while the fat emulsion dilutions' background is white with curved black lines. (c) The calculated μa from the black India ink's corrected transmission data is plotted over concentration with a linear-fitted curve. (d) Similarly, a linear fitted-curve of Intralipid-20% fat emulsion's μs' over concentration. For comparison the linear fit of Intralipid-10% fat emulsion's μs' over concentration from Royston, Poston, and Prahl is plotted. (e) Top-down view of the phantom mold with capillary tube and pencil lead targets epoxied into place. (f) Front view of phantom mold with prostate-mimicking mixture added. BII: black India ink; LF: linear fit curve; IL-20%: Intralipid-20%; IL-10%: Intralipid-10%; CT: capillary tube; PL: pencil lead; PPM: prostate phantom mixture.
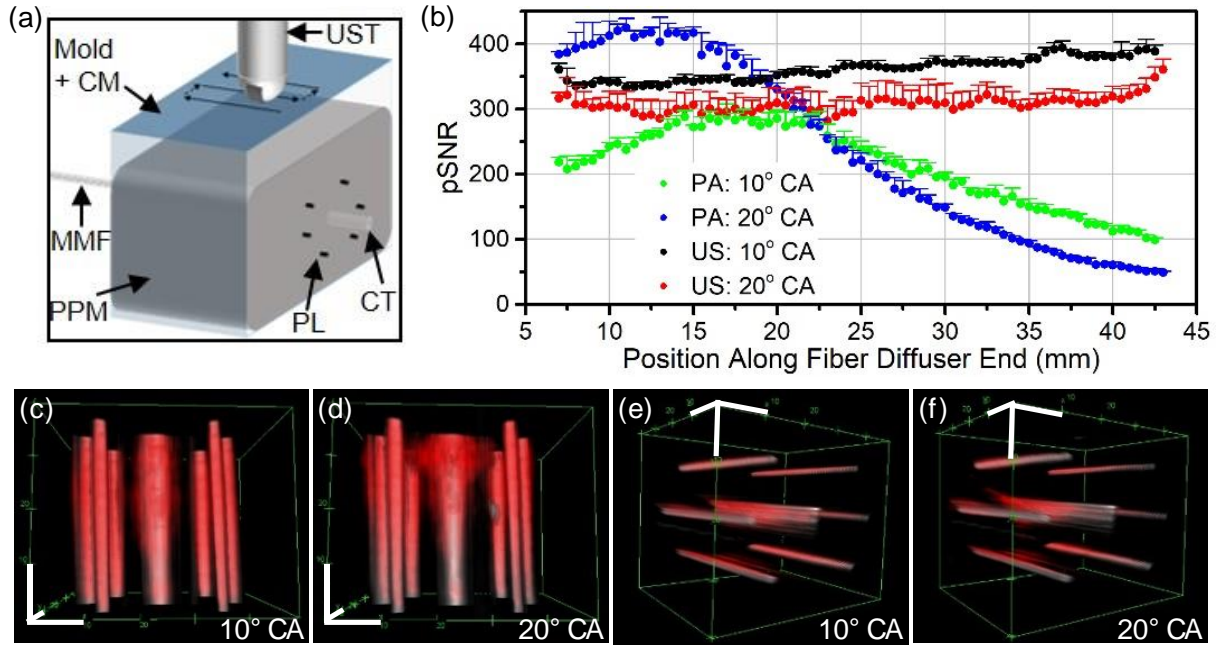
Figure 5.7. PA and US signal generated over whole prostate-mimicking phantom without moving the illumination source. (a) Schematic shown of experiment. (b) PA and US pSNR from pencil lead targets embedded in prostate-mimicking phantom is graphed over the position along the fiber diffuser from the proximal to distal end. (c-f) Snapshots of 3-D composites comprised of both the US channel (gray) and PAT channel (red) are displayed with 1 cm axis scale bars (white). Snapshots in c and d subpanels have a top-down view, while e and f subpanels' view is of signal from distal to proximal the diffuser end. CM: coupling medium; UST: ultrasound transducer; MMF: multimode fiber; PPM: prostate phantom mixture; PL: pencil lead; CT: capillary tube; CA: coupling angle.

6. CONCLUSIONS AND FUTURE DIRECTIONS

6.1   Conclusions

The MRI fusion-guided biopsy has been recently incorporated for initial prostate biopsy [1–3]. This approach, which includes acquiring biopsy cores from suspicious regions plus the standard templated TRUS-guided biopsy protocol, has greatly improved the sensitivity of the prostate biopsy [1,2]. This increased sensitivity reduces the need for repeat biopsy following a false negative result. The gains in sensitivity come with some pitfalls though, which include needing an expensive mpMRI [29], nephrotoxic contrast agents [30], and potential distortion artifacts due tissue movement during the biopsy procedure [28]. Therefore, further improvements in the prostate biopsy can be made by developing a method to provide suspicious regions in real-time.

In **Chapter 1** many US-based targeting methods were reviewed [50,53,56–58,63,64,70–75,78–80,85], but have yet to provide the improvement in sensitivity that the MRI fusion-guided prostate biopsy has [1,2]. Pure optical-based methods have suffered from limited imaging depth [130]. A hybrid imaging technique that combines diffuse optics with US is called PAT. In this method photons interact with the tissue until their ultimate absorption. The absorbed energy is in turn converted to heat, which thermodynamically expands the tissue. The resultant acoustic wave is detectable by clinical US transducer arrays, such as the ones currently used for the prostate biopsy [134,238–241]. The combination of spectroscopic information from PAT and anatomical information from US provides the potential to develop a real-time targeted prostate biopsy that could be seamlessly integrated into the clinic.

Significant work by Dogra and colleagues has shown that differences in endogenous contrast can be observed in human prostates with PAT. This work was performed on *ex vivo* human prostates specimens that were axially sliced, allowing uniform imaging of the entire anterior-posterior prostate [163,186,196]. In the clinical scenario, uniform illumination of the anterior-posterior axis of the prostate is difficult to achieve with the non-invasive access to the prostate being the rectum [165,170,171,190,200] and urethra. To determine if PAT and US imaging in a more clinically-relevant manner of intact human prostates could be used to identify targets for the prostate biopsy, we first developed a device for *ex vivo* human prostates using a

curved array TRUS with bifurcated fiber bundle (**Ch. 2**). The PAT/US imaging device was optimized for imaging 1064 nm and 1197 nm PAT, which corresponds to the endogenous contrast of hemoglobin and C-H bond [126,134]. These biomarkers were used as angiogenesis [76] and lipid accumulation [191] have been shown to be present in PCa. After optimizing the PAT/US imaging device, human prostates were imaged following radical prostatectomy. Subsequent image processing and machine learning showed that 1197 nm PAT did not provide a unique contribution to the feature learning (**Ch. 3**) [162]. With the 1064 nm PAT and US images, texture-based features learned from the training data set were able to provide targets that identified 100% of the primary and 67% of the secondary prostate tumors in the testing data set [226]. This preliminary study shows a potential for PAT/US to provide targets for the prostate biopsy

A limitation was found in the prostate imaging study—the anterior prostate, which was furthest from the light source, had a low PA signal [162]. Other recent studies imaging *in vivo* human prostates has shown a similar limitation of PAT imaging depth when a transrectal illumination source was used [170,171]. Simulation results have compared the transrectal illumination with transurethral illumination for prostate PAT [188] and suggest that transurethral illumination could improve the PAT imaging of the anterior prostate, which is important for biopsy guidance as the templated TRUS-guided prostate biopsy under samples this region of the prostate [262].

Transurethral illumination devices have improved from bevel-tipped side firing fibers [190] to cylindrically-diffusing fibers with sideways reflected emission [165]. After investigating the performance of 360° side-firing transurethral illumination devices (**Ch. 4**), the most ideal transurethral illumination device was determined to be one that illuminates the whole prostate with each pulse to eliminate the need to rotate the illumination device. The 2018 study by Ai *et al.* developed a cylindrically-diffusing fiber that showed potential for whole prostate illumination, which may be realized if the one-third of coupled light that forward propagates from the fiber end was converted to side-fired emission [165]. In **Chapter 5** a method to control the conversion efficiency of forward propagating energy to side-fired energy was elucidated. By tuning the launch angle of the energy coupled into a MMF, the side-firing conversion efficiency can be optimized and the longitudinal emission profile can be controlled for transurethral illumination of the whole prostate.

6.2   Future directions

Engineering improvements and testing are still needing to be made to translate PAT/US imaging into the clinic for targeting the prostate biopsy. The transurethral illumination device with angular coupling method (**Ch. 5**) was tested using a tissue-mimicking phantom and not in a biological sample. *Ex vivo* human prostates could be used to confirm the PAT imaging depth before progressing to *in vivo* imaging. In addition, the transurethral illumination device was fabricated using a 2 mm diameter core MMF that has a high rigidity. After adding a glass capillary tube to protect the cylindrical diffuser end, the final outer diameter was 4 mm. While these specifications can work for the application [242], a more ideal design would be one that is more flexible and has a diameter that is as compact as possible.

Another design addition that could improve prostate PAT would be to include a second illumination source incorporated into the TRUS probe. The prostate location with the highest frequency of tumor occurrence is the posterior peripheral area [201], which is furthest from the urethra and increases in the cranial prostate as the prostatic urethra has a 35° anterior bend in the middle [38]. If needed the system used in **Chapter 5** included a 6 W laser that has sufficient energy for a transurethral and a rectal illumination source. In fact, this setup already includes a polarizing beam splitter for eliminating excess energy. This excess energy could be rerouted to a fiber bundle or fibers that would be incorporated into a TRUS probe, as done by other recent studies. With the incorporation of the illumination source in the TRUS probe, the light emission should be oriented in such a way that the fluence corresponds to the acceptance area of the US transducer array. Therefore, manual manipulation of the TRUS probe would be acceptable for PAT, and studies have shown that the posterior peripheral area can have sufficient energy fluence for PAT imaging [170,171].

After optimization of the prostate PAT/US imaging device, imaging may be performed *in vivo*. Machine learning methods for identifying suspicious regions for biopsy targeting can then be tested in a living sample compared to *ex vivo* human studies, such as the one presented in **Ch. 3** [162] and by Dogra and colleagues. *In vivo* studies are especially important since hemoglobin's absorption coefficient is different between the oxy- and deoxygenated state [126,134] and if blood is coagulated [263], which occurs within minutes after the prostate is removed from the body. Therefore, *in vivo* studies are needed to ultimately test the ability for endogenous PA contrast to help guide prostate biopsy.

If the endogenous PA contrast is not sufficient, having an optimized *in vivo* human PAT/US prostate imaging system enables the testing of exogenous contrast agents. PSMA, which is a target for positron emission tomography contrast agents for PCa [207,208], is also being targeted for PAT. *In vitro* [264] and animal [192] studies have shown that PAT/US imaging of exogenous PSMA contrast agents have the potential to provide a specific PA biomarker for detecting suspicious regions for biopsy sampling.

Finally, a couple additional features would be useful for a clinical product. One of which is the ability to save the biopsy locations on the images as a reference. Knowing the exact location of the biopsy core could be helpful for patients who are opting for surveillance over surgical treatment since repeat biopsies are typically performed as a component of active surveillance [265]. In addition to tracking the core location, a three-dimensional reconstruction of the prostate that includes the suspicious regions with boundaries would be useful for comparing to pathology results, which could give insights into the accuracy of the PCa detection method.

REFERENCES

1. H. U. Ahmed, A. E. Bosaily, L. C. Brown, R. Gabe, R. Kaplan, M. K. Parmar, and Y. Collaco-moraes, "Diagnostic accuracy of multi-parametric MRI and TRUS biopsy in prostate cancer (PROMIS): a paired validating confirmatory study," Lancet **389**, 815–822 (2017).

2. A. Postema, M. Mischi, J. de la Rosette, and H. Wijkstra, "Multiparametric ultrasound in the detection of prostate cancer: a systematic review," World J. Urol. **33**, 1651–1659 (2015).

3. Y. Ueno, T. Tamada, V. Bist, C. Reinhold, H. Miyake, U. Tanaka, K. Kitajima, K. Sugimura, and S. Takahashi, "Multiparametric magnetic resonance imaging: current role in prostate cancer management," Int. J. Urol. 550–557 (2016).

4. M. A. Bjurlin, H. B. Carter, P. Schellhammer, M. S. Cookson, L. G. Gomella, D. Troyer, T. M. Wheeler, S. Schlossberg, D. F. Penson, and S. S. Taneja, "Optimization of initial prostate biopsy in clinical practice: sampling, labeling and specimen processing," J. Urol. **189**, 2039–2046 (2013).

5. J. C. Weinreb, J. O. Barentsz, P. L. Choyke, F. Cornud, M. A. Haider, K. J. Macura, D. Margolis, M. D. Schnall, F. Shtern, C. M. Tempany, H. C. Thoeny, and S. Verma, "PI-RADS prostate imaging - reporting and data system: 2015, version 2," Eur. Urol. **69**, 16–40 (2016).

6. A. Noone, N. Howlader, M. Krapcho, D. Miller, A. Brest, M. Yu, J. Ruhl, Z. Tatalovich, A. Mariotto, D. Lewis, H. Chen, E. Feuer, and K. Cronin, *SEER Cancer Statistics Review, 1975-2015* (2018).

7. H. B. Carter, P. C. Albertsen, M. J. Barry, R. Etzioni, S. J. Freedland, K. L. Greene, L. Holmberg, P. Kantoff, B. R. Konety, M. H. Murad, D. F. Penson, and A. L. Zietman, *Early Detection of Prostate Cancer: AUA Guideline* (2013), Vol. 112.

8. S. P. Balk, Y.-J. Ko, and G. J. Bubley, "Biology of Prostate-Specific Antigen," J. Clin. Oncol. **21**, 383–391 (2003).

9. D. Dalton, "Elevated serum prostate-specific antigen due to acute bacterial prostatis," Urology **33**, 465 (1989).

10. X. Game, S. Vincendeau, R. Palascak, S. Milcent, R. Fournier, and A. Houlgatte, "Total and free serum prostate specific antigen levels during the first month of acute prostatitis," Eur. Urol. **43**, 702–705 (2003).

11. M.-B. Tchetgen, J. T. Song, M. Strawderman, S. J. Jacobsen, and J. E. Oesterling, "Ejaculation increases the serum prostate-specific antigen concentration," Urology **47**, 511–6 (1996).

12. R. B. Nadler, P. a Humphrey, D. S. Smith, W. J. Catalona, and T. L. Ratliff, "Effect of inflammation and benign prostatic hyperplasia on elevated serum prostate specific antigen levels.," J. Urol. **154**, 407–413 (1995).

13. G. L. Andriole, E. D. Crawford, R. L. Grubb, S. S. Buys, D. Chia, T. R. Church, M. N. Fouad, C. Isaacs, P. A. Kvale, D. J. Reding, J. L. Weissfeld, L. A. Yokochi, B. O'Brien, L. R. Ragard, J. D. Clapp, J. M. Rathmell, T. L. Riley, A. W. Hsing, G. Izmirlian, P. F. Pinsky, B. S. Kramer, A. B. Miller, J. K. Gohagan, and P. C. Prorok, "Prostate cancer screening in the randomized prostate, lung, colorectal, and ovarian cancer screening trial: Mortality results after 13 years of follow-up," J. Natl. Cancer Inst. **104**, 125–132 (2012).

14. F. H. Schroder, J. Hugosson, M. J. Roobol, T. L. J. Tammela, S. Ciatto, V. Nelen, M. Kwiatkowski, M. Lujan, H. Lilja, M. Zappa, L. J. Denis, F. Recker, A. Paez, L. Maattanen, C. H. Bangma, G. Aus, S. Carlsson, A. Villers, X. Rebillard, T. van der Kwast, P. M. Kujala, B. G. Blijenberg, U.-H. Stenman, A. Huber, K. Taari, M. Hakama, S. M. Moss, H. J. de Koning, and A. Auvinen, "Prostate-Cancer Mortality at 11 Years of Follow-up," N. Engl. J. Med. **366**, 981–990 (2012).

15. K. Hodge, "Random Systematic Versus Directed Ultrasound Guided Transrectal Core Biopsies of the Prostate," J. Urol. **142**, 71–74 (1989).

16. A. B. Rosenkrantz, S. Verma, P. Choyke, S. C. Eberhardt, S. E. Eggener, K. Gaitonde, M. A. Haider, D. J. Margolis, L. S. Marks, P. Pinto, G. A. Sonn, and S. S. Taneja, "Prostate Magnetic Resonance Imaging and Magnetic Resonance Imaging Targeted Biopsy in Patients with a Prior Negative Biopsy: A Consensus Statement by AUA and SAR," J. Urol. **196**, 1613–1618 (2016).

17. P. R. Carroll, J. K. Parsons, G. Andriole, R. R. Bahnson, E. P. Castle, W. J. Catalona, D. M. Dahl, J. W. Davis, J. I. Epstein, R. B. Etzioni, T. Farrington, G. P. Hemstreet, M. H. Kawachi, S. Kim, P. H. Lange, K. R. Loughlin, W. Lowrance, P. Maroni, J. Mohler, T. M.

Morgan, K. A. Moses, R. B. Nadler, M. Poch, C. Scales, T. M. Shaneyfelt, M. C. Smaldone, G. Sonn, P. Sprenkle, A. J. Vickers, R. Wake, D. A. Shead, and D. A. Freedman-Cass, "Prostate cancer early detection, Version 2.2016: Featured updates to the NCCN guidelines," JNCCN J. Natl. Compr. Cancer Netw. **14**, 509–519 (2016).

18. H. G. Welch, E. S. Fisher, D. J. Gottlieb, and M. J. Barry, "Detection of prostate cancer via biopsy in the medicare-SEER population during the PSA era," J. Natl. Cancer Inst. **99**, 1395–1400 (2007).

19. C. Öbek, T. Doanca, S. Erdal, S. Erdoğan, and H. Durak, "Core length in prostate biopsy: Size matters," J. Urol. **187**, 2051–2055 (2012).

20. M. Kachanov, D. Beyersdorff, F. Preisser, D. Tilki, M. Fisch, M. Graefen, and L. Bud, "Anterior localization of prostate cancer suspicious lesions in 1,161 patients undergoing magnetic resonance imaging/ultrasound fusion guided targeted biopsies," J. Urol. **200**, 1035–1040 (2018).

21. F. Porpiglia, M. Manfredi, F. Mele, M. Cossu, E. Bollito, A. Veltri, S. Cirillo, D. Regge, R. Faletti, R. Passera, C. Fiori, and S. De Luca, "Diagnostic Pathway with Multiparametric Magnetic Resonance Imaging Versus Standard Pathway: Results from a Randomized Prospective Study in Biopsy-naïve Patients with Suspected Prostate Cancer," Eur. Urol. **72**, 282–288 (2017).

22. I. Schoots, M. Roobol, D. Nieboer, C. Bangma, E. Steyerberg, and M. Hunink, "Magnetic Resonance Imaging-targeted Biopsy May Enhance the Diagnostic Accuracy of Significant Prostate Cancer Detection Compared to Standard Transrectal Ultrasound-guided Biopsy: A Systematic Review and Meta-analysis," Eur. Urol. **68**, 438–450 (2015).

23. J. O. Barentsz, J. C. Weinreb, S. Verma, H. C. Thoeny, C. M. Tempany, F. Shtern, A. R. Padhani, D. Margolis, K. J. Macura, M. A. Haider, F. Cornud, and P. L. Choyke, "Synopsis of the PI-RADS v2 Guidelines for Multiparametric Prostate Magnetic Resonance Imaging and Recommendations for Use," Eur. Urol. **69**, 41–49 (2016).

24. P. A. Pinto, P. H. Chung, A. R. Rastinehad, A. A. Baccala Jr., J. Kruecker, C. J. Benjamin, S. Xu, P. Yan, S. Kadoury, C. Chua, J. K. Lockllin, B. Turkbey, J. H. Shih, S. P. Gates, C. Buckner, G. Bratslavsky, W. M. Linehan, N. D. Glossop, P. L. Choyke, and B. J. Wood, "Magnetic Resonance Imaging/Ultrasound Fusion Guided Prostate Biopsy Improves Cancer Detection Following Transrectal Ultrasound Biopsy and Correlates With

Multiparametric Magnetic Resonance Imaging," J. Urol. **186**, 1281–1285 (2011).

25. M. M. Siddiqui, S. Rais-Bahrami, H. Truong, L. Stamatakis, S. Vourganti, J. Nix, A. N. Hoang, A. Walton-Diaz, B. Shuch, M. Weintraub, J. Kruecker, H. Amalou, B. Turkbey, M. J. Merino, P. L. Choyke, B. J. Wood, and P. A. Pinto, "Magnetic resonance imaging/ultrasound-fusion biopsy significantly upgrades prostate cancer versus systematic 12-core transrectal ultrasound biopsy," Eur. Urol. **64**, 713–719 (2013).

26. V. K. Yarlagadda, W. S. Lai, J. B. Gordetsky, K. K. Porter, J. W. Nix, J. V. Thomas, and S. Rais-Bahrami, "MRI/US fusion-guided prostate biopsy allows for equivalent cancer detection with significantly fewer needle cores in biopsy-naive men," Diagnostic Interv. Radiol. **24**, 115–120 (2018).

27. L. Marks, S. Young, and S. Natarajan, "MRI-ultrasound fusion for guidance of targeted prostate biopsy," Curr. Opin. Urol. **23**, 43–50 (2013).

28. C. P. Filson, S. Natarajan, D. J. A. Margolis, J. Huang, P. Lieu, F. J. Dorey, R. E. Reiter, and L. S. Marks, "Prostate cancer detection with magnetic resonance-ultrasound fusion biopsy: the role of systematic and targeted biopsies," Cancer **122**, 884–892 (2016).

29. M. Davuluri, A. Toler, A. Wojtowycz, G. Bratslavsky, and S. Vourganti, "Cost of prostate MRI-US fusion– a decision analysis comparing cost effectiveness of systematic transrectal ultrasound guided biopsy and MRI-ultrasound Fusion prostate biopsy in the initial and repeat biopsy setting," J. Urol. **193**, e898–e899 (2015).

30. M. Perazella, "Gadolinium-contrast toxicity in patients with kidney disease: nephrotoxicity and nephrogenic systemic fibrosis," Curr. Drug Saf. **3**, 67–75 (2008).

31. P. F. Pinsky, H. L. Parnes, and G. Andriole, "Mortality and Complications Following Prostate Biopsy in the PLCO Cancer Screening Trial," BJU **113**, 254–259 (2014).

32. M. Ghafoori, M. Velayati, M. A. Ghasabeh, M. Shakiba, and M. Alavi, "Prostate biopsy using transrectal ultrasonography; the optimal number of cores regarding cancer detection rate and complications," Iran. J. Radiol. **12**, 0–4 (2015).

33. D. M. Marcus, M. Goodman, A. B. Jani, A. O. Osunkoya, and P. J. Rossi, "A comprehensive review of incidence and survival in patients with rare histological variants of prostate cancer in the United States from 1973 to 2008.," Prostate Cancer Prostatic Dis. **15**, 283–8 (2012).

34. D. F. Gleason and G. T. Mellinger, "Prediction of prognosis for prostatic adenocarcinoma by combined histological grading and clinical staging (reprint)," J. Urol. **167**, 953–958 (2002).

35. J. I. Epstein, W. C. J. Allsbrook, M. B. Amin, and L. L. Egevad, "The 2014 International Society of Urological Pathology (ISUP) Consensus Conference on Gleason Grading of Prostatic Carcinoma," Am. J. Surg. Pathol. **40**, 244–252 (2016).

36. P. M. Pierorazio, P. C. Walsh, A. W. Partin, and J. I. Epstein, "Prognostic Gleason grade grouping: Data based on the modified Gleason scoring system," BJU Int. **111**, 753–760 (2013).

37. N. Howlader, A. Noone, M. Krapcho, J. Garshell, D. Miller, S. Altekruse, C. Kosary, M. Yu, J. Ruhl, Z. Tatalovich, A. Mariotto, D. Lewis, H. Chen, E. Feuer, and K. Cronin, *SEER Cancer Statistics Review 1975-2010* (2016).

38. J. E. Mcneal, "The Zonal Anatomy of the Prostate," Prostate **2**, 35–49 (1981).

39. M. Zhou and K. Trpkov, "Nonneoplastic Diseases of the Prostate," in *Genitourinary Pathology: Foundations in Diangostic Pathology*, Second Edi (Elsevier Inc., 2016), pp. 1–68.

40. H. a Guess, H. M. Arrighi, E. J. Metter, and J. L. Fozard, "Cumulative prevalence of prostatism matches the autopsy prevalence of benign prostatic hyperplasia.," Prostate **17**, 241–6 (1990).

41. H. Gray, *Anatomy, Descriptive and Surgical*, 15th ed. (Running Press Book Publishers, 1974).

42. L. M. Eri, H. Thomassen, B. Brennhovd, and L. L. Håheim, "Accuracy and repeatability of prostate volume measurements by transrectal ultrasound.," Prostate Cancer Prostatic Dis. **5**, 273–278 (2002).

43. L. Cheng, T. D. Jones, C.-X. Pan, A. Barbarin, J. N. Eble, and M. O. Koch, "Anatomic distribution and pathologic characterization of small-volume prostate cancer (<0.5 ml) in whole-mount prostatectomy specimens.," Mod. Pathol. **18**, 1022–6 (2005).

44. R. Berges and M. Oelke, "Age-stratified normal values for prostate volume, PSA, maximum urinary flow rate, IPSS, and other LUTS/BPH indicators in the German male community-dwelling population aged 50 years or older," World J. Urol. **29**, 171–178 (2011).

45.   P. F. Pinsky, B. S. Kramer, E. D. Crawford, R. L. Grubb, D. A. Urban, G. L. Andriole, D. Chia, D. L. Levin, and J. K. Gohagan, "Prostate volume and prostate-specific antigen levels in men enrolled in a large screening trial," Urology **68**, 352–356 (2006).

46.   K. Hodge, J. McNeal, and T. Stamey, "Ultrasound Guided Transrectal Guided Core Biopsies of the Palpably Abnormal Prostate," J. Urol. **142**, 66–70 (1989).

47.   H. SINGH, E. I. CANTO, S. F. SHARIAT, D. KADMON, B. J. MILES, T. M. WHEELER, and K. M. SLAWIN, "Predictors of Prostate Cancer After Initial Negative Systematic 12 Core Biopsy," J. Urol. **171**, 1850–1854 (2004).

48.   M. E. Chen, D. A. Johnston, K. Tang, R. Joseph Babaian, and P. Troncoso, "Detailed mapping of prostate carcinoma foci: Biopsy strategy implications," Cancer **89**, 1800–1809 (2000).

49.   M. E. Chen, P. Troncoso, D. A. Johnston, K. Tang, and R. J. Babaian, "Optimization of prostate biopsy strategy using computer based analysis," J. Urol. **158**, 2168–2175 (1997).

50.   A. Toi, M. G. Neill, G. A. Lockwood, J. M. Sweet, L. A. Tammsalu, and N. E. Fleshner, "The Continuing Importance of Transrectal Ultrasound Identification of Prostatic Lesions," J. Urol. **177**, 516–520 (2007).

51.   O. Ukimura, K. Faber, and I. S. Gill, "Intraprostatic targeting.," Curr. Opin. Urol. **22**, 97–103 (2012).

52.   T. Loch, U. Eppelmann, J. Lehmann, B. Wullich, A. Loch, and M. Stöckle, "Transrectal ultrasound guided biopsy of the prostate: Random sextant versus biopsies of sono-morphologically suspicious lesions," World J. Urol. **22**, 357–360 (2004).

53.   J. Braeckman, P. Autier, C. Garbar, M. P. Marichal, C. Soviany, R. Nir, D. Nir, D. Michielsen, H. Bleiberg, L. Egevad, and M. Emberton, "Computer-aided ultrasonography (HistoScanning): A novel technology for locating and characterizing prostate cancer," BJU Int. **101**, 293–298 (2008).

54.   J. Schiffmann, P. Tennstedt, J. Fischer, Z. Tian, B. Beyer, K. Boehm, M. Sun, G. Gandaglia, U. Michl, M. Graefen, and G. Salomon, "Does HistoScanning[TM] predict positive results in prostate biopsy? A retrospective analysis of 1,188 sextants of the prostate," World J. Urol. **32**, 925–930 (2014).

55. J. Braeckman, P. Autier, C. Soviany, R. Nir, D. Nir, D. Michielsen, K. Treurnicht, M. Jarmulowicz, H. Bleiberg, S. Govindaraju, and M. Emberton, "The accuracy of transrectal ultrasonography supplemented with computer-aided ultrasonography for detecting small prostate cancers," BJU Int. **102**, 1560–1565 (2008).

56. S. Javed, E. Chadwick, A. A. Edwards, S. Beveridge, R. Laing, S. Bott, C. Eden, and S. Langley, "Does prostate HistoScanning play a role in detecting prostate cancer in routine clinical practice? Results from three independent studies," BJU Int. **114**, 541–548 (2014).

57. L. A. M. Simmons, P. Autier, F. Zat'ura, J. Braeckman, A. Peltier, I. Romic, A. Stenzl, K. Treurnicht, T. Walker, D. Nir, C. M. Moore, and M. Emberton, "Detection, localisation and characterisation of prostate cancer by prostate HistoScanning," BJU Int. **110**, 28–35 (2012).

58. J. Schiffmann, J. Fischer, P. Tennstedt, B. Beyer, K. Böhm, U. Michl, M. Graefen, and G. Salomon, "Comparison of prostate cancer volume measured by HistoScanning^{TM} and final histopathological results," World J. Urol. **32**, 939–944 (2014).

59. A. V Taira, G. S. Merrick, R. W. Galbreath, H. Andreini, W. Taubenslag, R. Curtis, W. M. Butler, E. Adamovich, and K. E. Wallner, "Performance of transperineal template-guided mapping biopsy in detecting prostate cancer in the initial and repeat biopsy setting.," Prostate Cancer Prostatic Dis. **13**, 71–7 (2010).

60. E. E. Christensen, T. S. Curry, and J. E. Dowdey, *Introduction to the Physics of Diagnostic Radiology*, 2nd ed. (Lea and Febeger, 1978).

61. C. P. Pavlovich, T. C. Cornish, J. K. Mullins, J. Fradin, L. Z. Mettee, J. T. Connor, A. C. Reese, F. B. Askin, R. Luck, J. I. Epstein, and H. B. Burke, "High-resolution transrectal ultrasound: Pilot study of a novel technique for imaging clinically localized prostate cancer," Urol. Oncol. Semin. Orig. Investig. **32**, 34.e27-34.e32 (2014).

62. S. Ghai, G. Eure, V. Fradet, M. E. Hyndman, T. McGrath, B. Wodlinger, and C. P. Pavlovich, "Assessing Cancer Risk on Novel 29 MHz Micro-Ultrasound Images of the Prostate: Creation of the Micro-Ultrasound Protocol for Prostate Risk Identification," J. Urol. **196**, 562–569 (2016).

63. J. Ophir, I. Cespedes, H. Ponnekanti, Y. Yazdi, and X. Li, "Elastography: A quantitative method for imaging the elasticity of biological tissues," Ultrason. Imaging **13**, 111–134 (1991).

64. B. S. Garra, "Elastography: history, principles, and technique comparison," Abdom. Imaging **40**, 680–697 (2015).

65. S. Phipps, T. H. J. Yang, F. K. Habib, R. L. Reuben, and S. A. McNeill, "Measurement of tissue mechanical characteristics to distinguish between benign and malignant prostatic disease," Urology **66**, 447–450 (2005).

66. D. W. Good, G. D. Stewart, S. Hammer, P. Scanlan, W. Shu, S. Phipps, R. Reuben, and A. S. McNeill, "Elasticity as a biomarker for prostate cancer: A systematic review," BJU Int. **113**, 523–534 (2014).

67. B. Zhang, X. Ma, W. Zhan, F. Zhu, M. Li, J. Huang, Y. Li, L. Xue, L. Liu, and Y. Wei, "Real-time elastography in the diagnosis of patients suspected of having prostate cancer: A meta-analysis," Ultrasound Med. Biol. **40**, 1400–1407 (2014).

68. Y. Zhang, J. Tang, Y. M. Li, X. Fei, E. H. He, Q. Y. Li, and H. Y. Shi, "The contribution of strain patterns in characterization of prostate peripheral zone lesions at transrectal ultrasonography," Acta Radiol **53**, 119–126 (2012).

69. L. Zhai, J. Madden, W. Foo, M. L. Palmeri, V. Mouraviev, T. Polascik, and K. Nightingale, "Acoustic Radiation Force Impulse of Human Prostates ex vivo," Ultrasound Med. Biol. **36**, 576–588 (2010).

70. L. Zhair, T. Polascik, W. Foo, S. Rosenzweig, M. L. Palmeri, J. Madden, and K. Nightingale, "Acoustic Radiation Force Impulse Imaging of Human Prostates: Initial in vivo Demonstration," Ultrasound Med. Biol. **38**, 50–61 (2012).

71. M. L. Palmeri, T. J. Glass, Z. A. Miller, S. J. Rosenzweig, A. Buck, T. J. Polascik, R. T. Gupta, A. F. Brown, J. Madden, and K. R. Nightingale, "Identifying Clinically Significant Prostate Cancers using 3-D in Vivo Acoustic Radiation Force Impulse Imaging with Whole-Mount Histology Validation," Ultrasound Med. Biol. **42**, 1251–1262 (2015).

72. S. C. Barr RG, Memo R, "Shear wave ultrasound elastography of the prostate: initial results.," Ultrasound Q. **28**, 13–20 (2012).

73. J. M. Correas, a-M. Tissier, a Khairoune, V. Vassiliu, A. Méjean, O. Hélénon, R. Memo, and R. G. Barr, "Prostate Cancer : Diagnostic Performance of Real-time Shear-Wave Elastography," Radiology **275**, 280–289 (2015).

74. K. Boehm, G. Salomon, B. Beyer, J. Schiffmann, K. Simonis, M. Graefen, and L. Budaeus, "Shear wave elastography for localization of prostate cancer lesions and assessment of elasticity thresholds: Implications for targeted biopsies and active surveillance protocols," J. Urol. **193**, 794–800 (2015).

75. K. Boehm, L. Budaus, P. Tennstedt, B. Beyer, J. Schiffmann, A. Larcher, K. Simonis, M. Graeffen, D. Beyersdorff, and G. Salomon, "Prediction of Significant Prostate Cancer at Prostate Biopsy and Per Core Detection Rate of Targeted and Systematic Biopsies Using Real-Time Shear Wave Elastography," Urol. Int. **95**, 198–196 (2015).

76. G. Russo, M. Mischi, W. Scheepens, J. J. De La Rosette, and H. Wijkstra, "Angiogenesis in prostate cancer: onset, progression and imaging," BJU Int. **110**, 794–808 (2012).

77. S. A. Bigler, R. E. Deering, and M. K. Brawer, "Comparison of microscopic vascularity in benign and malignant prostate tissue," Hum. Pathol. **24**, 220–226 (1993).

78. E. J. Halpern, F. Frauscher, S. E. Strup, L. N. Nazarian, P. O'Kane, and L. G. Gomella, "Prostate: high-frequency Doppler US imaging for cancer detection.," Radiology **225**, 71–7 (2002).

79. K. Okihara, M. Kojima, T. Nakanaouchi, K. Okada, and T. Miki, "Transrectal Power Doppler Imaging in the Detection of Prostate Cancer," BJU Int. **85**, 1053–1057 (2000).

80. H. X. Zhao, Q. Zhu, and Z. Wang, "Detection of prostate cancer with three-dimensional transrectal ultrasound: Correlation with biopsy results," Br. J. Radiol. **85**, 714–719 (2012).

81. J. L. Sauvain, E. Sauvain, P. Rohmer, D. Louis, N. Nader, R. Papavero, J. M. Bremon, and J. Jehl, "Value of transrectal power Doppler sonography in the detection of low-risk prostate cancers," Diagn. Interv. Imaging **94**, 60–67 (2013).

82. J. M. Gorce, M. Arditi, and M. Schneider, "Influence of bubble size distribution on the echogenicity of ultrasound contrast agents: a study of SonoVue," Invest. Radiol. **35**, 661–671 (2000).

83. J. Sedelaar, G. van Leenders, C. Hulsbergen-van de Kaa, H. van der Poel, J. van der Laak, F. Debruyne, H. Wijkstra, and J. de la Rosette, "Microvessel Density: Correlation between Contrast Ultrasonography and Histology of Prostate Cancer," Eur. Urol. **40**, 285–293 (2001).

84. J. P. M. Sedelaar, G. J. L. H. Van Leenders, T. E. B. Goossen, C. A. Hulsbergen-van Der Kaa, N. P. Van Adrichem, H. Wijkstra, and J. J. M. C. H. De La Rosette, "Value of contrast ultrasonography in the detection of significant prostate cancer: Correlation with radical prostatectomy specimens," Prostate **53**, 246–253 (2002).

85. M. J. Mitterberger, F. Aigner, W. Horninger, H. Ulmer, S. Cavuto, E. J. Halpern, and F. Frauscher, "Comparative efficiency of contrast-enhanced colour Doppler ultrasound targeted versus systematic biopsy for prostate cancer detection," Eur. Radiol. **20**, 2791–2796 (2010).

86. G. Taverna, G. Morandi, M. Seveso, G. Giusti, A. Benetti, P. Colombo, F. Minuti, F. Grizzi, and P. Graziotti, "Colour Doppler and microbubble contrast agent ultrasonography do not improve cancer detection rate in transrectal systematic prostate biopsy sampling," BJU Int. **108**, 1723–1727 (2011).

87. Y. Gao, X. H. Liao, L. Lu, L. Wang, Y. Ma, H. Z. Qin, X. Yan, and P. Guo, "Contrast-enhanced transrectal ultrasonography for the detection of diffuse prostate cancer," Clin. Radiol. **71**, 258–264 (2016).

88. N. Dejong, "Mechanical Index," Eur. J. Echocardiogr. **3**, 73–74 (2002).

89. M. Wink, F. Frauscher, D. Cosgrove, J. Y. Chapelon, L. Palwein, M. Mitterberger, C. Harvey, O. Rouvière, J. de la Rosette, and H. Wijkstra, "Contrast-Enhanced Ultrasound and Prostate Cancer; A Multicentre European Research Coordination Project," Eur. Urol. **54**, 982–993 (2008).

90. Y. Li, J. Tang, X. Fei, and Y. Gao, "Diagnostic Performance of Contrast Enhanced Ultrasound in Patients with Prostate Cancer. A Meta-Analysis.," Acad. Radiol. **20**, 156–164 (2013).

91. J. Jiang, Y. Chen, Y. Zhu, X. Yao, and J. Qi, "Contrast-enhanced ultrasonography for the detection and characterization of prostate cancer: Correlation with microvessel density and Gleason score," Clin. Radiol. **66**, 732–737 (2011).

92. T. E. B. Goossen, J. J. M. C. H. De La Rosette, C. a Hulsbergen-van De Kaa, G. J. L. H. Van Leenders, and H. Wijkstra, "The value of dynamic contrast enhanced power Doppler ultrasound imaging in the localization of prostate cancer.," Eur. Urol. **43**, 124–131 (2003).

93. Y. Zhu, Y. Chen, J. Jiang, R. Wang, Y. Zhou, and H. Zhang, "Contrast-enhanced harmonic ultrasonography for the assessment of prostate cancer aggressiveness: A preliminary study," Korean J. Radiol. **11**, 75–83 (2010).

94. A. B. Rosenkrantz, S. Verma, P. Choyke, S. C. Eberhardt, S. E. Eggener, K. Gaitonde, M. A. Haider, D. J. Margolis, L. S. Marks, P. Pinto, G. A. Sonn, and S. S. Taneja, "Prostate MRI and MRI-Targeted Biopsy in Patients with a Prior Negative Biopsy: A Consensus Statement of the American Urological Association and the Society of Abdominal Radiology's Prostate Cancer Disease-Focused Panel," J. Urol. (2016).

95. A. Bhavsar and S. Verma, "Anatomic imaging of the prostate.," Biomed Res. Int. **2014**, 1–9 (2014).

96. P. J. L. De Visschere, A. Vral, G. Perletti, E. Pattyn, M. Praet, V. Magri, and G. M. Villeirs, "Multiparametric magnetic resonance imaging characteristics of normal, benign and malignant conditions in the prostate," Eur. Radiol. (2016).

97. T. Tamada, T. Sone, Y. Jo, A. Yamamoto, T. Yamashita, N. Egashira, S. Imai, and M. Fukunaga, "Prostate cancer: relationships between postbiopsy hemorrhage and tumor detectability at MR diagnosis.," Radiology **248**, 531–9 (2008).

98. N. Van As, E. Charles-Edwards, A. Jackson, S. Jhavar, S. Reinsberg, N. Desouza, D. Dearnaley, M. Bailey, A. Thompson, T. Christmas, C. Fisher, C. Corbishley, and S. Sohaib, "Correlation of diffusion-weighted MRI with whole mount radical prostatectomy specimens," Br. J. Radiol. **81**, 456–462 (2008).

99. N. M. deSouza, S. F. Riches, N. J. VanAs, V. A. Morgan, S. A. Ashley, C. Fisher, G. S. Payne, and C. Parker, "Diffusion-weighted magnetic resonance imaging: a potential non-invasive marker of tumour aggressiveness in localized prostate cancer," Clin. Radiol. **63**, 774–782 (2008).

100. S. Verma, A. Rajesh, H. Morales, L. Lemen, G. Bills, M. Delworth, K. Gaitonde, J. Ying, R. Samartunga, and M. Lamba, "Assessment of aggressiveness of prostate cancer: Correlation of apparent diffusion coefficient with histologic grade after radical prostatectomy," Am. J. Roentgenol. **196**, 374–381 (2011).

101. N. J. van As, N. M. de Souza, S. F. Riches, V. A. Morgan, S. A. Sohaib, D. P. Dearnaley, and C. C. Parker, "A Study of Diffusion-Weighted Magnetic Resonance Imaging in Men with Untreated Localised Prostate Cancer on Active Surveillance," Eur. Urol. **56**, 981–988 (2009).

102. Y. Ueno, K. Kitajima, K. Sugimura, F. Kawakami, H. Miyake, M. Obara, and S. Takahashi, "Ultra-high b-value diffusion-weighted MRI for the detection of prostate cancer with 3-T MRI.," J. Magn. Reson. Imaging **38**, 154–60 (2013).

103. H. A. Vargas, O. Akin, T. Franiel, Y. Mazaheri, J. Zheng, C. Moskowitz, K. Udo, J. Eastham, and H. Hricak, "Diffusion-weighted endorectal MR imaging at 3 T for prostate cancer: tumor detection and assessment of aggressiveness.," Radiology **259**, 775–784 (2011).

104. M. R. Engelbrecht, H. J. Huisman, R. J. F. Laheij, G. J. Jager, G. J. L. H. van Leenders, C. a Hulsbergen-Van De Kaa, J. J. M. C. H. de la Rosette, J. G. Blickman, and J. O. Barentsz, "Discrimination of prostate cancer from normal peripheral zone and central gland tissue by using dynamic contrast-enhanced MR imaging.," Radiology **229**, 248–254 (2003).

105. T. Tamada, T. Sone, H. Higashi, Y. Jo, A. Yamamoto, A. Kanki, and K. Ito, "Prostate cancer detection in patients with total serum prostate-specific antigen levels of 4-10 ng/mL: Diagnostic efficacy of diffusion-weighted imaging, dynamic contrast-enhanced MRI, and T2-weighted imaging," Am. J. Roentgenol. **197**, 664–670 (2011).

106. A. Erbersdobler, H. Isbarn, K. Dix, I. Steiner, T. Schlomm, M. Mirlacher, G. Sauter, and A. Haese, "Prognostic value of microvessel density in prostate cancer: A tissue microarray study," World J. Urol. **28**, 687–692 (2010).

107. S. Guneyli, C. Z. Erdem, and L. O. Erdem, "Magnetic resonance imaging of prostate cancer," Clin. Imaging **40**, 601–609 (2016).

108. S. Verma, B. Turkbey, N. Muradyan, A. Rajesh, F. Cornud, M. A. Haider, P. L. Choyke, and M. Harisinghani, "Overview of dynamic contrast-enhanced MRI in prostate cancer diagnosis and management," Am. J. Roentgenol. **198**, 1277–1288 (2012).

109. H. Hricak, "MR imaging and MR spectroscopic imaging in the pre-treatment evaluation of prostate cancer," Br. J. Radiol. **78**, (2005).

110. S. Verma and A. Rajesh, "A clinically relevant approach to imaging prostate cancer: Review," Am. J. Roentgenol. **196**, 1–10 (2011).

111. E. Casciani, E. Polettini, L. Bertini, P. Emiliozzi, M. Amini, V. Pansadoro, and G. F. Gualdi, "Prostate cancer: evaluation with endorectal MR imaging and three-dimensional proton MR spectroscopic imaging.," Radiol. Medica **08**, 530–541 (2004).

112. J. Kurhanewicz, V. D., H. Hricak, P. Narayan, P. Carroll, and S. Nelson, "Three-dimensional H-1 MR spectroscopic imaging of the in situ human prostate with high (0.24-0.7-cm3) spatial resolution," Radiology **198**, 795–805 (1996).

113. J. C. J. Weinreb, J. J. D. Blume, F. V. F. Coakley, T. M. Wheeler, J. B. Cormack, C. K. Sotto, H. Cho, A. Kawashima, C. M. Tempany-Afdhal, K. J. Macura, M. Rosen, S. R. Gerst, and J. Kurhanewicz, "Prostate cancer: sextant localization at MR imaging and MR spectroscopic imaging before prostatectomy--results of ACRIN prospective multi-institutional clinicopathologic study.," Radiology **251**, 122–133 (2009).

114. A. B. Rosenkrantz, M. Kopec, X. Kong, J. Melamed, G. Dakwar, J. S. Babb, and B. Taouli, "Prostate cancer vs. post-biopsy hemorrhage: Diagnosis with T2- and diffusion-weighted imaging," J. Magn. Reson. Imaging **31**, 1387–1394 (2010).

115. S. Loeb, A. Berglund, and P. Stattin, "Population based study of use and determinants of active surveillance and watchful waiting for low and intermediate risk prostate cancer.," J. Urol. **190**, 1742–9 (2013).

116. R. A. Godtman, E. Holmberg, A. Khatami, C. G. Pihl, J. Stranne, and J. Hugosson, "Long-term Results of Active Surveillance in the G??teborg Randomized, Population-based Prostate Cancer Screening Trial," Eur. Urol. 1–7 (2016).

117. M. R. Cooperberg and P. R. Carroll, "Trends in Management for Patients With Localized Prostate Cancer, 1990-2013," Jama-Journal Am. Med. Assoc. **314**, 80–82 (2015).

118. T. Maurer, M. Eiber, M. Schwaiger, and J. Gschwend, "Current use of PSMA–PET in prostate cancer management," Nat. Rev. Urol. **3**, 226–235 (2016).

119. S. A. Kwee, M. N. Coel, and J. Lim, "Detection of recurrent prostate cancer with 18F-fluorocholine PET/CT in relation to PSA level at the time of imaging," Ann. Nucl. Med. **26**, 501–507 (2012).

120. K. Kitajima, R. C. Murphy, M. A. Nathan, A. T. Froemming, C. E. Hagen, N. Takahashi, and A. Kawashima, "Detection of Recurrent Prostate Cancer After Radical Prostatectomy: Comparison of 11C-Choline PET/CT with Pelvic Multiparametric MR Imaging with Endorectal Coil," J. Nucl. Med. **55**, 223–232 (2014).

121. F. Buchegger, V. Garibotto, T. Zilli, L. Allainmat, S. Jorcano, H. Vees, O. Rager, C. Steiner, H. Zaidi, Y. Seimbille, O. Ratib, and R. Miralbell, "First imaging results of an intraindividual comparison of 11C-acetate and 18F-fluorocholine PET/CT in patients with prostate cancer at early biochemical first or second relapse after prostatectomy or radiotherapy," Eur. J. Nucl. Med. Mol. Imaging **41**, 68–78 (2014).

122. H. Jadvar, "Prostate cancer: PET with 18F-FDG, 18F- or 11C-acetate, and 18F- or 11C-choline," J. Nucl. Med. **52**, 81–89 (2011).

123. Z. Yang, S. Hu, J. Cheng, J. Xu, W. Shi, B. Zhu, Y. Zhang, Z. Yao, H. Pan, and Y. Zhang, "Prevalence and risk of cancer of incidental uptake in prostate identified by fluorine-18 fluorodeoxyglucose positron emission tomography/computed tomography," Clin. Imaging **38**, 470–474 (2014).

124. B. Turkbey, E. Mena, J. Shih, P. A. Pinto, M. J. Merino, M. L. Lindenberg, M. Bernardo, Y. L. McKinney, S. Adler, R. Owenius, P. L. Choyke, and K. A. Kurdziel, "Localized prostate cancer detection with 18F FACBC PET/CT: Comparison with MR imaging and histopathologic analysis," Radiology **270**, 849–856 (2014).

125. V. Ntziachristos, "Going deeper than microscopy: the optical imaging frontier in biology.," Nat. Methods **7**, 603–614 (2010).

126. J. Hui, R. Li, E. H. Phillips, C. J. Goergen, M. Sturek, and J. X. Cheng, "Bond-selective photoacoustic imaging by converting molecular vibration into acoustic waves," Photoacoustics **4**, 11–21 (2016).

127. X. Liang, K.-H. Wang, and T. C. Zhu, "Feasibility of interstitial diffuse optical tomography using cylindrical diffusing fiber for prostate PDT," Phys. Med. Biol. **58**, 3461–3480 (2013).

128. J. Boutet, L. Herve, M. Debourdeau, L. Guyon, P. Peltie, J.-M. Dinten, L. Saroul, F. Duboeuf, and D. Vray, "Bimodal ultrasound and fluorescence approach for prostate cancer diagnosis.," J. Biomed. Opt. **14**, 064001 (2014).

129. L. V. Wang and H. Wu, *Biomedical Optics: Principles and Imaging* (John Wiley & Sons, Inc., 2007).

130. S. Kharchenko, J. Adamowicz, M. Wojtkowski, and T. Drewa, "Optical coherence tomography diagnostics for onco − urology . Review of clinical perspectives," Cent. Eur. J. Urol. **66**, 136–141 (2013).

131. B. G. Muller, D. M. de Bruin, M. J. Brandt, W. van den Bos, S. van Huystee, D. J. Faber, D. Savci, P. J. Zondervan, T. M. de Reijke, M. P. Laguna-Pes, T. G. van Leeuwen, and J. M. C. H. de la Rosette, "Prostate cancer diagnosis by optical coherence tomography: First results from a needle based optical platform for tissue sampling," J. Biophotonics **9**, n/a-n/a (2016).

132. B. G. Muller, D. M. de Bruin, W. van den Bos, M. J. Brandt, J. F. Velu, M. T. J. Bus, D. J. Faber, D. Savci, P. J. Zondervan, T. M. de Reijke, P. L. Pes, J. de la Rosette, and T. G. van Leeuwen, "Prostate cancer diagnosis: the feasibility of needle-based optical coherence tomography," J. Med. Imaging **2**, 037501–037501 (2015).

133. A. G. Bell, "On the Production and Reproduction of Sound by Light," Am. J. Sci. **20**, 305–324 (1880).

134. L. V Wang and J. Yao, "A practical guide to photoacoustic tomography in the life sciences," Nat. Methods **13**, 627–638 (2016).

135. J. Yao and L. V. Wang, "Photoacoustic tomography: fundamentals, advances and prospects," Contrast Media Mol. Imaging **6**, 332–345 (2011).

136. P. J. van den Berg, R. Bansal, K. Daoudi, W. Steenbergen, and J. Prakash, "Preclinical detection of liver fibrosis using dual-modality photoacoustic/ultrasound system," Biomed. Opt. Express **7**, 5081–5091 (2016).

137. Y. Zhu, L. A. Johnson, Z. Huang, J. M. Rubin, J. Yuan, H. Lei, J. Ni, X. Wang, P. D. R. Higgins, and G. Xu, "Identifying intestinal fibrosis and inflammation by spectroscopic photoacoustic imaging: an animal study in vivo," Biomed. Opt. Express **9**, 1590–1600 (2018).

138. R. Li, E. Phillips, P. Wang, C. J. Goergen, and J. X. Cheng, "Label-free in vivo imaging of peripheral nerve by multispectral photoacoustic tomography," J. Biophotonics **9**, 124–128 (2016).

139. L. Nie, K. Maslov, A. Garcia-uribe, M. A. Anastasio, L. V Wang, L. Nie, X. Cai, K. Maslov, A. Garcia-uribe, M. A. Anastasio, and L. V Wang, "Photoacoustic tomography through a whole adult human skull with a photon recycler," J. Biomed. Opt. Lett. **17**, 110506 (2012).

140. Y.-H. Liu, Y. Xu, L.-D. Liao, K. C. Chan, and N. V Thakor, "A handheld real-time photoacoustic imaging system for animal neurological disease models: from simulation to realization," Sensors (Basel). **18**, 4081 (2018).

141. C. B. Sussman, C. Rossignol, Q. Zhang, H. Jiang, T. Zheng, and D. Steindler, "Photoacoustic tomography can detect cerebral hemodynamic alterations in a neonatal rodent model of hypoxia-ischemia," Acta Neurobiol. Exp. (Wars). **72**, 253–263 (2012).

142. Y. Qu, C. Li, J. Shi, R. Chen, S. Xu, H. Rafsanjani, K. Maslov, H. Krigman, L. Garvey, P. Hu, P. Zhao, K. Meyers, E. Diveley, S. Pizzella, L. Muench, N. Punyamurthy, N. Goldstein, O. Onwumere, M. Alisio, K. Meyenburg, J. Maynard, K. Helm, J. Slaughter, S. Barber, T. Burger, C. Kramer, J. Chubiz, M. Anderson, R. McCarthy, S. K. England, G. A. Macones, Q. Zhou, K. K. Shung, J. Zou, M. J. Stout, M. Tuuli, and L. V Wang, "Transvaginal fast-scanning optical-resolution photoacoustic endoscopy," J. Biomed. Opt. **23**, 1–4 (2018).

143. S. Nandy, A. Mostafa, I. S. Hagemann, M. A. Powell, E. Amidi, K. Robinson, D. G. Mutch, C. Siegel, and Q. Zhu, "Evaluation of ovarian cancer: initial application of coregistered photoacoustic tomography and US," Radiology **289**, 740–747 (2018).

144. S. E. Bohndiek, L. S. Sasportas, S. Machtaler, J. V Jokerst, S. Hori, and S. S. Gambhir, "Photoacoustic tomography detects early vessel regression and normalization during ovarian tumor response to the antiangiogenic therapy trebananib," J. Nucl. Med. **56**, 1942–1947 (2015).

145. M. Heijblom, D. Piras, M. Brinkhuis, J. C. G. van Hespen, F. M. van den Engh, M. van der Schaaf, J. M. Klaase, T. G. van Leeuwen, W. Steenbergen, and S. Manohar, "Photoacoustic image patterns of breast carcinoma and comparisons with Magnetic Resonance Imaging and vascular stained histopathology," Sci. Rep. **5**, 11778 (2015).

146. R. Li, P. Wang, L. Lan, F. P. Lloyd, C. J. Goergen, S. Chen, and J.-X. Cheng, "Assessing breast tumor margin by multispectral photoacoustic tomography," Biomed. Opt. Express **6**, 1273–1281 (2015).

147. L. Xi, S. R. Grobmyer, L. Wu, R. Chen, G. Zhou, L. G. Gutwein, J. Sun, W. Liao, Q. Zhou, H. Xie, and H. Jiang, "Evaluation of breast tumor margins in vivo with intraoperative photoacoustic imaging," Opt. Express **20**, 8726–8731 (2012).

148. S. Manohar, S. E. Vaartjes, J. C. G. van Hespen, J. M. Klaase, F. M. van den Engh, W. Steenbergen, and T. G. van Leeuwen, "Initial results of in vivo non-invasive cancer imaging in the human breast using near-infrared photoacoustics," Opt. Express **15**, 12277–12285 (2007).

149. R. A. Kruger, R. B. Lam, D. R. Reinecke, S. P. Del Rio, and R. P. Doyle, "Photoacoustic angiography of the breast," Med. Phys. **37**, 6096–6100 (2010).

150. X. Leng, W. Chapman Jr, B. Rao, S. Nandy, R. Chen, R. Rais, I. Gonzalez, Q. Zhou, D. Chatterjee, M. Mutch, and Q. Zhu, "Feasibility of co-registered ultrasound and acoustic-resolution photoacoustic imaging of human colorectal cancer," Biomed. Opt. Express **9**, 5159–5172 (2018).

151. F. Knieling, C. Neufert, A. Hartmann, J. Claussen, A. Urich, C. Egger, M. Vetter, S. Fischer, L. Pfeifer, A. Hagel, C. Kielisch, R. S. Görtz, D. Wildner, M. Engel, J. Röther, W. Uter, J. Siebler, R. Atreya, W. Rascher, D. Strobel, M. F. Neurath, and M. J. Waldner, "Multispectral optoacoustic tomography for assessment of crohn's disease activity," N. Engl. J. Med. **376**, 1292–1294 (2017).

152. A. Shah, T. Delgado-Goni, T. Casals Galobart, S. Wantuch, Y. Jamin, M. O. Leach, S. P. Robinson, J. Bamber, and M. Beloueche-Babari, "Detecting human melanoma cell re-differentiation following BRAF or heat shock protein 90 inhibition using photoacoustic and magnetic resonance imaging," Sci. Rep. **7**, 8215 (2017).

153. R. M. Weight, J. A. Viator, P. S. Dale, C. W. Caldwell, and A. E. Lisle, "Photoacoustic detection of metastatic melanoma cells in the human circulatory system," Opt. Lett. **31**, 2998–3000 (2006).

154. Y. Wang, D. Xu, S. Yang, and D. Xing, "Toward in vivo biopsy of melanoma based on photoacoustic and ultrasound dual imaging with an integrated detector," Biomed. Opt. Express **7**, 279–286 (2016).

155. Y. Zhou, W. Xing, K. I. Maslov, L. A. Cornelius, and L. V Wang, "Handheld photoacoustic microscopy to detect melanoma depth in vivo," Opt. Lett. **39**, 4731–4734 (2014).

156. X. Li, D. Wang, H. Ran, L. Hao, Y. Cao, M. Ao, N. Zhang, J. Song, L. Zhang, H. Yi, Z. Wang, and P. Li, "A preliminary study of photoacoustic/ultrasound dual-mode imaging in melanoma using MAGE-targeted gold nanoparticles," Biochem. Biophys. Res. Commun. **502**, 255–261 (2018).

157. Y. Cao, J. Hui, A. Kole, P. Wang, Q. Yu, W. Chen, M. Sturek, and J.-X. Cheng, "High-sensitivity intravascular photoacoustic imaging of lipid–laden plaque with a collinear catheter design," Sci. Rep. **6**, 25236 (2016).

158. J. Hui, R. Li, P. Wang, E. Phillips, R. Bruning, C.-S. Liao, M. Sturek, C. J. Goergen, and J.-X. Cheng, "Assessing carotid atherosclerosis by fiber-optic multispectral photoacoustic tomography," Proc. SPIE **9323**, 93233S (2015).

159. T. J. Allen, P. C. Beard, A. Hall, A. P. Dhillon, and J. S. Owen, "Spectroscopic photoacoustic imaging of lipid-rich plaques in the human aorta in the 740 to 1400 nm wavelength range," J. Biomed. Opt. **17**, 61209–61211 (2012).

160. D. Razansky, N. J. Harlaar, J. L. Hillebrands, A. Taruttis, E. Herzog, C. J. Zeebregts, G. M. Van Dam, and V. Ntziachristos, "Multispectral optoacoustic tomography of matrix metalloproteinase activity in vulnerable human carotid plaques," Mol. Imaging Biol. **14**, 277–285 (2012).

161. I. M. Graf, S. Kim, B. Wang, R. Smalling, and S. Emelianov, "Noninvasive detection of intimal xanthoma using combined ultrasound, strain rate and photoacoustic imaging," Ultrasonics **52**, 435–441 (2012).

162. B. Bungart, L. Lan, P. Wang, R. Li, M. O. Koch, L. Cheng, T. A. Masterson, M. Dundar, and J. Cheng, "Photoacoustic tomography of intact human prostates and vascular texture analysis identify prostate cancer biopsy targets," Photoacoustics **11**, 46–55 (2018).

163. S. Sinha, N. A. Rao, B. K. Chinni, and V. S. Dogra, "Evaluation of frequency domain analysis of a multiwavelength photoacoustic signal for differentiating malignant from benign and normal prostates: ex vivo study with human prostates," J. Ultrasound Med. **35**, 2165–2177 (2016).

164. R. E. Kumon, C. X. Deng, and X. Wang, "Frequency-domain analysis of photoacoustic imaging data from prostate adenocarcinoma tumors in a murine model," Ultrasound Med. Biol. **37**, 834–839 (2012).

165. M. Ai, T. Salcudean, R. Rohling, P. Abolmaesumi, and S. Tang, "Transurethral illumination probe design for deep photoacoustic imaging of prostate," in *Proceedings of SPIE* (SPIE, 2018), Vol. 10494, p. 104940C.

166. H. K. Zhang, Y. Chen, J. Kang, A. Lisok, I. Minn, M. G. Pomper, and E. M. Boctor, "Prostate specific membrane antigen-targeted photoacoustic imaging of prostate cancer in vivo," J. Biophotonics e201800021 (2018).

167. J. L. Su, R. R. Bouchard, A. B. Karpiouk, J. D. Hazle, and S. Y. Emelianov, "Photoacoustic imaging of prostate brachytherapy seeds," Biomed. Opt. Express **2**, 17–24 (2011).

168. X. Wang, W. W. Roberts, P. L. Carson, D. P. Wood, and J. B. Fowlkes, "Photoacoustic tomography: a potential new tool for prostate cancer," Biomed. Opt. Express **1**, 1117–1126 (2010).

169. S. Huang, J. T. Wei, S. A. Tomlins, J. B. Fowlkes, and P. L. Carson, "Interstitial assessment of aggressive prostate cancer by physio-chemical photoacoustics : an ex vivo study with intact human prostates," Med. Phys. **45**, 4125–4132 (2018).

170. A. Horiguchi, K. Tsujita, K. Irisawa, T. Kasamatsu, K. Hirota, M. Kawaguchi, M. Shinchi, K. Ito, T. Asano, H. Shinmoto, H. Tsuda, and M. Ishihara, "A pilot study of photoacoustic imaging system for improved real-time visualization of neurovascular bundle during radical prostatectomy," Prostate **76**, 307–315 (2016).

171. A. Horiguchi, M. Shinchi, A. Nakamura, T. Wada, K. Ito, T. Asano, H. Shinmoto, H. Tsuda, and M. Ishihara, "Pilot study of prostate cancer angiogenesis imaging using a photoacoustic imaging system," Urology **108**, 212–219 (2017).

172. Z. Xie, W. Roberts, P. Carson, X. Liu, C. Tao, and X. Wang, "Evaluation of bladder microvasculature with high-resolution photoacoustic imaging," Opt. Lett. **36**, 4815–4817 (2011).

173. A. Kamaya, S. Vaithilingam, B. I. Chung, O. Oralkan, and B. T. Khuri-Yakub, "Photoacoustic imaging of the bladder: a pilot study," J. Ultrasound Med. **32**, 1245–1250 (2013).

174. C. Kim, M. Jeon, and L. V Wang, "Nonionizing photoacoustic cystography in vivo," Opt. Lett. **36**, 3599–3601 (2011).

175. K. Sivasubramanian, V. Periyasamy, R. A. Dienzo, and M. Pramanik, "Hand-held, clinical dual mode ultrasound - photoacoustic imaging of rat urinary bladder and its applications," J. Biophotonics **11**, e201700317 (2018).

176. O. Ogunlade, J. J. Connell, J. L. Huang, E. Zhang, M. F. Lythgoe, D. A. Long, and P. Beard, "In vivo three-dimensional photoacoustic imaging of the renal vasculature in preclinical rodent models," Am. J. Physiol. Physiol. **314**, F1145–F1153 (2017).

177. K. Okumura, J. Matsumoto, Y. Iwata, K. Yoshida, N. Yoneda, T. Ogi, A. Kitao, K. Kozaka, W. Koda, S. Kobayashi, D. Inoue, N. Sakai, K. Furuichi, T. Wada, and T. Gabata, "Evaluation of renal oxygen saturation using photoacoustic imaging for the early prediction of chronic renal function in a model of ischemia-induced acute kidney injury," PLoS One **13**, e0206461 (2018).

178. E. S. L. Berndl, X. He, D. A. Yuen, and M. C. Kolios, "Photoacoustic imaging for assessing ischemic kidney damage in vivo," in *Proceedings of SPIE* (2018), Vol. 10494, p. 104941P–10494–7.

179. C. Ungureanu, "Contrast agents for photoacoustic imaging," Growth (Lakeland) **13**, 639–650 (2016).

180. P. Wang, T. Ma, M. N. Slipchenko, S. Liang, J. Hui, K. K. Shung, S. Roy, M. Sturek, Q. Zhou, Z. Chen, and J.-X. Cheng, "High-speed intravascular photoacoustic imaging of lipid-laden atherosclerotic plaque enabled by a 2-kHz barium nitrite raman laser," Sci. Rep. **4**, 6889 (2014).

181. P. Wang, J. R. Rajian, and J.-X. Cheng, "Spectroscopic Imaging of Deep Tissue through Photoacoustic Detection of Molecular Vibration," J. Phys. Chem. Lett. **4**, 2177–2185 (2013).

182. V. S. Dogra, B. K. Chinni, K. S. Valluru, J. V. Joseph, A. Ghazi, J. L. Yao, K. Evans, E. M. Messing, and N. A. Rao, "Multispectral Photoacoustic Imaging of Prostate Cancer: Preliminary Ex-vivo Results," J. Clin. Imaging Sci. **3**, 41 (2013).

183. M. A. Yaseen, S. A. Ermilov, H.-P. Brecht, R. Su, A. Conjusteau, M. Fronheiser, B. A. Bell, M. Motamedi, and A. A. Oraevsky, "Optoacoustic imaging of the prostate: development toward image-guided biopsy.," J. Biomed. Opt. **15**, 021310 (2010).

184. M. P. Patterson, C. B. Riley, M. C. Kolios, and W. M. Whelan, "Optoacoustic characterization of prostate cancer in an in vivo transgenic murine model.," J. Biomed. Opt. **19**, 056008 (2014).

185. G. Xu, M. C. Davis, J. Siddiqui, S. A. Tomlins, S. Huang, L. P. Kunju, J. T. Wei, and X. Wang, "Quantifying Gleason scores with photoacoustic spectral analysis: feasibility study with human tissues.," Biomed. Opt. Express **6**, 4781–9 (2015).

186. A. R. Rajanna, R. Ptucha, S. Sinha, B. Chinni, V. Dogra, and N. A. Rao, "Prostate cancer detection using photoacoustic imaging and deep learning," in *IS&T International Symposium on Electronic Imaging* (2016), pp. 1–6.

187. A. Bashkatov, E. Genina, V. Kochubey, V. Rubtsov, E. Kolesnikova, and V. Tuchin, "Optical properties of human colon tissues in the 350 – 2500 nm spectral range," Quantum Electron. **44**, 779–784 (2014).

188. S. Tang, J. Chen, P. Samant, S. Kelly, and L. Xiang, "Transurethral photoacoustic endoscopy for prostate cancer: a simulation study," in *IEEE Transactions on Medical Imaging* (2016), Vol. 35, pp. 1780–1787.

189. T. Mitcham, K. Dextraze, H. Taghavi, M. Melancon, and R. Bouchard, "Photoacoustic imaging driven by an interstitial irradiation source," Photoacoustics **3**, 45–54 (2015).

190. M. A. Lediju Bell, X. Guo, D. Y. Song, and E. M. Boctor, "Transurethral light delivery for prostate photoacoustic imaging," J. Biomed. Opt. **20**, 036002 (2015).

191. S. Yue, J. Li, S.-Y. Lee, H. J. Lee, T. Shao, B. Song, L. Cheng, T. A. Masterson, X. Liu, T. L. Ratliff, and J.-X. Cheng, "Cholesteryl ester accumulation induced by PTEN loss and PI3K/AKT activation underlies human prostate cancer aggressiveness," Cell Metab. **19**, 393–406 (2014).

192. H. K. Zhang, Y. Chen, J. Kang, A. Lisok, I. Minn, M. G. Pomper, and E. M. Boctor, "Prostate-specific membrane antigen-targeted photoacoustic imaging of prostate cancer in vivo," J. Biophotonics **11**, e201800021 (2018).

193. V. Dogra, B. Chinni, S. Singh, H. Schmitthenner, N. Rao, J. J. Krolewski, and K. L. Nastiuk, "Photoacoustic imaging with an acoustic lens detects prostate cancer cells labeled with PSMA-targeting near-infrared dye-conjugates," J. Biomed. Opt. **21**, 066019 (2016).

194. G. Xu, M. Qin, A. Mukundan, J. Siddiqui, M. Takada, P. Vilar-, S. A. Tomlins, R. Kopelman, and X. Wang, "Prostate cancer characterization by optical contrast enhanced photoacoustics," in *Proc. of SPIE* (2016), p. 9708.

195. J. Levi, A. Sathirachinda, and S. S. Gambhir, "A high-affinity, high-stability photoacoustic agent for imaging gastrin-releasing peptide receptor in prostate cancer," Clin. Cancer Res. An Off. J. Am. Assoc. Cancer Res. **20**, 3721–3729 (2014).

196. V. S. Dogra, B. K. Chinni, K. S. Valluru, J. V Joseph, A. Ghazi, J. L. Yao, K. Evans, E. M. Messing, and N. a Rao, "Multispectral Photoacoustic Imaging of Prostate Cancer: Preliminary Ex-vivo Results.," J. Clin. Imaging Sci. **3**, 41 (2013).

197. S. Tang, J. Chen, P. Samant, S. Kelly, and L. Xiang, "Transurethral Photoacoustic Endoscopy for Prostate Cancer: A Simulation Study," IEEE Trans. Med. Imaging (2016).

198. K. T. Tokala, D. Piao, and G. Xu, "A geometric-sensitivity-difference method improves object depth-localization for continuous-wave fluorescence diffuse optical tomography: An in silico study in an axial outward-imaging geometry," J. Xray. Sci. Technol. **22**, 627–643 (2014).

199. J. Wu, L. You, L. Lan, H. J. Lee, S. T. Chaudhry, R. Li, J. X. Cheng, and J. Mei, "Semiconducting Polymer Nanoparticles for Centimeters-Deep Photoacoustic Imaging in the Second Near-Infrared Window," Adv. Mater. **29**, 1–6 (2017).

200. R. L. Drake, A. W. Vogl, and A. W. M. Mitchell, "Pelvis and Perineum," in *Gray's Atlas of Anatomy*, Second (Churchill Livingston, Elsevier Inc., 2015), pp. 212–284.

201. O. Eminaga, A. Semjonow, E. Eltze, O. Bettendorf, A. Schultheis, U. Warnecke-Eberz, I. Akbarov, S. Wille, and U. Engelmann, "Analysis of topographical distribution of prostate cancer and related pathological findings in prostatectomy specimens using cMDX document architecture," J. Biomed. Inform. **59**, 240–247 (2016).

202. D. M. Schuster, B. Savir-baruch, P. T. Nieh, V. A. Master, R. K. Halkar, P. J. Rossi, M. M. Lewis, J. A. Nye, W. Yu, and F. D. Bowman, "Detection of Recurrent Prostate Carcinoma with anti -1-Amino- 3- 18 F-Fluorocyclobutane-1-Carboxylic Acid PET / CT and 111 In − Capromab Pendetide SPECT / CT," Radiology **2010**, (2011).

203. D. M. Schuster, P. a Taleghani, P. T. Nieh, V. a Master, R. Amzat, B. Savir-Baruch, R. K. Halkar, T. Fox, A. O. Osunkoya, C. S. Moreno, J. a Nye, W. Yu, B. Fei, Z. Wang, Z. Chen, and M. M. Goodman, "Characterization of primary prostate carcinoma by anti-1-

amino-2-[(18)F] -fluorocyclobutane-1-carboxylic acid (anti-3-[(18)F] FACBC) uptake.," Am. J. Nucl. Med. Mol. Imaging **3**, 85–96 (2013).

204. M. Cimitan, R. Bortolus, S. Morassut, V. Canzonieri, A. Garbeglio, T. Baresic, E. Borsatti, A. Drigo, and M. G. Trovò, "[18F]fluorocholine PET/CT imaging for the detection of recurrent prostate cancer at PSA relapse: Experience in 100 consecutive patients," Eur. J. Nucl. Med. Mol. Imaging **33**, 1387–1398 (2006).

205. F. E. von Eyben and K. Kairemo, "Meta-analysis of (11)C-choline and (18)F-choline PET/CT for management of patients with prostate cancer.," Nucl. Med. Commun. **35**, 221–30 (2014).

206. B. Mohsen, T. Giorgio, Z. S. Rasoul, L. Werner, G. R. M. Ali, D. K. V. Reza, and S. Ramin, "Application of ^{11} C-acetate positron-emission tomography (PET) imaging in prostate cancer: systematic review and meta-analysis of the literature," BJU Int. **112**, 1062–1072 (2013).

207. T. Maurer, J. E. Gschwend, I. Rauscher, M. Souvatzoglou, B. Haller, G. Weirich, H.-J. Wester, M. Heck, H. Kübler, A. J. Beer, M. Schwaiger, and M. Eiber, "Diagnostic Efficacy of 68Gallium-PSMA-PET compared to Conventional Imaging in Lymph Node Staging of of 130 consecutive Patients with Intermediate to High-Risk Prostate Cancer," J. Urol. **195**, 1436–1443 (2015).

208. P. J. Van Leeuwen, P. Stricker, G. Hruby, A. Kneebone, F. Ting, B. Thompson, Q. Nguyen, B. Ho, and L. Emmett, "68Ga-PSMA has a high detection rate of prostate cancer recurrence outside the prostatic fossa in patients being considered for salvage radiation treatment," BJU Int. **117**, 732–739 (2016).

209. J. S. Ross, C. E. Sheehan, H. a G. Fisher, R. P. Kaufman, P. Kaur, K. Gray, I. Webb, G. S. Gray, R. Mosher, and B. V. S. Kallakury, "Correlation of primary tumor prostate-specific membrane antigen expression with disease recurrence in prostate cancer.," Clin. Cancer Res. **9**, 6357–6362 (2003).

210. R. L. Siegel, K. D. Miller, and A. Jemal, "Cancer statistics, 2018," CA. Cancer J. Clin. **68**, 7–30 (2018).

211. G. S. Sandhu and G. L. Andriole, "Overdiagnosis of prostate cancer," J. Natl. Cancer Inst. - Monogr. **2011**, 146–151 (2012).

212. J. J. Fenton, M. S. Weyrich, S. Durbin, Y. Liu, H. Bang, and J. Melnikow, *Prostate-Specific Antigen–Based Screening for Prostate Cancer: A Systematic Evidence Review for the U.S. Preventative Services Task Force. Evidence Synthesis No. 154. AHRQ Publication No. 17-05229-EF-1.* (2018).

213. M. T. C. S. F. Martin G. Sanda, MD; Ronald C. Chen, M. J. B. MD; Kirsten Greene, MD; Laurence H. Klotz, MD; Danil V. Makarov, M. Nelson, MD; James Reston, PhD; George Rodrigues, MD; Howard M. Sandler, and M. Mary Ellen Taplin, MD; Jeffrey A. Cadeddu, "Clinically Localized Prostate Cancer : American Urological Association (AUA) / American Society for Radiation Oncology (ASTRO) / Society of Urologic Oncology (SUO) Clinically Localized Prostate Cancer," Am. Urol. Assoc. 1–56 (2017).

214. M. A. Levine, M. Ittman, J. Melamed, and H. Lepor, "Two consecutive sets of transrectal ultrasound guided sextant biopsies of the prostate for the detection of prostate cancer," J. Urol. **159**, 471–476 (1998).

215. M. M. Siddiqui, A. K. George, R. Rubin, S. Rais-Bahrami, H. L. Parnes, M. J. Merino, R. M. Simon, B. Turkbey, P. L. Choyke, B. J. Wood, and P. A. Pinto, "Efficiency of Prostate Cancer Diagnosis by MR/Ultrasound Fusion-Guided Biopsy vs Standard Extended-Sextant Biopsy for MR-Visible Lesions," J. Natl. Cancer Inst. **108**, 1–7 (2016).

216. A. Borkowetz, B. Hadaschik, I. Platzek, M. Toma, G. Torsev, T. Renner, R. Herout, M. Baunacke, M. Laniado, G. Baretton, J. P. Radtke, C. Kesch, M. Hohenfellner, M. Froehner, H. P. Schlemmer, M. Wirth, and S. Zastrow, "Prospective comparison of transperineal magnetic resonance imaging/ultrasonography fusion biopsy and transrectal systematic biopsy in biopsy-naïve patients," BJU Int. **121**, 53–60 (2018).

217. P. P. Tonttila, J. Lantto, E. Pääkkö, U. Piippo, S. Kauppila, E. Lammentausta, P. Ohtonen, and M. H. Vaarala, "Prebiopsy Multiparametric Magnetic Resonance Imaging for Prostate Cancer Diagnosis in Biopsy-naive Men with Suspected Prostate Cancer Based on Elevated Prostate-specific Antigen Values: Results from a Randomized Prospective Blinded Controlled Trial," Eur. Urol. **69**, 419–425 (2016).

218. S. T. L. and L. P. A., "Ultrasound Transducer Selection in Clinical Imaging Practice," J. Ultrasound Med. **32**, 573–582 (2013).

219. J. R. Rajian, R. Li, P. Wang, and J.-X. Cheng, "Vibrational Photoacoustic Tomography: Chemical Imaging beyond the Ballistic Regime," J. Phys. Chem. Lett. **4**, 3211–3215 (2013).

220. S. Hu, "Emerging concepts in functional and molecular photoacoustic imaging," Curr. Opin. Chem. Biol. **33**, 25–31 (2016).

221. Y. Cao, A. Kole, J. Hui, Y. Zhang, J. Mai, M. Alloosh, M. Sturek, and J. X. Cheng, "Fast assessment of lipid content in arteries in vivo by intravascular photoacoustic tomography," Sci. Rep. **8**, 1–10 (2018).

222. M. Heijblom, D. Piras, M. Brinkhuis, J. C. G. Van Hespen, F. M. Van Den Engh, M. Van Der Schaaf, J. M. Klaase, T. G. Van Leeuwen, W. Steenbergen, and S. Manohar, "Photoacoustic image patterns of breast carcinoma and comparisons with Magnetic Resonance Imaging and vascular stained histopathology," Sci. Rep. **5**, 1–16 (2015).

223. R. Li, M. N. Slipchenko, P. Wang, and J.-X. Cheng, "Compact high power barium nitrite crystal-based Raman laser at 1197 nm for photoacoustic imaging of fat," J. Biomed. Opt. **18**, 040502 (2013).

224. N. Kuo, H. J. Kang, D. Y. Song, J. U. Kang, and E. M. Boctor, "Real-time photoacoustic imaging of prostate brachytherapy seeds using a clinical ultrasound system," J. Biomed. Opt. **17**, 066005 (2012).

225. M. a. Lediju Bell, N. P. Kuo, D. Y. Song, J. Kang, and E. M. Boctor, "In vivo photoacoustic imaging of prostate brachytherapy seeds," J. Biomed. Opt. **19**, 126011-1–13 (2014).

226. B. L. Bungart, L. Lan, P. Wang, R. Li, M. O. Koch, L. Cheng, T. A. Masterson, M. Dundar, and J.-X. Cheng, "Photoacoustic tomography of intact human prostates and vascular texture analysis identify prostate cancer biopsy targets," Photoacoustics **11**, 46–55 (2018).

227. P. Wang, H.-W. Wang, M. Sturek, and J. Cheng, "Bond-selective Imaging of Deep Tissue Through the Optical Window Between 1600 and 1850 nm," J. Biophotonics **5**, 25–32 (2010).

228. *ANSI Z136.1 - Safe Use of Lasers* (American National Standards Institute, Inc., 2007).

229. R. Fakoor, F. Ladhak, A. Nazi, and M. Huber, "Using deep learning to enhance cancer diagnosis and classification," Proceeding 30th Int. Conf. Mach. Learn. Atlanta, Georg. **28**, (2013).

230. A. Coates, A. Arbor, and A. Y. Ng, "An Analysis of Single-Layer Networks in Unsupervised Feature Learning," Aistats 2011 215–223 (2011).

231. R. Arora, M. O. Koch, J. N. Eble, T. M. Ulbright, L. Li, and L. Cheng, "Heterogeneity of Gleason grade in multifocal adenocarcinoma of the prostate," Cancer **100**, 2362–2366 (2004).

232. C. A. Schneider, W. S. Rasband, and K. W. Eliceiri, "NIH Image to ImageJ : 25 years of image analysis," Nat. Methods **9**, 671–675 (2012).

233. A. Vedaldi and B. Fulkerson, "{VLFeat}: An Open and Portable Library of Computer Vision Algorithms," (2008).

234. O. Ukimura, J. A. Coleman, A. De La Taille, M. Emberton, J. I. Epstein, S. J. Freedland, G. Giannarini, A. S. Kibel, R. Montironi, G. Ploussard, M. J. Roobol, V. Scattoni, and J. S. Jones, "Contemporary role of systematic prostate biopsies: Indications, techniques, and implications for patient care," Eur. Urol. **63**, 214–230 (2013).

235. A. El-Hakim and S. Moussa, "CUA guidelines on prostate biopsy methodology," Can. Urol. Assoc. J. **4**, 89–94 (2010).

236. D. Lieu, "Ultrasound Physics and Instrumentation for Pathologists," Arch. Pathol. Lab. Med. **134**, 1541–1556 (2010).

237. B. Bungart, Y. Cao, T. Yang-Tran, G. Sean, L. Lan, D. R. Roblyer, M. O. Koch, L. Cheng, T. M. Masterson, and J.-X. Cheng, "Cylindrical illumination with angular coupling for whole-prostate photoacoustic tomography," Biomed. Opt. Express **27**, 1405–1419 (2019).

238. A. Taruttis and V. Ntziachristos, "Advances in real-time multispectral optoacoustic imaging and its applications," Nat. Photonics **9**, 219–227 (2015).

239. M. Xu and L. V Wang, "Photoacoustic imaging in biomedicine," Rev. Sci. Instrum. **77**, 41101 (2006).

240. K. S. Valluru, B. K. Chinni, N. A. Rao, S. Bhatt, and V. S. Dogra, "Basics and clinical applications of photoacoustic imaging," Ultrasound Clin. **4**, 403–429 (2009).

241. S. Zackrisson, S. M. W. Y. van de Ven, and S. S. Gambhir, "Light in and sound out: emerging translational strategies for photoacoustic imaging," Cancer Res. **74**, 979–1004 (2015).

242. D. Georgescu, E. Alexandrescu, R. Multescu, and B. Geavlete, "Cystoscopy and urinary bladder anatomy," in *Endoscopic Diagnosis and Treatment in Urinary Bladder Pathology* (Elsevier Inc., 2016), pp. 1–24.

243. A.-A. Yassine, L. Lilge, and V. Betz, "Optimizing interstitial photodynamic therapy with custom cylindrical diffusers," J. Biophotonics **0**, e201800153 (2018).

244. J. C. Mizeret and H. E. van den Bergh, "Cylindrical fiberoptic light diffuser for medical applications," Lasers Surg. Med. **19**, 159–167 (1996).

245. M. Li, B. Lan, W. Liu, J. Xia, and J. Yao, "Internal-illumination photoacoustic computed tomography," J. Biomed. Opt. **23**, 1–4 (2018).

246. T. H. Nguyen, Y. Rhee, J. Ahn, and H. W. Kang, "Circumferential irradiation for interstitial coagulation of urethral stricture," Opt. Express **23**, 20829–20840 (2015).

247. W. H. Nau, R. J. Roselli, and D. F. Milam, "Measurement of thermal effects on the optical properties of prostate tissue at wavelengths of 1,064 and 633 nm," Lasers Surg. Med. **24**, 38–47 (1999).

248. A. E. Worthington, J. Trachtenberg, and M. D. Sherar, "Ultrasound properties of human prostate tissue during heating," Ultrasound Med. Biol. **28**, 1311–1318 (2002).

249. J. R. Cook, R. R. Bouchard, and S. Y. Emelianov, "Tissue-mimicking phantoms for photoacoustic and ultrasonic imaging," Biomed. Opt. Express **2**, 3193–206 (2011).

250. M. Fonseca, B. Zeqiri, P. C. Beard, and B. T. Cox, "Characterisation of a phantom for multiwavelength quantitative photoacoustic imaging," Phys. Med. Biol. **61**, 4950–4973 (2016).

251. D. D. Royston, R. S. Poston, and S. A. Prahl, "Optical properties of scattering and absorbing materials used in the development of optical phantoms at 1064 nm," J. Biomed. Opt. **1**, 110–116 (1996).

252. F. Padera, "Measuring absorptance (k) and refractive index (n) of thin films with the perkinelmer lambda 950/1050 high performance UV-Vis/NIR spectrometers," PerkinElmer, Inc. (2013).

253. N. Sultanova, S. Kasarova, and I. Nikolov, "Dispersion properties of optical polymers," in *Proceedings of the International School and Conference on Photonics* (2009), Vol. 116, pp. 585–587.

254. H. J. van Staveren, C. J. M. Moes, J. van Marie, S. A. Prahl, and M. J. C. van Gemert, "Light scattering in lntralipid-10% in the wavelength range of 400–1100 nm," Appl. Opt. **30**, 4507–4514 (1991).

255. J. Crisp and B. Elliott, *Introduction to Fiber Optics*, 3rd ed. (Elsevier, 2005).

256. E. B. Stechel, K. D. Meeks, W. M. Trott, P. E. Klingsporn, and D. M. Berry, "High-power transmission through step-index multimode fibers," in *Proc. of SPIE* (1990), Vol. 1441, pp. 61–70.

257. M. Ai, W. Shu, T. Salcudean, R. Rohling, P. Abolmaesumi, and S. Tang, "Design of high energy laser pulse delivery in a multimode fiber for photoacoustic tomography," Opt. Express **25**, 17713–17726 (2017).

258. E. B. Stechel, "Laser-induced damage in step-index multimode fibers," in *Proc. of SPIE* (1993), Vol. 1848, pp. 1848–1849.

259. K. Irisawa, T. Hirasawa, K. Hirota, K. Tsujita, and M. Ishihara, "Influence of laser pulse width to the photoacoustic temporal waveform and the image resolution with a solid-state excitation laser," in *Proc. of SPIE, Photons Plus Ultrasound: Imaging and Sensing* (2012), Vol. 8223W, p. 82232W–8223–8.

260. H. Moradi, S. Tang, and S. E. Salcudean, "Towards intra-operative prostate photoacoustic imaging: configuration evaluation and implementation using the da vinci research kit," IEEE Trans. Med. Imaging 1 (2018).

261. P.-T. Dong, H. Mohammad, X. Wang, J. Hui, J. Li, L. Liang, M. N. Seleem, and J.-X. Cheng, "Annihilation of methicillin-resistant staphylococcus aureus via photobleaching of staphyloxanthin," bioRxiv 227603 (2017).

262. S. R. J. Bott, M. P. A. Young, M. J. Kellett, and M. C. Parkinson, "Anterior prostate cancer: is it more difficult to diagnose?," BJU Int. **89**, 886–889 (2002).

263. W. H. Nau, R. J. Roselli, and D. F. Milam, "Measurement of thermal effects on the optical properties of prostate tissue at wavelengths of 1,064 and 633 nm," Lasers Surg. Med. **24**, 38–47 (1999).

264. V. Dogra, B. Chinni, S. Singh, H. Schmitthenner, N. Rao, J. J. Krolewski, and K. L. Nastiuk, "Photoacoustic imaging with an acoustic lens detects prostate cancer cells labeled with PSMA-targeting prostate cancer cells labeled with PSMA-targeting," J. Biomed. Opt. **21**, 066019 (2016).

265. C. Morash, R. Tey, C. Agbassi, L. Klotz, T. McGowan, J. Srigley, and A. Evans, "Active surveillance for the management of localized prostate cancer: Guideline recommendations," Can. Urol. Assoc. J. **9**, 171–178 (2015).

VITA

Brittani Bungart was born and raised in Jefferson City, MO, USA. In 2012, she graduated from the University of Missouri with a Bachelor of Science degree in Biological Engineering with Honors. At the University of Missouri, she worked under the supervision of Dr. James C-M. Lee on the topic of Alzheimer's disease. During this time she co-founded the Mizzou Biomedical Competitive Advancement Team (BioCATs) and was Treasurer of the University of Missouri Chapter of the Institute of Biological Engineering. She was also a McNair Scholar and honored as the Most Outstanding Biological Engineering Senior and the Discovery Inductee for the Mizzou Ring Society. In 2011, Brittani participated in the University of South Carolina's National Institutes of Health Research Experience for Undergraduates in the Department of Biomedical Engineering under the supervision of Dr. Melissa Moss. In 2013, Brittani matriculated into the Medical Scientist Training Program at the Indiana University School of Medicine, where she finished the basic sciences portion of the medical curriculum from 2013 to 2015. From 2015 to 2019, Brittani has pursued her doctoral degree in Biomedical Engineering at Purdue University's Weldon School of Biomedical Engineering under the supervision of Dr. Ji-Xin Cheng and Dr. Young Kim. During this time she has participated in highly interdisciplinary, translational research projects and was awarded a predoctoral fellowship from the Indiana Clinical and Translational Sciences Institute and the Bilsland Dissertation Fellowship. From October 2017 to 2019, Brittani completed research for her dissertation as a visiting scholar at Boston University's Electrical and Computer Engineering Department under the mentorship of Dr. Ji-Xin Cheng. In addition to research, Brittani has served as a counselor at Camp MD/Dr. Camp, an outreach camp for minorities in healthcare, for four years and also co-chaired the programs during her last year. She has also been active in the Combined Degree Student Counsel at Indiana University School of Medicine as the Purdue University Representative and American Physician Scientist Association Representative. She has also participated in the American Physician Scientist Association's Mentorship Program for three years and served as research chair for the Urology Student Interest Group at Indiana University School of Medicine. After completion of her Ph.D., she will return to Indiana University School of Medicine to complete her degree in medicine.

PEER-REVIEWED PUBLICATIONS

1. **Bungart B**, Cao Y, Yang-Tran T, Gorsky S, Lan L, Roblyer D, Koch MO, Cheng L, Masterson T, Cheng JX. Cylindrical Illumination with Angular Coupling for Whole-Prostate Photoacoustic Tomography. Biomed. Op. Express. 2019 Feb 22;10(3):1405-1419.

2. **Bungart BL**, Lan L, Wang P, Li R, Koch MO, Cheng L, Masterson TA, Dundar M, Cheng JX. Photoacoustic Tomography of Intact Human Prostates and Vascular Texture Analysis Identify Prostate Cancer Biopsy Targets. Photoacoustics. 2018 Aug 3;11:46-55.

3. Acuna A, Berman AG, Damen FW, Meyers BA, Adelsperger AR, Bayer KC, Brindise MC, **Bungart B**, Kiel AM, Morrison RA, Muskat JC, Wasilczuk KM, Wen Y, Zhang J, Zito P, Goergen CJ. Computational Fluid Dynamics of Vascular Disease in Animal Models. J. Biomech. Eng. 2018 Aug 1;140(8).

4. Lee HJ, Zhang D, Jiang Y, Wu X, Shih PY, Liao CS, **Bungart B**, Xu XM, Drenan R, Bartlett E, Cheng JX. Label-Free Vibrational Spectroscopic Imaging of Neuronal Membrane Potential. J Phys Chem Lett. 2017 May 4;8(9):1932-1936.

5. Zhu D, **Bungart BL**, Yang X, Zhumadilov Z, Lee JC, Askarova S. Role of Membrane Biophysics in Alzheimer's-related Cell Pathways. Front. Neurosci. 2015 May 27;9:186. Review.

6. **Bungart BL**, Dong L, Sobek D, Sun GY, Yao G, Lee JC. Nanoparticle-emitted Light Attenuates Amyloid-β-induced Superoxide and Inflammation in Astrocytes. Nanomedicine. 2014 Jan;10(1):15-7.

7. Li K, Markosyan RM, Zheng YM, Golfetto O, **Bungart B**, Li M, Ding S, He Y, Liang C, Lee JC, Gratton E, Cohen FS, Liu SL. IFITM Proteins Restrict Viral Membrane Hemifusion. PLoS Pathog. 2013 Jan;9(1):e1003124.